University of Glasgow

Graphene Field Effect Transistor Based Pressure Sensors for Tactile Sensing Applications

Nivasan Yogeswaran

A thesis submitted in fulfilment for the degree of

Doctor of Philosophy

Electronics and Nanoscale Engineering Research Division
School of Engineering

University of Glasgow

January 2019

Abstract

The development of electronic skin emulating human skin's functionality is a growing area of interest due to its prospect in autonomous and interactive robots, prosthesis and wearable health monitoring devices. In an effort to mimic human skin a number of sensors for the detection of various stimuli have been developed including pressure, strain and thermal sensors. Amongst them, a significant effort has been focused on the development of novel pressure sensors due to their potential in the aforementioned applications. A number of strategies have been adopted for the development of pressure sensors and in particular, there has been a growing interest in the development of field effect transistor (FET) based pressure sensors. This is due to the capability to develop large area high spatial resolution active matrix pressure sensor array. In recent times, there has been a growing demand for the development of flexible pressure sensors due to emerging applications such as smart prosthesis, interactive robots, and wearable electronics. The use of conventional material like Si for flexible electronic applications are limited owing to their rigid and brittle nature. This has led to the investigation of various novel materials like organic semiconductors, carbon nanotube, inorganic semiconductor nanowires, and graphene. Amongst them, graphene is an attractive choice owing to its intrinsic material properties such as its electronic and mechanical properties. Further, the complementary metal oxide semiconductor (CMOS) compatibility and ability to grow high-quality graphene over a large area, and its low optical absorption are some of the other attractive features for the development of large area transparent electronic applications. The high mobility of graphene would enable the development of low voltage devices attractive for flexible electronics applications. This thesis presents work on the development of graphene field effect transistor (GFET) based pressure sensors for tactile sensing applications.

The developed sensor comprises of two main components: a top-gate GFET and a piezoelectric transducer layer. A commercially available chemical vapour deposition grown monolayer graphene on Cu foil (from Graphenea) was used as the channel material of the transistor. A high-κ Al_2O_3 deposited by atomic layer deposition technique was employed as the top-gate dielectric. In particular, care was taken to ensure a low temperature CMOS compatible process was adopted for the development of GFET. This ensured that the developed fabrication process could be transferred directly for the development of flexible devices. The development of the transfer process, the impact of different polymers (used as supporting layer during the transfer

process) on graphene and the optimisation of dielectric deposition process are discussed in the thesis.

The piezoelectric transducer layer is another vital component of the developed pressure sensor. In this respect, two piezoelectric materials, lead zirconate titanate (PZT) and aluminium nitride (AlN), have been investigated as the transducer layer. The pressure sensors were characterised with the piezoelectric transducer layer in an extended-gate configuration with GFET. PZT based pressure sensors exhibited a pressure sensitivity of 4.55×10^{-3} kPa^{-1} for a pressure range between 0 - 94.18 kPa. Though PZT is a better piezoelectric material than AlN, CMOS process incompatibility, non-biocompatibility and high processing temperature often associated with PZT limit its use in the development of flexible electronics especially for wearable applications. Therefore, AlN deposited by low temperature radio frequency magnetron sputtering has been explored as an alternate piezoelectric transducer layer for pressure sensing applications. The use of AlN also evades the need for the high voltage poling process often employed to enhance the piezoelectric property of the material. The AlN deposited via an optimised RF sputtering process reported in the thesis resulted in film with a piezoelectric constant of 5.9 pC/N. Similar to PZT , AlN was also characterised in an extended gate configuration and exhibited a sensitivity of 7.18×10^{-3} kPa^{-1} for a pressure range of 0-9.74 kPa.

In an attempt to improve the spatial sensor resolution of sensor and to improve the signal to noise ratio a piezoelectric layer integrated within the top gate dielectric stack was investigated. In this regard,a flexible GFET with a piezoelectric layer integrated with the top-gate dielectric film was developed. The top gate dielectric stack comprise a 15 nm Al_2O_3(deposited by ALD)/ 90 nm AlN (deposited by RF sputtering). The developed device exhibited typical GFET electrical characteristics. The electron and hole mobility of the developed devices were 1612 $cm^2/V.s$ and 1568 $cm^2/V.s$ respectively. In addition, the device also displayed a stable electrical response under mechanical bending condition, thereby demonstrating its potential in the development of flexible electronics.

Acknowledgements

First and foremost, I am extremely thankful to my supervisor Prof. Ravinder Dahiya for giving me the opportunity to work in this exciting field and for his guidance and motivation and the freedom he provided me to pursue my research. I would also like to thank my co-supervisor Dr. Leandro Lorenzelli for his guidance and support during my stay at Fondazione Bruno Kessler (FBK), Italy and for all the hiking trips. I would also like to thank my other co-supervisor Dr.Vincenzo Vinciguerra, for his technical guidance and support especially during my secondment at STMicroelectronics. I would also like to thank him for his amazing Italian treats he offered us during my secondment.

Special thanks to Shoubhik and Wenting for amazing memories, dinners, parties, and trips. Thanks for the boundless support you have provided me throughout my Ph.D. Shoubhiks one-liners and Wenting's laugh will be missed. I would also like to express my sincere thanks to Dr.Dhayalan (Dhaya Anna), Willam (Boss), Dr.Libu (Libu Cheta) for their unwavering support, motivations and the knowledge you have passed me. Special thanks to Libu Cheta and Dhaya Anna for awesome Thosai and Indian foods. I would also like to thank Tasos (T.V), Fengyuan and Habib for their support during the course of my Ph.D. Thanks to my friends Dr. Sajina and Dr. Saleem for making me feel home and for the support and advise you guys provided me during my stay in Italy.

I am also extremely grateful to the staffs of JWNC and FBK without whose support none of the work presented in this thesis would have been possible. I would like to say my special thanks to Stefano, Flavio, Severino, Paolo, Helen, David, Lesley, Thomas, Colin, Susan, Dougie, Dr. Stephen Thoms for their support.

I am also thankful to European Commision in the framework of FP7 Project CONTEST and School of Engineering for the financial support.

Thanks to my friends Pradeep, Bhavana, Pavi for all the banters and dinner.

I am also particularly grateful for my aunt (Sutharsana) and uncle (Mugunthan) and my cousins for the support they have provided me during my stay in UK and making me feel home. Thanks for everything.

Finally and most importantly, I am thankful to my wonderful Family. None of what I have achieved in life would have been possible without their support. I would like to thank my Mom and Dad for the love and support I have had received since the day I was born. I am extremely lucky to have my two wonderful sisters who always cheer me up and kept me in check with their call. Thanks for everything you have done to me.

List of Publications

Journal Articles

1. F. Liu, W.T. Navaraj, **N. Yogeswaran**, D. Gregory, R. Dahiya "Van der Waals contact engineering of graphene field-effect transistors for large-area flexible electronics," *ACS Nano*, vol. 13, no. 3, p.13, 2019.

2. L. Manjakkal, W. Dang, **N. Yogeswaran**, R. Dahiya "Textile Based Potentiometric Electrochemical pH Sensor for Wearable, " *Biosensors*, vol.9(1), no.14, 2019.

3. **N. Yogeswaran**, W.T. Navaraj, S. Gupta, F. Liu, V. Vinciguerra, L. Lorenzelli and R. Dahiya "Piezoelectric Graphene Field Effect Transistor for Tactile Sensing" *Applied Physics Letter*, 13, 014102, 2018.

4. **N. Yogeswaran**, W. Dang, W. T. Navaraj, D. Shakthivel, S. Khan, E. O. Polat, et al., "New materials and advances in making electronic skin for interactive robots," *Advanced Robotics*, vol. 29, p.1359-1373, 2015.

5. S. Khan, **N. Yogeswaran**, W. T. Navaraj, L. Lorenzelli, and R. Dahiya, "Flexible FETs using ultrathin Si microwires embedded in solution processed dielectric and metal layers," *Journal of Micromechanics and Microengineering*, vol. 25, p. 125019, 2015.

Journal Article under preparation

1. **N. Yogeswaran**, S. Gupta, R. Dahiya "Flexible Piezoelectric Graphene Field Effect Transistor Pressure Sensor for Tactile Sensing Applications".

2. S. Gupta, **N. Yogeswaran**, F. Giacomozzi, L. Lorenzelli, R. Dahiya "Touch Sensor based on Flexible AlN Piezocapacitor Coupled with MOSFET" *IEEE sensor Journal- Submitted.*

3. R. Dahiya, **N. Yogeswaran**, F. Liu, L. Manjakkal, H. Jorntell, "Large Area eSkin: The Challenges Beyond Sensor Designs," -*Submitted* .

Conference Proceedings

1. **N. Yogeswaran**, S. Gupta, R. Dahiya, "Low Voltage Graphene FET Based Pressure Sensor," *IEEE Sensors*, New Delhi, p. 1-4, 2018.

2. S. Gupta, **N. Yogeswaran**, F. Giacomozzi, L. Lorenzelli, R. Dahiya, "Flexible AlN Coupled MOSFET for Touch Sensing," *IEEE Sensors*, New Delhi, p. 1-4, 2018.

3. F. Liu,**N. Yogeswaran**, C. G. Nunez, D. Gregory and R. Dahiya "Graphene-ZnO NWs hybrid film for large-area UV photodetector, " *IEEE Sensors*, New Delhi, p. 1-4, 2018.

4. **N. Yogeswaran**, D. Shakthivel, L. Lorenzelli, V. Vinciguerra and R. Dahiya "Graphene Au Nanoparticle Hybrid Near-Infrared Photodetector," *IEEE Sensors*, Glasgow, p. 1-3, 2017.

5. F. Liu, W. Taube, **N. Yogeswaran**, D. Gregory, and R. Dahiya, "Transforming the Short-Term Sensing Stimuli to Long-Term E-Skin Memory," *IEEE Sensors*, Glasgow, p. 1-3, 2017.

6. D. Shakthivel, **N. Yogeswaran**, and R. Dahiya, "Towards Graphene Based Flexible Force Sensor, " *IEEE Sensors*, Glasgow, p. 1-3, 2017.

7. **N. Yogeswaran**, Z. Tang, V. Vinciguerra and R. Dahiya "Bending Effects in a Flexible Dual Gated Graphene FET: a Verilog-A Model Implementation," *European Conference on Circuit Theory and Design (ECCTD)*, Catania, p. 1-4, 2017.

8. W. T. Navaraj, **N. Yogeswaran**, V. Vinciguerra and R. Dahiya "Simulation Study of Junctionless Silicon Nanomembrane FETs for High performance Printable Electronics," *European Conference on Circuit Theory and Design (ECCTD)*, Catania, p. 1-4, 2017

9. **N. Yogeswaran**, S. Tinku, S. Khan, L. Lorenzelli, V. Vinciguerra and R. Dahiya, "Stretchable resistive pressure sensor based on CNT-PDMS nanocomposites," *11th Conference on Ph.D. Research in Microelectronics and Electronics (PRIME)*, Glasgow, p. 326-329, 2015.

10. S. Khan, **N. Yogeswaran**, L. Lorenzelli, and R. Dahiya, "Si Microwires Based FETs on Flexible Substrates," *11th Conference on Ph.D. Research in Microelectronics and Electronics (PRIME)*, Glasgow, p. 326-329, 2015.

11. **N. Yogeswaran**, S. Khan, W. Dang, E. O. Polat, L. Lorenzelli, et al., "Tuning electrical conductivity of CNT-PDMS nanocomposites for flexible electronic applications," *15th International Conference on Nanotechnology (IEEE-NANO)*, Rome, p. 1441-1444, 2015.

Contents

List of Figures

List of Tables

Glossary of Abbreviations

ALD	atomic layer deposition
AFM	atomic force microscope
CAB	cellulose acetate butyrate
CMOS	complementary metal-oxide semiconductor
CNP	charge neutrality point
CNT	carbon nanotube
CVD	chemical vapour deposition
DTM	diffusive transport model
DTG	dry transfer of graphene
EDX	energy dispersive X-ray spectroscopy
EG	epitaxial growth of graphene
E-skin	electronic skin
FET	field effect transistor
GFET	graphene field effect transistor
HMDS	hexamethyldisilazane
PZT	lead zirconate titanate
LDL	lower detection limit
LPE	liquid phase exfoliation
MIM	metal-insulator-metal
MIS	metal-insulator-semiconductor
MLG	mono layer graphene
MOSFET	metal-oxide-semiconductor field effect transistor
NWFET	nanowire field effect transistor
OFET	organic field effect transistor
PAT	polymer assisted transfer
PC	poly(bisphenol A carbonate)
PDMS	polydimethylsiloxane
PEN	polyethylene napthalate
PET	polyethylene terephthalate
PI	polyimide
PMMA	poly(methyl methacrylate)
PSR	pressure sensitive rubber
PTM	peak transconductance method

PVC	polyvinyl chloride
RF	radio frequency
RIE	reactive ion etching
SEM	scanning electron microscope
SiNR	silicon nanoribbon
TFT	thin film transistor
TMA	trimethylaluminium
XRD	x-ray diffraction
C_{bg}	back gate oxide capacitance
C_{ox}	top gate oxide capacitance
R_c	contact resistance
$R_{channel}$	channel resistance
R_{total}	total device resistance
μ	mobility
V_{bg}	back-gate voltage
V_{Dirac}	Dirac voltage
V_{tg}	top gate voltage
$V_{tg,Driac}$	top gate Dirac point voltage

Chapter 1

Introduction

Flexible electronics are expected to be next big evolution of electronics industry. This has been primarly driven by its potential applications in various sectors such as consumer electronics, health care monitoring, computing platforms, energy storage and generation etc [1]. The development of flexible electronics requires new approaches to be adopted in terms of material, design and fabrication technologies. The traditional materials employed in the development of conventional electronics are limited by their rigid and brittle nature. This has lead to the investigation of novel materials and smart structural engineering approaches for the development of flexible and strecthable electronics [2]. In its infancy stage, organic semiconductors were the natural choice for the development of flexible electronics due to their inherent flexible nature and low processing cost and compatibility with existing printing techniques. However, the low carrier mobility of organic semiconductors ($\mu \approx 0.5 - 5cm^2/V.s$) [3] have limited their use in high performance applications [2, 4, 5]. This led to the exploration of new novel materials such as inorganic nanowires and nanomembrane [6–9], carbon nanotube (CNT) and graphene for the development of flexible electronics. Amongst them, carbon nanomaterials like CNT and graphene are attractive candidates for the development of flexible electronics due to their fascinating electrical properties [10]. Besides their electrial properties, these materials also demonstrate excellent mechanical and optical properties which are attractive for the development of flexible electronics [11, 12]. However, the use of CNT is limited by the lack of control over its chirality and the challenges associated with the formation of a film with a dense network of CNTs required for device development. In this regard, graphene is a more promising material for large area electronics applications. Further, the demonstration of large scale growth of graphene compatible with roll-to-roll production and printing demonstrates its feasibility for mass industrial production for the development of flexible electronics [13–15].

Electronic skin (e-skin) is one of the rapidly progressing applications of flexible electronics with the advent of humanoids, smart prostheses and wearable electronics. Human skin is the largest and most important sense organ of our body. The sense of touch provides us with vital information of our environment which cannot be decoded

from audio or visual cues. Some of the information gathered from tactile feedback includes surface texture, change in temperature and magnitude of applied pressure etc. The human skin consits of distinct sensory receptors for different stimuli such as mechanoreceptors (for presure and vibration), thermoreceptors (for temperature) and nocioceptors (for pain) [16]. The development of e-skin, mimicking the human skin would have a profound impact on the aforementioned applications. For instance, robots have advanced from mere industrial tools used in human restricted environments towards autonomous humanoids and social robots where they are expected to be involved in human interactions. Therefore, the development of robots/ artificial intelligent systems equipped with e-skin would enable the development of truly smart autonomous systems which could adapt to various environments and enable safe human-machine interaction [17]. Smart-prosthesis is another emerging field where e-skin would have a huge impact. In fact prosthesis with tactile feedback are one of the two preferred features by amputees [18]. The integration of e-skin with prosthesis would provide several benefits to amputees including: enabling amputees to overcome phantom limb pain; providing a sense ownership over the prosthesis as it would become part of the body; reducing the cognitive strain often associated with audio and visual feedbacks [18, 19].

The primary functionality of human skin is the sense of touch detected by the mechanoreceptors. There are four types of mechanoreceptors for measuring force applied for different time durations. The slow-adapting receptors (SA-I and SA-II) respond to static pressure and are responsible for surface texture and pattern discrimination and deformation of skin. The fast adapting receptors (FA-I and FA-II) enable the detection of dynamic forces applied at both low (5-50 Hz) and high frequencies (400 Hz). These are critical for object manipulation and grip control [16, 19]. The type and distribution of these receptors varies within the skin. For instance, finger tips consist of about 241 units/cm^2 while the palm region consists of 58 units/cm^2 [20]. In an attempt to mimic the human skin's mechanoreceptors a number of transduction mechanisms and device architectures have been explored. Among different architectures, field effect transistors (FET) based pressure sensors are an attractive choice. Adaptation of FET based pressure sensor would enable the development of high sensitivity and high spatial resolution sensors for active matrix thereby minimising the cross talks often observed in passive matrix. Therefore, considering the above mentioned factors, FET based pressure sensors are an ideal choice for mimicking the human skin. In addition, FET would also allow facile integration with circuitry. Despite, significant progress in the development of pressure sensors, a number of the bottlenecks still remains to be addressed for the realisation of large area e-skin for robotics and prosthesis applications. These includes low-operation voltage, mechanical flexibility and high sensitivity that could match the human skin's performance, robustness, low cost fabrication processes and process compatibility with the existing fabrication techniques. In this regard, the the major objective of this thesis

is the development of graphene FET (GFET) based pressure sensors for tactile sensing application.

1.1 Objective and Outcome of the Thesis

The objective of the thesis is to develop a pressure sensor for e-skin applications. In this regard, a GFET based pressure sensor has been developed to explore the best of both worlds (graphene and FET). The body of work presented in this thesis provides a new approach for the development of GFET based pressure sensors for tactile sensing applications. Graphene was chosen as the channel material for the device development owing to its fascinating intrinsic material properties such as its mechanical and electrical properties which are ideal for the development of flexible electronics.

The aims of the thesis are as follows:

- Development of a low temperature CMOS compatible process for the development of GFET. This entails the transfer printing process of graphene and process development for a low residue photolithography process on graphene for electrode deposition and graphene patterning.

- Investigation of different piezoelectric transducer material for pressure sensing applications. In this regard two materials, PZT and AlN has been investigated as a transducer layer for the pressure sensor. Process development and optimisation of the piezoelectric AlN as the transducer layer for the development of GFET based pressure sensor was studied. The deposition of AlN was carried out using a low temperature radio frequency (RF) magnetron sputtering process, thereby ensuring a complete a CMOS compatible fabrication process for development of flexible pressure sensors.

- Demonstration of a GFET based pressure sensor that operates at a remarkably low voltage (100 mV). The operation of the sensor was based on the piezopotenial modulation for drain current.

- Demonstration of flexible GFET comprising of top gate dielectric stack of ALD Al_2O_3 / piezoelectric AlN. This will be explored for the flexible pressure sensing applications

1.2 Structure of Thesis

The organisation and content of the thesis are as follows:

Chapter 2 presents the state of the art on the development of physical sensors. It covers various transduction mechanisms and strategies adopted to develop flexible physical sensors. In particular, approaches used for the development of FET based

pressure sensors are also discussed in detail towards the end of the chapter. In addition, it also provides an introduction to graphene,its electrical properties and key parameters associated with GFET are discussed. In addition, an overview of major graphene synthesis methods are discussed.

Chapter 3 describes the fabrication and characterisation techniques adopted for the development of the graphene pressure sensor reported in this thesis. The fabrication section discusses the optimised recipe adopted for the device development while the characterisation techniques cover various material and electrical characterisation techniques employed for the device characterisation.

Chapter 4 provides an in-depth study on the impact of the polymers used during the transfer process on graphene. Three polymers were investigated for the transfer of graphene, their impact on the transferred graphene samples were evaluated using AFM, Raman spectroscopy and electrical characterisation.

Chapter 5 details the optimisation and characterisation of ALD Al_2O_3 used as a top-gate dielectric material. The chapter also presents the process optimisation for the development of highly c-axis oriented AlN film as a transducer layer for the pressure sensing application.

Chapter 6 describes the fabrication and characterisation of top-gate GFETs. The GFET was developed using a low temperature CMOS compatible process thereby allowing the direct adoption of the process for the development of the flexible devices. The chapter begins with the fabrication and characterisation of back-gate GFET. Following which a top-gate GFET is realised. The electrical characterisation of the top gate GFET is presented.

Chapter 7 presents the development of graphene field effect transistor based pressure sensor for tactile sensing applications. Two piezoelectric materials (PZT and AlN) in an extended gate configuration have been investigated for pressure sensing applications. The sensor performance for different piezoelectric materials is discussed. Finally, a flexible GFET comprising of AlN integrated within the top-gate dielectric stack is presented.Notably, the device was fabricated by adopting a low temperature CMOS compatible process. The developed device would be explored for pressure sensing applications.

Chapter 8 summaries the key outcome of the research work and provides suggestions for future works.

Chapter 2

State of the Art: Pressure Sensors and Materials for E-skin Applications

2.1 Introduction

Skin, the largest organ of the human body, plays a vital role in the way in which the humans perceive and interact with the environment. It provides crucial information to distinguish between different stimuli such as temperature, pain, mechanical force etc. In addition, human skin is also capable of efficiently differentiating mechanical stimuli caused by interaction with different surface textures and magnitude of forces and frequencies of force. In this regard, emulating human skin's sensory ability via electronics has recently become an area of growing interest, owing to its broad applications in the field of the prosthesis, robotics, health-care monitoring device, human-machine interaction devices etc [21–24]. Especially, in application with regard to prosthesis and robotics, integrating the sense of touch could have a profound impact, enabling a more facile and natural interaction [18], while easing the cognitive requirements where the operation relies solely on the visual or auditory informations for the operation [25].

The human sense of touch can be classified into two categories based on the origin of the sensory input as: (1) cutaneous; (2) kinesthetics. Cutaneous sense refers to sensory input originating from the receptors embedded within the skin and the associated somatosensory system, therefore it is responsible for information gathered on interaction with the object. Kinesthetics sense arises from the input from the receptors available at tendons, joints and muscles, therefore can provide information on static and dynamic positions of the body. The tactile perceptions of humans rely on cutaneous sense to detect a mechanical stimuli, temperature and pain etc [26, 27]. The tactile sensing is referred to as the detection and quantification of a given property of a contact area and pre-processing of the signal before the signal is sent to a higher level for final data interpretation, resulting in reduction of data processing capability requirement

[27]. In the context of robotic tactile sensing, the aforementioned sensory input can be classified into intrinsic and extrinsic sensing. Intrinsic sensors refers to tactile sensors embedded within the structure to detect parameters such as magnitude of force, while the extrinsic sensors refers to sensors placed closer to the contact surface/interface and used for the determination of tactile data at a localised point [16]. Though human sense of touch has been well documented, the ability to mimic the human tactile sensing characteristics still remains a major challenge, due to its distributed nature, high sensitivity, and fast response. Besides, the tactile sensing ability of human skin, e-skin should also be stretchable/conformable similar to human skin, differentiate between different mechanical stimuli, and exhibit the ability to detect two stimuli such as temperature and humidity simultaneously [28–30]. In addition, the development of self-healing sensors [31], self-powered sensors [22] [32, 33] and chemical sensors for health-care monitoring have also been explored in the development of electronic skin.

In the pursuit of development of e-skin, various novel materials and device architecture are being explored to attain the required criteria. Amongst various material, graphene has become an attractive choice owing to fascinating intrinsic properties, and development of large scale synthesis techniques. Further, the development of graphene FET based physical sensors would enable the realisation of large area active matrix tactile sensors. This chapter will provide an overview of various strategies and techniques that have been adopted in the development of pressure sensors for e-skin applications. In addition, graphene's properties relevant to FET applications and widely used synthesis methods are discussed.

2.2 Prerequisites of Pressure Sensor

In addition to flexibility and robustness, pressure sensors developed for e-skin and other applications are required to meet certain prerequisites to satisfy the end applications. These parameters include pressure range, sensitivity, linearity, lower detection limit (LDL), response time and operation voltage.

A high sensitivity over a large dynamic pressure range is an appealing feature for pressure sensors. For applications related to e-skin, the low (<10 kPa) and medium pressure (10-100 kPa) regime are an area of interest, as they represent the pressure range associated with gentle touch and object manipulations [34]. Figure 2.1 shows the pressure range and the potential applications for a given pressure regime. The low pressure range can be further classified into subcategories to define their potential uses beyond e-skin for robotics and prosthesis: ultra low pressure regime (< 1Pa), subtle-pressure (1 Pa- 1 kPa), low pressure (1-10 kPa) [35]. The ultra low pressure range described are often observed in audio/ sound-generated pressure [36] could find application in development of microphones and other sound generated pressure sensitive devices [36]. The development of sensors in the subtle pressure range could have an impact in biomedical devices to monitor vital health signs such as breathing rates [37].

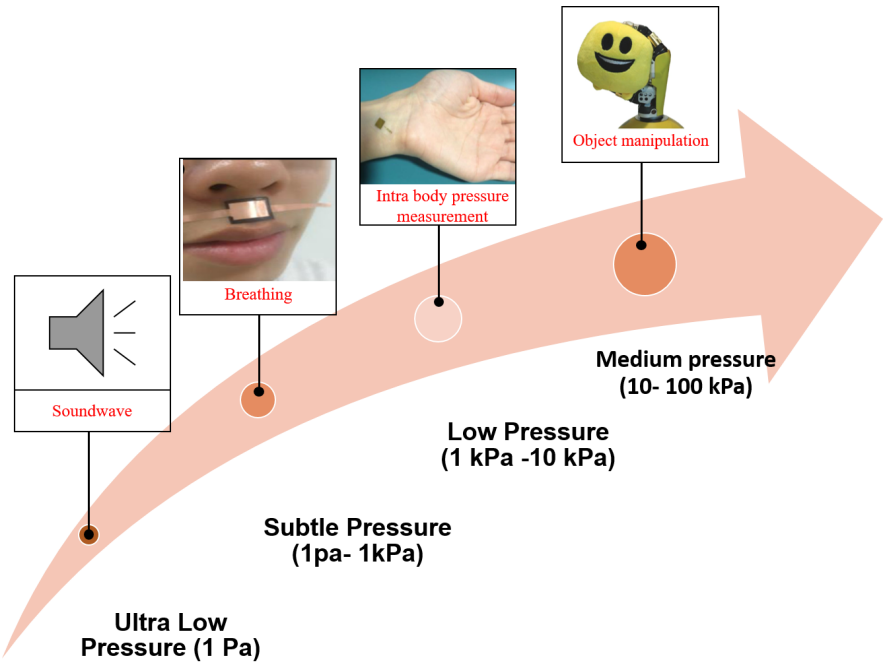

Figure 2.1: Classification of pressure regime and its corresponding applications [37] [38] [22].Reprinted (adapted) with permission from [37]. Copyright © 2018 American Chemical Society.

.

In addition, development of pressure sensors would lead to ultra-sensitive e-skin, which surpasses the human sensitive regime. Low pressure range represents the range of pressure we often encounter on a daily basis, such as gentle touch, intra body pressure etc., therefore this has become an area of growing interest for development of sensors for wearable health-monitoring devices [38, 39]. As mentioned above, the pressure regime associated with object manipulation often falls under the medium pressure regime category. Besides, this development of sensors in this pressure regime would enable healthcare monitoring devices for pulse monitoring, biomechanics application associated with gait monitoring for early detection of Parkinson's disease [37] [39].

Sensitivity (S=$\Delta Y/\Delta P$) is another important parameter of the pressure sensor. It is defined as the change in the output signal (ΔY) of the sensor with respect to the corresponding change in the pressure (ΔP). In addition to high sensitivity, linearity of the sensitivity over a wide range of pressure is another preferred feature in a sensor. Linearity can be described as the range over which a linear relationship is observed between the sensitivity of the sensor and the applied pressure. LDL of the sensor refers to its lowest possible limit of pressure detection by the sensors. Especially, with regard to e-skin, the two other most important parameters are operation voltage and response time. In order to truly mimic the human skin requires a large number of sensors arranged in a distributed manner similar to human skin. Such distributed nature of a large number of sensors would result in a power hungry system, thereby limiting its use in a wearable and portable system. Therefore the development of sensors with

low operation voltage have become an area of growing interest. Further, applications related to grasp and slip detection require sensors with low response time. Response time of the sensor is defined as the time interval between the between stimuli event and stable output of sensor.

2.3 Transduction Mechanisms

The operation of physical sensors developed for e-skin application relies on the effective conversion of mechanical stimuli into an electrical signal. Three most widely adopted transduction mechanisms for the detection of mechanical stimuli such as pressure, strain, shear and torsion for e-skin applications are resistive, capacitance and piezoelectric. Besides aforementioned techniques,other transduction mechanism such as optics, ultrasonic and triboelectric have also been adopted for pressure sensing applications. Figure 2.2 depicts a schematic illustration of the 3 major transduction mechanisms widely adopted in e-skin applications.

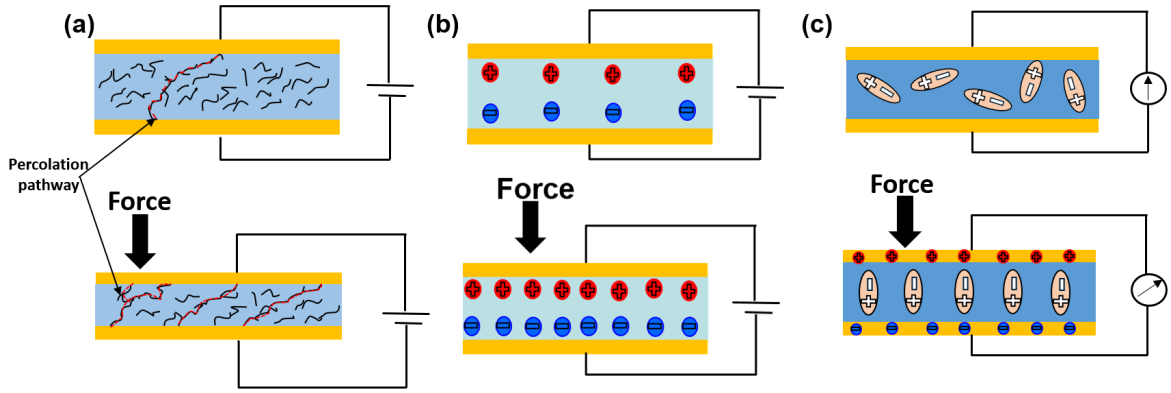

Figure 2.2: Schematic illustrating 3 major transduction mechanisms widely used in physical sensors for e-skin applications(a)Piezoresistive (b)Capacitive (c)Piezoelectric.

2.3.1 Piezoresistive

Piezoresistive sensors' transduction mechanisms rely on change in the sensor resistance on application of mechanical stimuli. These sensors are have been investigated, owing to simpler device architecture and easy to readout mechanisms. In addition, piezoresistive sensors also exhibit high sensitivity over large pressure and flexion and enable a high pixel density [23]. Two widely-adopted techniques for the development of piezoresitive based pressure sensors are (a) change in the contact resistance of two conductive layer [23] [40, 41]; (b) use of the intrisic piezoresistive propterty of the material [42, 43].;

The change in the contact resistance between two conductors on application of force is related by $R_C = F^{1/2}$, [44] therefore the sensors exhibit a high sensitivity over large range of pressure. Gong et al demonstrated a piezoresistive sensor comprising of gold nanowire impregnated tissue paper on intergidated electrodes with a high sensitivity(S= 1.14 kPa^{-1}) over a wide pressure range (13 Pa - 50 kPa) [41]. Sun et al demostrated

a transparent co-planar gate GFET based active matrix pressure sensor [45]. The sensor comprises top layer with square graphene pattern, while the bottom layer comprises the interdigitated graphene on backplane of GFET. The application of force causes a contact between the top and bottom layer reducing the source to drain resistance of the GFET and increasing its transconductance. The sensor exhibited high sensitivity (0.12 kPa^{-1}) over 2500 pressure release cycles, demonstrating its promise in the development of flexible pressure sensors.

Another popular approach in the development of flexible piezoresistive pressure sensor is the use of nanocomposite as the active area of the sensor. The popularity of the nanocomposite arises due to its low cost and simple fabrication process. It is critical to ensure the uniform dispersion of the nanofillers within the elastomer to minimise the hysteresis behaviour often observed in peizoresistive sensors. Various conductive nanofillers such as carbon black [46], graphene [47, 48], CNTs [49] and metallic nanoparticles [50] incorporated with elastomer have been investigated for physical sensors. The resistance change of nanocomposite arises due to change in the percolation pathway or change in the tunnelling resistance between the filler on application of mechanical stimuli [46] [51].

2.3.2 Capacitive

Capacitive sensors are widely used in a parallel plate configuration where the device capacitance, C, is defined as :$C = \epsilon_o \epsilon_r A/d$, where ϵ_o is the free space permittivity, ϵ_r is the relative permittivity, A is the area of the capacitor and d is the dielectric thickness. Among the above-mentioned parameters change in dielectric thickness or area of the capacitor on an applied pressure or strain is widely used parameters to correlate the change in capacitance with the applied mechanical stimuli. Capacitor based pressure sensors are an attractive choice owing to their simple device structure, high sensitivity, low power consumption and ability to measure a static force. However, capacitive sensors are often affected by cross talks and low signal to noise ratio on scaling down, limiting their applications [52]. Elastomers are popular choice as a dielectric for capacitive sensors. However, elastomer dielectric are affected by significant visco-elastic creep, causing a hysteresis behaviour [53] [54]. Mannsfeld et al reported the use of microstructured polymeric dielectric to improve the viscoelastic creep, where the microstructures provide voids for elastic deformation on application of force [34]. This technique was further extended towards the development of the pressure sensitive FET-based sensors, where microstructured PDMS was used as a gate dielectric of the FET. The application of force results in the change in gate capacitance, thereby resulting in the change in the drain current of the organic FET (OFET) [21]. Besides parallel plate capacitors, co-planar capacitors have also been explored for tactile sensing applications, where the change in the volumetric density of voids on application of force resulted in the change in the dielectric constant of dielectric, leading to observed pressure sensitivity [22].

2.3.3 Piezoelectricity

Piezoelectricity refers to the ability of certain materials to generate charge or voltage on application of a mechanical stress. These materials can also generate force on application of a voltage. A simple piezoelectric sensor resembles a capacitive structure where the dielectric is piezoelectric material. The application of pressure or mechanical stimuli causes the polarisation of material, resulting in the generation of opposite charges at both ends of the electrode, resulting in the voltage generation. The piezoelectric constant of material (d_{33}) is defined as the ability of material to convert the applied force (in the same direction as in which voltage would appear) into charge. Piezoelectric transducers are a popular choice for tactile sensing applications requiring high sensitive, fast and dynamic response, such as slip detection. Unlike capacitive sensors, piezoelectric sensors are not suitable for static pressure measurement, as the generated voltage is an impulsive and occurs only on application and release of force. Recently, Chen et al demonstrated piezoelectric induced $PbTiO_3$ nanowire-graphene based heterostructure for both static and dynamic sensing [55]. The static sensing of the pressure sensors arises from the polarisation charge in $PbTiO_3$ nanowire, which results in an increase of scattering points within the graphene, affecting its conductivity thereby leading to the observed static pressure measurements.

Some of the widely used piezoelectric materials as a transducer layer are PZT [38] [56], zinc oxide [57], polyvinylidene difluoride (PVDF) and its co-polymers [58–60] etc. Inorganic materials like PZT exhibit high piezoelectric coefficient, however they are brittle in nature and their potential is limited in flexible electronics. Recent progress has seen the use of smart engineering to incorporate, inorganic piezoelectric material for flexible cutaneous pressure monitoring applications. Rogers and coworkers demonstrated the use of ultra thin PZT capacitive structure in an extended gate configuration with silicon nanomembrane based MOSFET (all mounted onto Ecoflex) for pressure sensing applications [38]. In the context of developing flexible piezoelectric based pressure sensors, polymer piezoelectric material like PVDF and its copolymers are an attractive choice [59, 61]. Piezoelectric materials have also been explored in the development of self-powered devices where the generated piezopotential is utilised in the device operation [57] [62, 63].

In addition to the three major transduction mechanisms described above, there are several more techniques adopted for pressure sensing applications. These include optical sensors, triboelctric sensors etc. The operation of the optical sensors relies on the measurement of the change in the intensity of the light on application of the force. The optical pressure sensors comprise light source, wave-guide, detector and sensing area. The application of pressure or force in the sensing area causes a change in the intensity of light whose intensity is monitored via detector, thus forming the basis of optical transduction mechanisms [64]. Triboelectric based pressure sensor is another transduction mechanisms which have been explored for tactile sensing application. The transduction mechanisms of sensor rely on the triboelectric effect,

where a contact electrification results in potential generation [65]. Similar to the piezopotential behaviour, triboelectric sensors could pave the way to a new generation of self-powered pressure sensors.

2.4 Striving Towards the Human Skin's Mechanical Property

2.4.1 Geometrical Engineering

Human skin remains the epitome of tactile sensory platforms, comprising a range of sensors distributed across the body. The sensors within the skin can be classified into three major categories: Thermoreceptors for innocuous temperature, nocioceptors for the pain sensation and while the mechanical stimuli are detected by various mechanoreceptors depending on type of force (static or dynamic) and its frequency enabling the humans to differentiate between different mechanical stimuli [16]. Besides its excellent sensing ability, human skin also exhibits some distinguishable features such as mechanical compliance enabling it to stretch and flex and also self-heal on the occurrence of damage. Taking inspiration from the human skin, various strategies have been adopted to incorporate the features in e-skin. The initial works on the development of tactile sensors for touch screen application and prosthesis hands relied on the use of rigid material. In early 1990s, researcher began exploring the use of the organic semiconductors for the development of flexible electronics, where the organic semiconductor based devices showed a similar electrical performance to that of inorganic devices. This presented a major breakthrough in the development of flexible electronics. Since then, a significant progress has been made, where performance of e-skin has surpassed human skin. This section will provide an overview of different techniques adopted to develop flexible or stretchable sensors.

In pursuit of development of e-skin that can match or surpass the human skin's mechanical compliance, various strategies have been adopted. This primarily involves the use of novel materials which are intrinsically flexible/ stretchable or the use of smart structural engineering enabling the use of conventional material for the development of flexible and stretchable devices. Traditionally, Si has been the natural choice for the development of electronics, however its rigid and brittle nature has limited its use in the development of flexible and stretchable electronics. Nonetheless, Si remains an attractive choice owing to its high performance and mature processing technology. Considering this, thin Si have been explored in the development of flexible electronics [66] [67]. Though development of flexible electronics is a major step in e-skin, in order to truly mimic the human skin requires conformable attachment to uneven surfaces, thin Si are not ideal for such applications. Rogers and co-worker have investigateed various strategies to incorporate inorganic material for the development of the stretchable electronics. One strategy is buckling where inorganic structures like

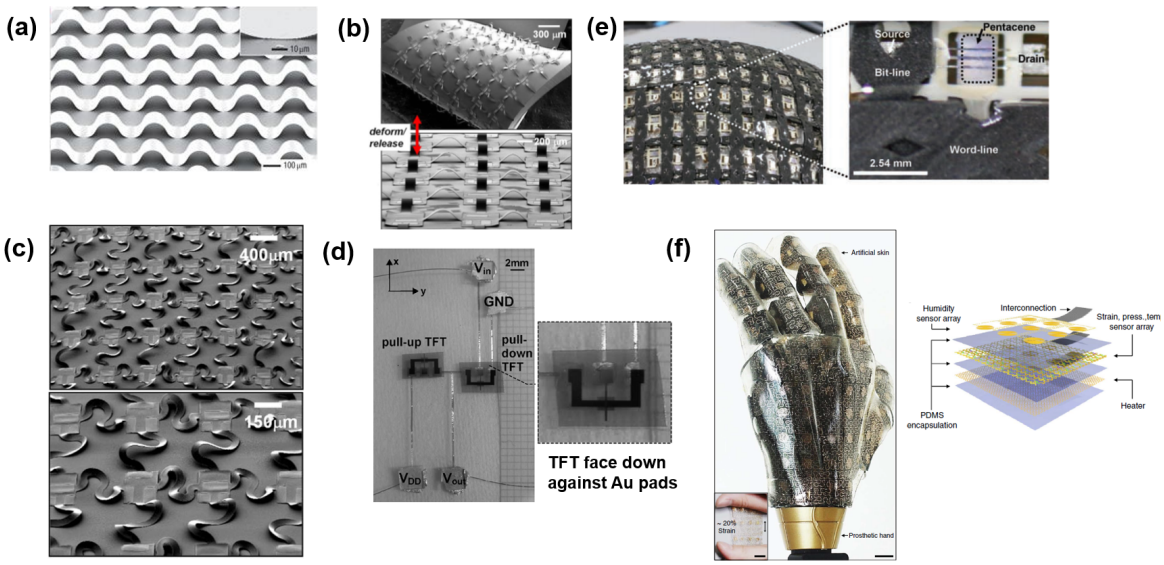

Figure 2.3: Strategies adopted to develop inorganic based stretchable electronics: (a)Buckling of inorganic GaAs nanoribbon on PDMS. The inset shows the bonded region of nanoribbon to PDMS. Reproduced with permission from [68]. (b) and (c) Interconnected rigid island configration- (b) SEM micrograph of CMOS inventor with straight bridge strucutre in normal state and twisted state [70](c) SEM micrograph of CMOS inventor with a serpentine bridge enabling a higher stretchability (bottom image showing a magnified image) [70]. Copyright (2008) National Academy of Sciences. (d) and (e) Use of strectahble interconnects to achieve an improved stretachbility- (d)Amorphous Si TFT on a PI substrate connected by Au interconnect. Reproduced with permission from [71] ©2005 IEEE. (e)Array of organic transistors connected by single wall CNT interconnects and magnified image of single cell in shown in the insert. Reproduced with permission from [72]. (f) Smart patterning of the active sensing material- SiNR based smart multifunctional e-skin on prosthesis. The e-skin comprises stretchable sensors for strain, pressure and temperature, along with humidity sensors and thermal actuators. Scheme shows the cross-sectional of six stacked layers of e-skin. Reproduced with permission from [73].

nanoribbons are attached to prestrained elastomer, which on release of the prestrain results in the nanoribbons buckling due to compressive force, as shown in Figure 2.3a. Besides Si, buckling has also been demonstrated in GaAs, GaN , CNT [68]. Buckling structure is achieved by transferring nanoribbon onto a prestrained elastomer with patterned adhesive sites and upon release of the prestrain on elastomer, nanoribbons with the buckles structure are realised. The adhesive sites are realised by the ozone exposure of lithographically defined regions [69] [68]. Another approach adopted to incorporate inorganic materials for the development of stretchable electronics is the use of interconnected rigid islands, as shown in Figure 2.3b. The active rigid devices on an elastomer substrate are bridged by material with lower stiffness, resulting in an improved stretchability and also enabling complex deformation, such as twisting etc. The stretchability can be further improved by use of a serpentine bridge structure, as shown in Figure 2.3c . The improved stretchability of the serpentine structure is owing to its longer length geometry enabling it to accomodate larger strain [70]. Further serpentine metallic and CNT based interconnects have also be explored in the enabling

of the development of high performance stretchable electronics using intrinsically rigid material [71] [72]. In addition, the performance and reliability of the interconnect could be further improved by encapsulating or embedding the interconnect with another material similar to the substrate [74]. Besides the use of patterned interconnects, stretchability can also be achieved by smart patterning of the active material. Recently, Kim et al demonstrated a silicon nanoribbon (SiNR) based smart multifunctional stretchable e-skin as shown in Figure 2.3f. The developed smart skin comprised SiNR based strain, pressure and temperature sensors for prosthesis applications. SiNRs of different patterns were developed to attain the optimum performance (strain and stretchability), they explored straight and serpentine SiNR structure depending on the stretchability required. In addition, sensors were also equipped with humidity and thermal actuators and platinum nanowire based mutielectrode array for signal transmission, showing its promise towards the development of the smart prosthesis based on inorganic material.

2.4.2 Materials and Techniques Beyond Silicon

Though various strategies have been adopted to incorporate the use of the Si in the development of flexible and stretchable electronics, the use of Si requires meticulous fabrication process, thereby limiting its use and compatibility with other processes associated with large area electronics development such as roll-to-roll printing, inkjet and screen printing etc. This has led to the investigation of unconventional and novel materials in the development of flexible electronics [75]. Polymers such as polyethylene terephthalate (PET) [76], polyethylene napthalate (PEN) [72], polyvinyl chloride (PVC) [22], polyimide (PI) [3, 77] have been investigated as the substrate for the development of flexible electronics, owing to their mechanical flexibility. Besides the aforementioned polymers, another class of material known as elastomers such as PDMS and EcoFlex are another popular choice, owing to their elastic behaviour enabling the development of the conformable electronics with improved elasticiity [23] [78] [79]. Ryu et al [79] demonstrated a highly oriented CNT-based fibre for strain sensing applications. By utilising a pre-strained Ecoflex, strain sensor capable of measuring strain greater than 900% was developed. The use of Ecoflex substrate ensured uniform distribution of strain across the fibre, thereby reducing the stress concentration leading to improved elasticity in comparison to the standalone CNT fibres, which were capable of withstanding only a mere 8% strain. Apart from its use as substrate, elastomer has also been investigated as a dielectric and conductive electrode for physical sensing applications [21] [32] [34]. For typical contact resistance-based resistive pressure sensors, the application of force results in change of contact resistance owing to cross-sectional deformation. The use of conductive microstructure is expected to result in an improved performance, owing to anisotropic configuration. In order to achieve a conductive microstructure, different materials such as thin metallic film [23], graphene [80] and CNT [81] and conductive polymers [82] and polymer composite [83, 84] have

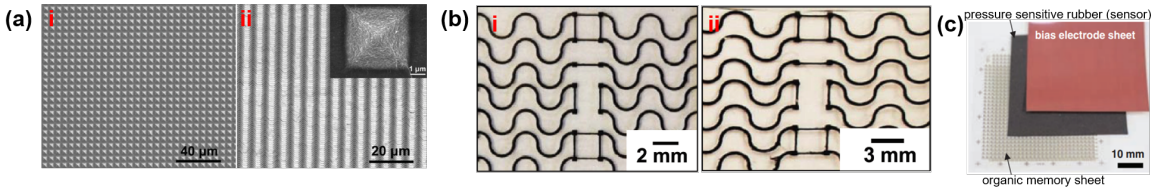

Figure 2.4: The use of novel material which are intrinsically flexible or stretchable to develop flexible/stretchable sensors : (a)Use of microstructured elastomer for improved performance (i) microstructured PDMS (ii) conductive microstructured PDMS with graphene film. Insert shows an individual PDMS microstructure coated with graphene film. Reproduced with permission from [80]. (b)Use of conductive nanocomposites - an all elastomer strain gauge sensor comprising carbon black -PDMS resistor connected with a serpentine CNT-PDMS interconnect (i)unstretched (ii) stretched by 150%. (c)Use of organic semiconductors-OFET based pressure sensor array on PEN substrate, 500μm thick pressure sensitive rubber and top bias electrode of Cu on PEN substrate. Reproduced with permission from [72] ©2009 American Association for the Advancement of Science.

been explored. Figure 2.4a shows a microstructured PDMS with pyramidal structure comprising a graphene film used for the development of high sensitive pressure sensors. Park et al recently demonstrated the use of CNT-PDMS composite based-interlocked microdome pressure sensor array structure resembling the human skin's epidermal and dermal ridges [84]. The developed sensor array was capable of differentiating different mechanical stimuli such as normal, bending, shear and twisting. In addition, a 3×3 array of sensors was demonstrated to show its capability in resolving the spatial distribution and direction of mechanical stimuli, thereby demonstrating the three axial stress sensing capability of the sensor. As mentioned above, the microstructured elastomer has also been investigated as a dielectric for a capacitive sensing application, resulting in an sensitivity 30 times higher in comparison to a capacitive structure with an unstructured dielectric [34].

Besides substrates, new materials have been explored as an active material for the development of physical sensors. Intrinsically, stretchable materials such as conductive rubbers have been employed for pressure/strain sensing application by incorporating conductive fillers such as carbon black, CNT, nanowires within the elastomer [85–87]. The conductive composites can be used to develop stretchable strain sensor comprising of all intrinsically stretchable material as shown in Figure 2.4b. In addition, pressure sensitive rubber (PSR) integrated with OFET [88] [89] (Figure 2.4c), CNT-FET [90], and nanowireFET (NWFET) [91] have also been investigated for the development of FET based pressure sensors.

2.5 FET-Based Pressure Sensors

Pressure sensors have become an integral part of various applications ranging from the consumer electronics, wearable electronic devices, healthcare devices and e-skin

applications. In this regard, various transduction mechanisms described above have been employed in the development of novel pressure sensors. Each transduction mechanisms have their own advantages and disadvantages. For instance, piezoresistive are attractive owing to their simple device architecture and easy readout mechanisms, however are limited by low pixel density. Capacitance transduction mechanisms offer high sensitive sensor with low power consumption, but are highly vulnerable from interference effects from neighbouring pixels. Piezoelectric transduction mechanisms are attractive owing to high sensitivity and fast response time. However, piezoelectric materials often exhibit pyroelectric property, thereby affecting its performance. The aforementioned sensors can be addressed via a passive matrix for large area sensing applications. Unfortunately, a passive matrix are inherently low speed and often affected by cross-talks, leading to incorrect signals. In this aspect, FET-based pressure sensors are an attractive candidate, as they offer significant advantages such as low power, high spatial resolution, high sensitivity, low noise, ease of integration with circuitry and use of FET avoids the cross talks

In this regard, various materials have been explored as an active channel material for the development of FET based pressure sensors. These include organic semiconductors [21] [24] [88] [89], nanowires [57] [91], CNT [92] [93] and graphene [61] [45]. Someya et al first explored the use of OFET for the development of flexible 16×16 active matrix pressure sensors [24]. The active matrix comprised OFET integrated with a pressure sensitive layer, with the OFET being addressed in the following configurations: The gate and drain electrodes of OFET are connected to word and bit lines respectively, while the source is connected to the ground via a pressure sensitive layer. The application of pressure causes the change in the resistance of the pressure sensitive layer, leading to change in the drain current of OFET. In another approach, an organic nonvolatile memory transistor integrated with PSR was used for pressure sensing applications [89]. The active matrix array comprising a floating gate OFET with a hybrid dielectric (consisting of thin AlO_x + self assembled monolayer) was capable of data retention of the pressure distribution even after 12 h of post-application of mechanical force (Figure 2.5a). Besides PSR, pressure sensitive foil integrated with DNTT based OFET have been investigated for the development of ultra-lightweight conformable active matrix pressure sensors (Figure 2.5b) [88]. The developed sensor exhibited high precision and sensitivity, combined with its comfortability, shows OFET potential in applications in the field of robotics and prosthesis. In addition, OFET based pressure sensors are also an attractive candidate, owing to the low cost and compatibility with large area electronics fabrication process.

Despite its advantage, OFET exhibits a low carrier mobility and requires higher voltage for its operation and this has led to investigation of materials with high carrier mobility, such as CNT, nanowire etc. Takei et al [91] demonstrated contact printed Ge/Si core/shell NWFET array on a flexible PI for active matrix for pressure sensing applications. The device exhibited a field effect mobility of 20 $cm^2.V^{-1}.s^{-1}$. Similar

to organic counterparts, the pressure sensitive NWFET was achieved by integrating a PSR enabling the development of an active matrix pressure sensors. Further, in comparison to OFET, the low operation voltage of NWFET is an attractive feature, as it would enable the development of low power sensors. CNT is another attractive material for the development of flexible transistors. Javery and co-workers developed a CNT thin film transistor (TFT) based active matrix user interactive e-skin. The e-skin consists of OLED laminated between the CNT TFT array and PSR [90]. The application of pressure results in the change in resistance of PSR leading to turn-on of OLED (Figure 2.5c(i)). Nela et al adopted a similar strategy to develop a CNT TFT based pressure sensor where the pressure sensitivity was achieved using a highly sensitive PSR for pressure sensing application, resulting in an improved response time [92]. Further, the sensor was developed via a solution compatible process and exhibited a stable response even under bending conditions (Figure 2.5c(ii)). The response time of such pressure sensor is not influenced by the switching time of the FET but rather by mechanical response of PSR. Development of transparent flexible pressure sensors are an attractive feature for various applications such as displays etc., in this regard graphene is an attractive choice owing to its low optical absorption. Sun et al demonstrated a resistive transduction based novel co-planar gate GFET 4×4 pressure sensor matrix [45]. In the co-planar gate GFET, graphene was used as both electrodes(gate, source and drain) and semiconductor with high capacitance ion-gel acting as the gate dielectric (Figure 2.5d). The sensor consists of top layer with a square graphene pattern and a bottom layer with an interdigitated graphene electrode. The application of force brings the top and bottom layer into contact and reduce source drain resistance resulting in an improved transconductance of the GFET. The simple fabrication process, its low power consumption and excellent optical transparency (80%) are attractive features of the reported pressure sensors.

To overcome the hysteresis issues and sensitivity at lower pressure regime associated with PSR integrated pressure sensors, various strategies have been adopted. One such technique is the use of the microstructured elastomer gate dielectric [21] [34]. Schwartz et al [21] developed a conjugated polymer (polyisoindigobithiophene-siloxane) based TFT integrated with microstructured PDMS film to demonstrate a flexible pressure sensor (Figure 2.6a). The application of force resulted in the change in the gate dielectric capacitance of the device which is reflected in change in the drain current of the TFT. Further in the study a pyramidal microstructure with larger inter spacing between microstructure was found to be the optimal as it led to an improved sensitivity due to larger air gap and enhanced compressibility due to higher force on individual pyramids. Such pressure sensors exhibit high sensitivity in the low pressure regime with high response time. Recently, Shin et al demonstrated a novel pressure sensitive GFET array where the air dielectric-graphene interface was formed by use of the origami substrate (Figure 2.6b) [94]. The reported origami structure comprised two panels connected by a foldable elastic joint. One panel consists of source/drain electrodes

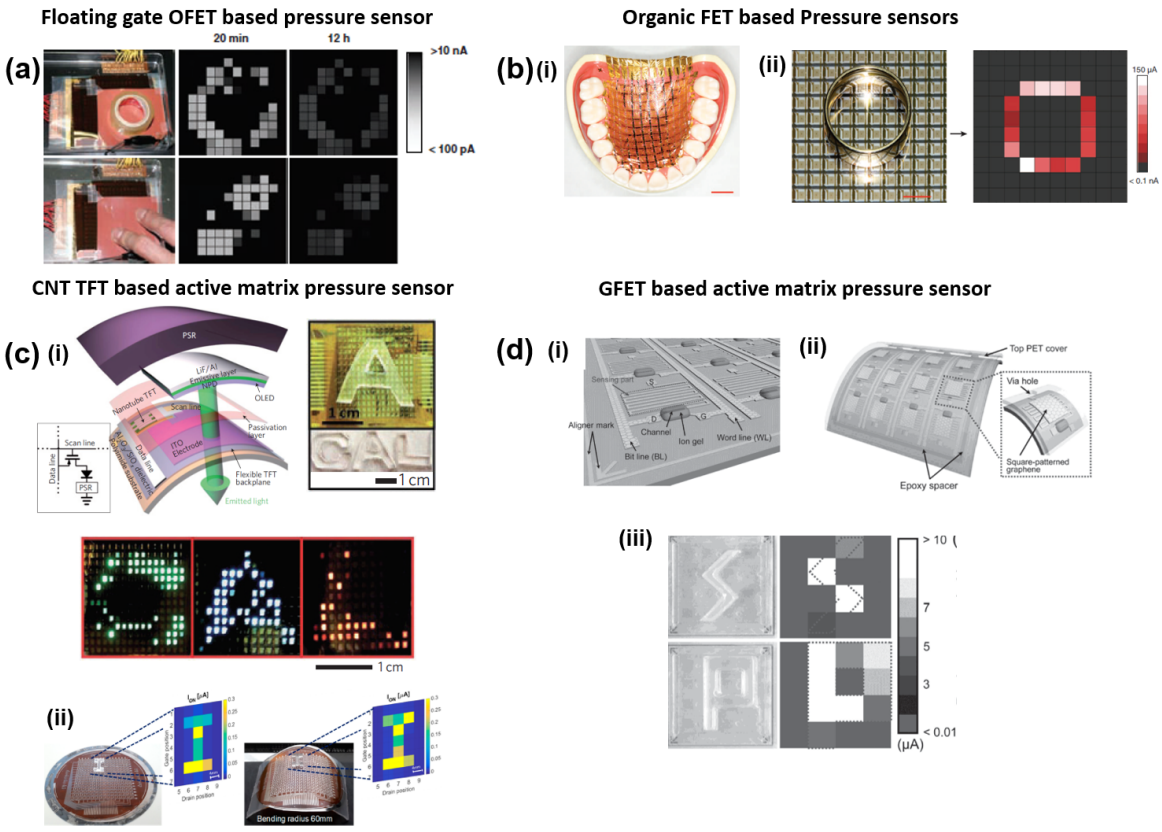

Figure 2.5: Pressure sensitive FET based on piezoresistive transduction mechanisms (a)Floating gate pressure sensitive OFET array with a PSR, capable of retaining the spatial pressure distrution data over 12h even after voltage and applied pressure has been removed. Reproduced with permission from [89]©2009 American Association for the Advancement of Science. (b)Flexible OFET pressure sensor array developed by laminating pressure sensitive foil, thereby enabling ultra flexibility and conformability(i)Flexible OFET array conformably attached to model of human jaw. (ii) Photograph of a metallic ring placed presure sensor array with pressure sensitive foil and resulting change in the drain current of OFET with contact on ring. Reproduced with permission from [88]. ©2013, Springer Nature. c)CNT TFT based active pressure sensor matrix developed by integrating pressure sensitive rubber (i) CNT TFT pressure sensor active matrix integrated with PSR enabling a user visualisation of pressure. Reproduced with permission from [90]. ©2013, Springer Nature.(ii)CNT TFT developed using solution compatible process. The stable response of 16 × 16 CNT TFT based pressure sensor array under normal and bending conditions (60 mm). Reproduced with permission from [92]. (d)(i)Coplanar gate GFET array with gate and drain electrode connected to word and bit line respectively. (ii)Integration of PET consisting of square graphene pattern with a GFET back plane. (iii) Spatial pressure map of the GFET based active matrix [45].

interconnects, graphene channel and an elastomeric partition spacer to define the local air gap between the graphene channel and the gate. The second panel consists of the gate electrode. The application of pressure results in reduction of the air-gap, thereby leading to an increase in metal-air-graphene capacitance, resulting in an increase in the drain current. Further, in comparison to the suspended gate structure reported by Zang et al [95], this structure enables the localisation of air dielectric, therefore providing an opportunity for the development of highly integrated active matrix with

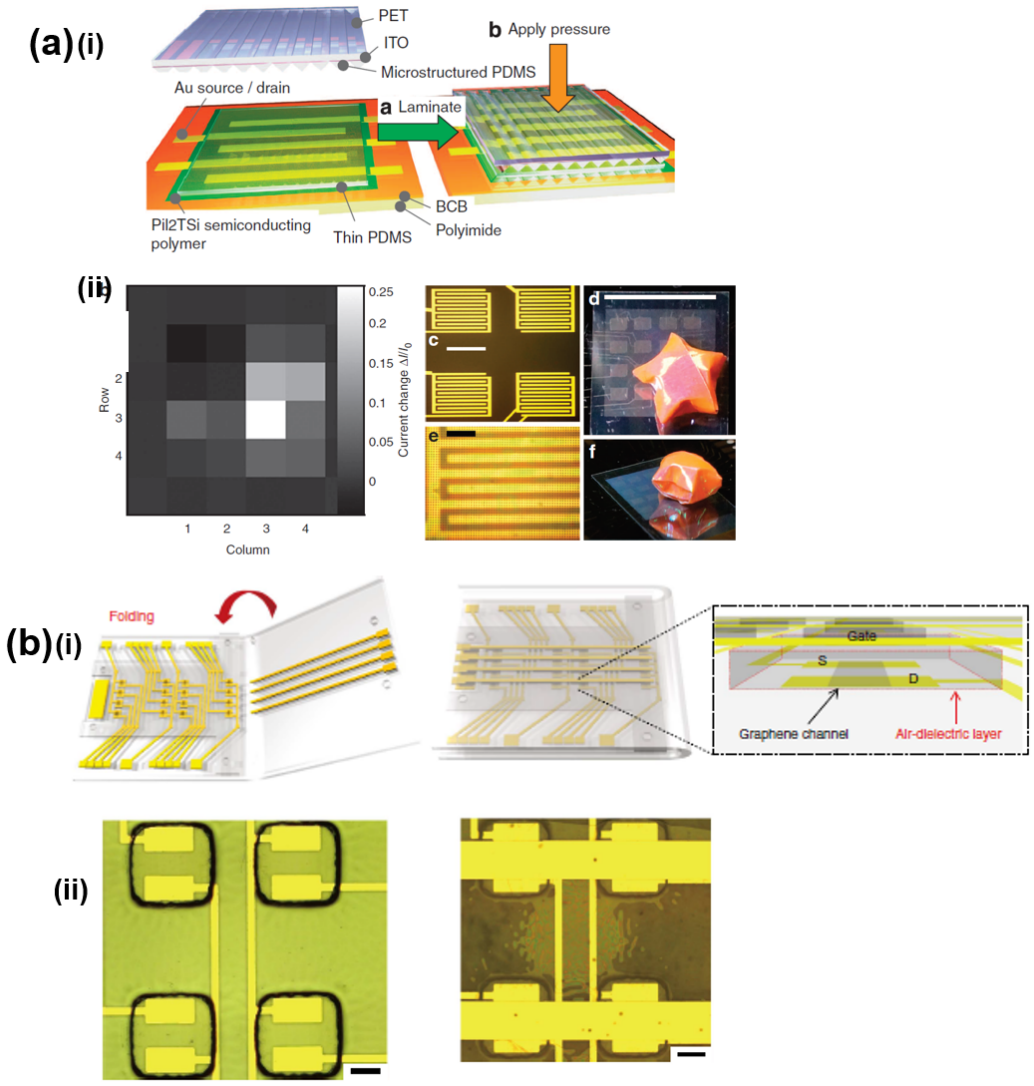

Figure 2.6: Pressure sensitive FET based on capacitive transuction mechanism. Two typical strategies adopted are (a)Use of microstructured gate dielectric (i)Pressure sensitive OFET with microstructure PDMS acting as a dielectric. The application of pressure results in compression of gate dielectric, causing a change in drain current of OFET. (ii)Spatial pressure distribution of the sensor due the change in normalised current on application of pressure (star made of paper). Optical microscopy image of 4×4 pixel and inidvidual pixel are shown on the right. Reproduced with permission from [21]. ©2013, Springer Nature. (b)Localisation of air gap (i)Scheme depiction of origami pressure sensitive GFET with a air dielectric layer-The pressure sensor consist of two panels connected by a foldable elastic joint (ii) Optical microscopy image of GFET with source and drain electrode and air dielectric layer surrounded by PDMS spacer (Left side). Optical microscopy image of GFET with folded gate [94].

an improved resolution.

Piezoelectric is another popular transduction mechanism which has been explored in the development of FET based pressure sensors. Unlike capacitive and piezoresistive transduction mechanisms, piezoelectricity is not affected by the scaling of devices, thereby enabling development of high resolution FET based devices. Wang and co-workers have explored the use of ZnO nanowire's semiconducting and piezoelectric property in the development of flexible electronics applications [57] [96]. Wu et al

demonstrated strain gate vertical piezotronic transistor for tactile imaging, the device comprised of two terminals with a metal semiconductor metal structure resulting in a two Schottky contacts. The application of force results in a generation of piezopotential which modulates the Schottky barrier height, thereby affecting the transport properties. The magnitude of the generated piezopotenial is affected by the applied force, therefore the applied force can act as gate bias modulating the electrical characteristics of piezotronic transistors. In the reported device each pixel is represented by one or two ZnO nanowires which can be addressed individually. Therefore by monitoring the output current of each pixels the spatial pressure distribution could be determined [57]. PVDF and its co-polymers are another popular piezoelectric material widely used for tactile sensing applications. Dahiya et al [58] have explored the use of PVDF-TrFE integrated with Si MOSFET for the detection of dynamic force for e-skin applications. Recently Sun et al [61] demonstrated development piezopotential powered co-planar GFET strain sensor array. The active matrix consist of coplanar-gate GFET and P(VDF-TrFE) based nanogenerator. The sensor consists of P(VDF-TrFE) nanogenerator on top of the coplanar gate of GFET. An application of strain results in generation of piezopotential (acts as a gate bias) which modulates the drain current.

2.6 Graphene: Structure, Properties and Synthesis Methods

Graphene is a 2 dimensional (2D) carbon allotrope which has become a material of significant interest in recent times owing to its unique intrinsic material properties such as those of electrical, thermal, mechanical and optical properties [97–99]. Though thin films of graphite were observed in early 1960s [100], it was not until 2004 that the material received a significant attention when Giem and coworkers demonstrated carrier modulation in a monolayer graphene achieved by mechanical exfoliation [97]. Since then, much progress has been made in graphene research, in understanding its properties, development of new synthesis methods, and use of it in various applications. Graphene has been investigated in various applications such as field effect transistors(FET) and circuits [77,101,102], transparent electrodes [103], chemical sensors [104–107], thermal spreaders [98, 108]. The focus of the thesis is on the development of GFET based pressure sensors. This section will cover the basics of graphene structure, its critical properties with regard to FET, together with various graphene synthesis methods.

2.6.1 Graphene Properties and its Fundamental Significance in FET

Crystal Properties and Electronic Band Structure

Graphene is a 2D carbon allotrope of sp^2 hybridised carbon atom arranged in a honeycomb lattice with a carbon-carbon bond length (L_b) and lattice constant(a) of 0.142 nm and 0.246nm respectively as shown in Figure 2.7. It is basis of other carbon allotropes. The fullerene can be considered as the graphene wrapped into a ball-shape, while carbon nanotube (CNT) is a rolled-up graphene sheet. Graphite can be considered as a 3D stack of graphene layers held together by a weak van der Waals force [109].

Graphene's unit cell consists of two carbon atoms, A and B, which form the basic building block of the honeycomb lattice depicted in Figure 2.7, with each atom consisting of four valence electrons ($2s, 2p_x, 2p_y, 2p_z$). Each carbon atom in the sub-lattice is bonded by σ bonds to 3 other carbon atoms in the neighbouring sub-lattice, resulting in the formation of the deep lying valence band of graphene. The graphene's mechanical property is attributed to σ bond. The overlapping $2p_z$ electrons of neighbouring carbon atoms results in the formation of the bonding (π) and antibonding (π^*) orbitals, which form the valence and conduction band of graphene. Therefore, graphene's electronic and optical properties are determined by the electrons in the $2p_z$ electrons [110]. The π and π^* overlap at the corners of Brillouin zone indicated as K and K' (momentum vector), around which they exhibit a linear dispersion, as depicted in Figure 2.8.

The graphene's electronic property can be described by tight binding Hamilton equation given in Equation 2.1 [112].

$$E^{\pm}(k_x, k_y) = \pm\gamma_0\sqrt{1 + 4cos\frac{\sqrt{3}k_x a}{2}cos\frac{k_y a}{2} + 4cos^2\frac{k_y a}{2}} \tag{2.1}$$

where a=$\sqrt{3}a_{c-c}$, where a_{c-c} is bond length (0.142nm), γ_0 is the transfer integral typically between 2.9 eV to 3 eV, k=(k_x, k_y) vectors of the first hexagonal Brillouin zone [112]. As mentioned above at K points in Brillouin zone, a linear energy dispersion(in contrast to prabolic dispersion observed in metal and semiconductor) is observed and the electrons behave like Dirac Fermions (Electrons with no rest mass)moving at the Fermi velocity given below. The linear energy dispersion can be approximated as given in Equation 2.2 [112]

$$E(k) \approx \pm\hbar\upsilon_f|\kappa| \tag{2.2}$$

where υ_f is the Fermi velocity of charge carriers in graphene, $\upsilon_f = 1\times10^6 m/s$, where the positive and negative sign represents the valence and conduction band receptively. Each carbon atoms $2p_z$ orbital consists of only one electron and as valence and conduction

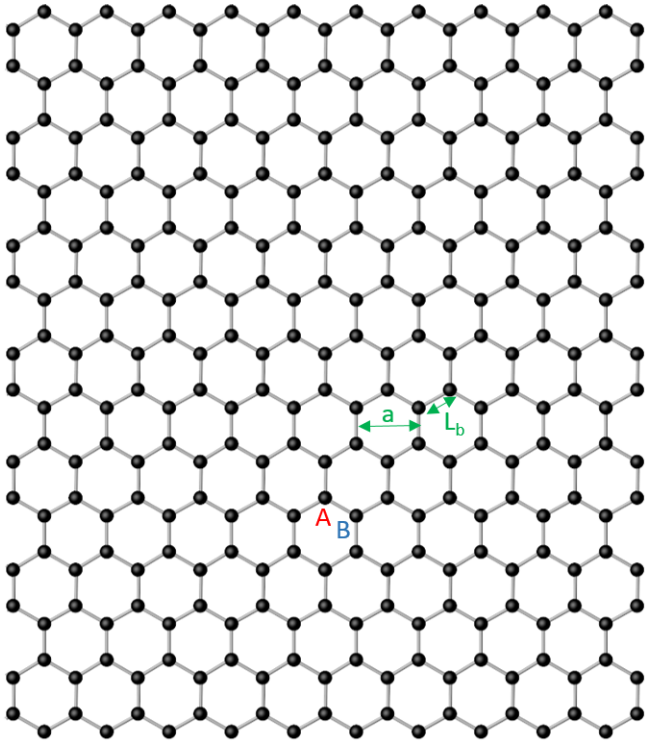

Figure 2.7: Schematic of graphene's atomic structure with carbon atoms arranged in a honeycomb lattice.

band touch at K and K', graphene can be considered a zero band gap semiconductor or semi-metal.

The electronic density, n, is related to the Fermi momemtum,k, by $k^2/\pi = n$. Therefore Equation 2.2 can be rewritten as $E(k) \approx \pm\hbar v_f\sqrt{\pi n}$ [111]. The Fermi Level in graphene can be modulated by application of electric field, thus resulting in an observed ambipolar behaviour in graphene, where the charge carriers can be altered between holes and electrons even at a high carrier density as high as $10^{13}cm^{-2}$ [113]. Sweeping the gate voltage of GFET from a negative to positive bias results in the shift of the Fermi level from the valence band to the conduction band passing through a point called Dirac point, where the valence and conduction band touches and conduction changes from p-type to n-type. The conduction is at minimum at the Dirac point. Further, the linear dispersion observed in graphene results in the vanishing density of states. This necessitates a large Fermi energy shift to achieve the required change in electronic density. Therefore in GFET when determining the total gate capacitance, C_g, it is also critical to include the graphene's quantum capacitance, C_q, in series with gate oxide capacitance,C_{ox}, especially for thin gate oxide. Therefore the total gate capacitance is given by $C_g = (C_{ox}.C_q)/(C_{ox}+C_q)$, leading to a smaller gate capacitance in comparison to C_{ox}. In graphene the quantum capacitance $\approx 2\mu F/cm^2$ in density range n$(0.5 - 10^{12}cm^{-2})$ [114] .

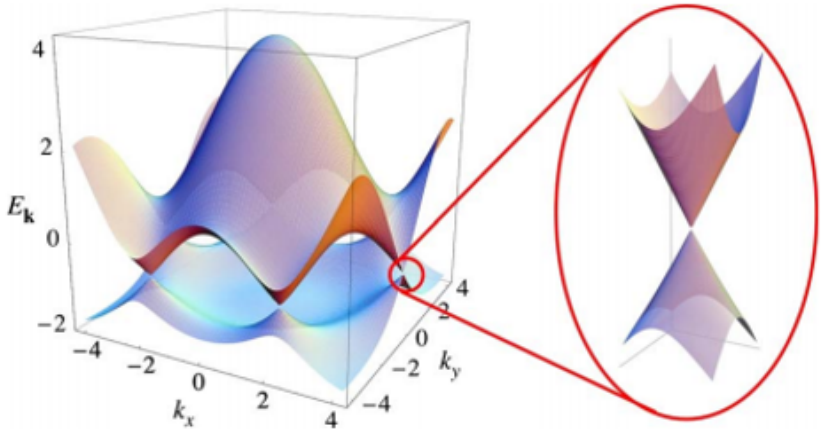

Figure 2.8: Graphene's band structure :Based on the tight binding and linear dispersion behaviour near the Kpoint. Reprinted with permission from [111].Copyright(2009) by American Physical Society.

Bandgap

Graphene is a zero-bandgap material as a result of overlap of valence and conduction band at K and K' near the Brillouin zone. This zero bandgap nature results in graphene FET with high off-current, thereby resulting in low I_{on}/I_{off} roughly around 5-10 limiting its use in the digital logic operations. Three techniques widely used for opening of bandgap in graphene are: by applying perpendicular electric field in bilayer graphene; by applying a strain in monolayer graphene, by graphene nanoribbons (GNR).

Bilayer Graphene Graphene can be classified as either mono-,bi- and few layer graphene(upto 5 layer) depending on the number of graphene layer stacked on top of each other. Similar to monolayer, the bi and few-layer graphene also exhibit unique electronic and phonon properties . In addition to the number of layers, the stacking arrangement of graphene layers also influences its electronic property [115]. Three possible stacking arrangements are Bernal stacking(AB stacking), AA stacking and rhomobohedral stacking (ABC stacking) [115, 116]. In a Bernal stacking configuration only half of the sub-lattice overlap while the other sub-lattice lies just above the centre of the underlying layer. In an AA configuration both sub-lattices of the stacked layer exactly overlap each other. The stacking arrangement of Bernal and rhomobohedral is shown in Figure 2.9. Similar to monolayer graphene, bilayer grpahene is gapless in nature and exhbits a parabolic dispersion near the K point. However, it is possible to open a non-zero bandgap in a Bernal stack bilayer graphene by application of the perpendicular electric field across a bilayer graphene via dual gated GFET [117, 118]. Further, by applying high perpendicular electric field a gate tunable bandgap (250meV) can be achieved in a bilayer graphene [119].

Graphene Nanoribbon Graphene nanoribbon (GNR) is another technique that would enable the opening of bandgap in graphene. The bandgap of the nanoribbon is

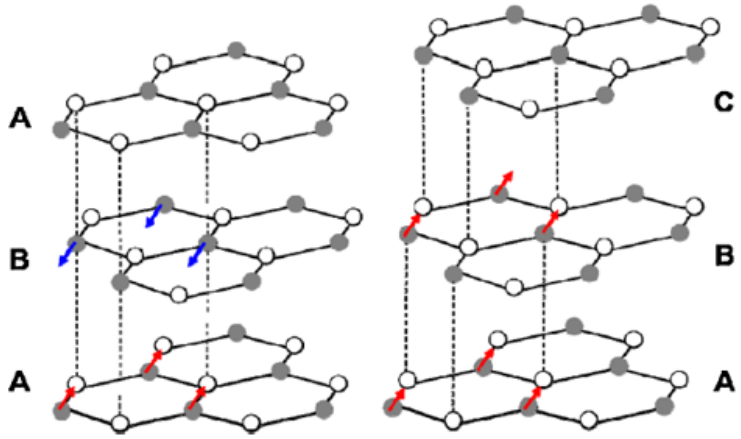

Figure 2.9: Stacking arrangement of a few layer graphene- Bernal structure(left) and rhomobohedral structure (right). A,B and C indicate the distinct position in the hexagonal lattice. Reprinted with permission from [116].Copyright(2010) by American Physical Society.

inversely proportional to the nanoribbon width. A bandgap opening of 200 meV has been demonstrated for 20 nm width GNR. In addition, a I_{on}/I_{off} as high as 10^6 has been demonstrated in 10 nm width GNR. However, very often GNR suffers from edge roughness and width along its length, which influences its electrical property. Therefore a GNR with similar specifications would have different electronic properties, resulting in significant device to device variations. Further, defining a GNR with well-patterned width and smooth edges is very challenging task even with the current state-of-the-art facility.The larger band gap opening in GNR comes at a cost of reduced mobility, which has been the attractive feature of graphene. This reduced mobility is due to the valence and conduction band becoming more parabolic around K point, thereby resulting in an increased effective mass and lower mobility. Therefore, limiting its application in the near future.

Carrier Mobility

One of the significant reasons behind the huge interest in graphene is its high carrier mobility at room temperature. Initial studies using exfoliated graphene samples on SiO_2 show high carrier mobility in the range of the $1 - 2 \times 10^5 cm^2/V.s$ [97, 120]. The mobility could be further enhanced in the absence of external factors such as charge impurities, substrate induced effects. This could be achieved in suspended graphene where high mobility in the range of 200,000 $cm^2/V.s$ were reported with low temperature measurements [121], while a room temperature measurement on suspended graphene exhibited a mobility of 120,000 $cm^2/V.s$, which is the highest for room temperature measurement of any semiconductor [122]. In addition, high carrier mobility in excess of 12,000 $cm^2/V.s$ has also been demonstrated on flexible top-gated CVD graphene GFET [102]. This exhibits graphene's potential in future electronics. Despite its impressive carrier mobility, its zero bandgap nature remains

a major bottle-neck in the realisation of graphene-based devices, especially in digital logic applications.

2.6.2 Graphene Synthesis

The first isolation of graphene was reported by Geim and co-workers in 2004 [97]. This was achieved by mechanical exfoliation of graphene from a highly oriented pyrolytic graphite (HOPG). Since then, various techniques have been reported for fabrication of graphene. Based on the graphene synthesis method it can be classified as either top-down or bottom-up approach. In top-down approach, graphene sheets were isolated from a graphitic material. This is achieved by overcoming van der Waals force between the graphitic layers. In a bottom-up approach, graphene is synthesised from a carbon containing source. Methods such as micromechanical exfoliation, chemical exfoliation of graphite oxide are classified as top-down methods, while the CVD and epitaxial growth of graphene are classified as bottom-up methods. This section will cover the four major synthesis techniques widely adopted in graphene research.

Micromechanical Exfoliation

Micromechanical cleavage, credited with the first isolation of graphene, involves the repeated peeling of layer/layers of graphene from HOPG using an adhesive tape to break the van der Waals force between the graphitic layers. The exfoliated samples result in a very high quality graphene with a ballistic transport at sub micrometre range. However, the exfoliated graphene flakes are of irregular shape and size, and fabrication of devices require individual selection and patterning of devices, thus limiting its use in industrial applications. This method is primarily used for basic studies of graphene [97].

Chemical Exfoliation of Graphite Oxide

This is one of the most popular methods widely adopted to achieve graphene. Graphene oxide is prepared by the reduction of graphite oxide (GO). Traditionally, graphite oxide has been prepared by 3 methods, namely Brodie [123], Hummers [124] and Staudenmaier [125]. Of these three methods, Hummer is the most popular method, where graphite is oxidized in the presence of sulfuric acid, sodium nitrate and potassium permanganate. The oxidation causes the disruption of sp^2 carbon network and introduces hydroxyl and epoxy functional groups to carbon network [126, 127]. Following this process, graphene oxide is exfoliated by sonication treatment of GO. Finally, graphene is obtained by the reduction of graphene oxide, which is generally achieved either via UV treatment [128, 129] or by chemical and thermal treatment. Some of the widely-used reducing agents are hydrazine [126] [130], dimethylhydrazine and sodium borohydride (NaBH4) [131]. Thermal reduction of graphene oxide is achieved by rapid thermal treatment at 1100^oC [126]. Graphene obtained by this

process is generally referred to as chemically reduced graphene, or chemically modified graphene as complete reduction of graphene does not occur during this process.

Liquid Phase Exfoliation

Liquid phase exfoliation (LPE) involves the exfoliation of mono to few layer graphite flakes by shear force of graphite in a solvent with the surface tension. This techniques was first reported in 2008 and has been a popular synthesis route for large scale manufacturing of grpahene [15, 132]. The successful exfoliation of the process relies on the intermolecular interaction between the solvent and the flakes, therefore an appropriate choice of the solvent is critical. Amongst the various solvent investigated the N-meythyl-pyrrolidone (NMP) was demonstrated to be best solvent for the exfoliation and stability while cyclopentanone exhibited the formation of dispersion with highest concentration [133]. In addition aqueous solution with surfactant have also been explored in LPE, thereby avoiding the use of any harmful or expensive chemicals. LPE requires application of the shear force to overcome the van-der Waals force between the interlayers. In this regards various techniques have been explored, amongst which sonication is one of the popular technique. Besides the appropriate solvent, the graphene concentration can also be increased by synthesis methods. Probe sonication has been demonstrated to result in higher concentration in comparison to the bath sonication. Further, a longer sonication time also results in the higher concentration, however this requires a trade-off between the quality of graphene flakes and concentration [134, 135].

Epitaxial Growth of Graphene on Silicon Carbide

Epitaxial growth of graphene (EG) on silicon carbide (SiC) surface is one of the viable methods for wafer scale growth of graphene [136, 137]. Besides, the dielectric nature of SiC is an added advantage, as it would enable direct fabrication of graphene devices, therefore evading the detrimental effects of the transfer printing process [138]. The growth of graphene on SiC surface is often achieved at high temperature ($1200^oC - 2000^oC$) and ultra-high vacuum (UHV) [139, 140]. However, recently the use of argon atmosphere has been as shown to result in a better graphene quality [138].

EG on SiC surface occurs following the decomposition of SiC surface, during which the Si atom desorbs and the lingering carbon atoms rearranges and bonds together to form a thin film of carbon atoms. Graphene growth on SiC can occur at both Si- (SiC(0001)) [136] [141] and carbon(SiC($000\bar{1}$)rich surface [142, 143], which will determine the final structure of graphene [144].

In Si rich surface, graphene growth occurs at regular orientation of 30^o to SiC forming a Bernal stacking. The first layer of carbon atom formed is called the 'Layer 0'or a 'buffer layer'. This consists of sp^2 hybridised carbon atoms. This layer provides the insulation to the subsequent layer of carbon atoms from the dangling bonds of

the SiC surface. Therefore, Layer 1 of carbon atoms is the one which truly mimics the characteristics of graphene's honey comb lattice [145]. However, uniformity of the graphene is disrupted following the growth of 2nd layer of graphene. This is due to reduction of Si atom desorption from the buried SiC layer [144].

Similar to SiC(0001), graphene growth on a carbon rich surface of SiC, SiC($000\bar{1}$), is also initiated following the growth of a buffer layer [145]. Unlike in the SiC(0001) face, in a carbon-rich face, rotational stacking of layers is much more complex, which results in better electrical conductivity than the graphene grown on the Si rich face. In addition, faster kinetics of graphene formation in the carbon-rich face leads to non-homogeneity in graphene growth [144].

EG on SiC is an attractive fabrication procedure, however, for it to be truly adapted for industrial application requires a number of issues to be addressed. Amongst these issues are greater control over uniformity over graphene thickness, cost of SiC, high growth temperature etc. Jang et al demonstrated that graphene growth can be achieved at a significantly lower temperature by depositing a thin film of Ni on SiC [146].

Chemical Vapour Deposition (CVD)

CVD growth of graphene is one of the most promising routes for large area growth of graphene. It involves the pyrolysis of hydrocarbon gas at a high temperature in the presence of a metal. The synthesis of graphene has been demonstrated on various metals - Cu [147, 148], Ni [149, 150], Fe [151], Co [152], Rh [153], Ir [154], Pt [155] and Au [156]. Amongst these metals the inexpensive Ni and Cu have become popular choices for the growth of graphene. CVD growth mechanism of graphene on a metal surface can be categorised as either carbon segregation or surface catalysis.

Graphene growth on Ni and other materials like Co, Fe are due to carbon segregation. Carbon solubility in Ni is a temperature-dependent process [157]. At a high temperature, carbon dissolves in Ni, forming a solid solution of metastable Ni_3C [158]. As the temperature cools down, the solubility of carbon decreases, leading to the precipitation of carbon atoms. In addition, to the experimental parameters the crystallinity of Ni is also critical, as it has a direct influence on the number of layers in the graphene. Graphene growth on single crystal Ni is more uniform and results in a thinner graphene layer, whereas polycrystalline Ni favours multi-layer graphene growth. This is due to the presence of grain boundaries, where carbon precipitation is much higher in comparison to the grain, leading to an inhomogeneity in thickness of graphene across the sample [159]. In addition to crystal structure, cooling rate is another parameter which influences the graphene growth. A faster cooling rate can suppress the formation of multilayer graphene [160].

In contrast to Ni, the CVD growth on Cu is due to the self-limiting surface catalysis process. Unlike Ni and other aforementioned metals, Cu exhibits very low solubility to carbon atoms, hence the graphene growth is primarily limited to a single layer graphene on a copper surface. Among various reported methods, CVD growth of

graphene is very appealing, as it enables large area growth of high quality graphene. Recently, Bae et al [13] demonstrated a growth of 30 inch graphene film on a Cu foil. In order to utilise fascinating properties of graphene for electronic application requires the graphene to be transferred to an appropriate substrate. A number of procedures have been reported for transfer printing of graphene. The transfer printing process adopted for the development of graphene will be discussed in detail in forthcoming chapter.

2.7 Chapter Summary

Development of pressure sensors has become an area of immense interest owing to its potential applications in a range of fields such as robotics, prosthesis, devices for human-machine interaction, wearable and health care electronics. Motivated by the potential of the aforementioned applications has led to the development of flexible pressure sensors. In this regard, two strategies have been adopted for the development of flexible electronics. They are smart structural engineering of conventional electronic material to develop flexible electronic devices and use of novel materials which are intrinsically flexible or stretchable. Some of the key techniques that have been adopted in the development of flexible and stretchable electronics have been discussed in detail in this chapter.

A number of transduction mechanisms and techniques have been adopted for the development of flexible pressure sensors. Amongst them, FET based pressure sensors are an attractive choice as they enable high spatial resolution, high sensitivity, fast response and enable facile integration with the circuitry. In addition, FET based sensors are less susceptible to interference from neighbouring pixels and enable the development of large area active matrix array which could truly mimic the human skin. Predominantly, FET based pressure sensors have been developed using the 3 main strategies: integration of pressure-sensitive rubber with FET; use of microstructure elastomer as a gate dielectric; integration of piezoelectric material with FET. Some of the key prerequisites for the development of pressure sensors for e-skin applications are: mechanical flexibility/stretch ability; high sensitivity; fast response; low operation voltage; low power consumption. In the case of the latter two requirements, self-powered sensors based on triboelectric and piezoelectric transduction mechanisms have been investigated.

The initial work on the development of flexible FET based pressure sensors were fuelled by organic semiconductors. However, the low carrier mobility and high operation voltage often associated with OFET has led to investigation of other materials such as CNT, nanowire, and graphene. In this regard, graphene is an attractive material owing to its fascinating material properties. Amongst the different properties its electronic property, where high carrier mobility as high as 200,000 $cm^2/V.s$ has been demonstrated in suspended graphene, making it possibly one of the most promising materials for the post-silicon era. The high carrier mobility of graphene

is due to its linear energy dispersion near Dirac point, where the charge carrier behaves like Dirac Fermions with a Fermi Velocity of $1 \times 10^6 m/s$, with mean free path in order of micrometres (ballistic transport). The development of an appropriate synthesis methodology is critical for the adaptation of graphene for large area electronics. In this regard, CVD growth of graphene is an attractive route as it would enable cost-efficient large area growth of high-quality graphene satisfying the industrial requirements. The zero bandgap nature of graphene would enable the development of GFET based pressure sensors that could be operated at a low gate voltage (piezopotential). Further, CMOS compatibility of graphene would allow facile integration of material with the existing CMOS technology. The low optical absorption of graphene would enable the development of transparent pressure sensors.

In summary, this chapter covers various strategies and techniques adopted for the development of flexible/stretchable sensors in physical sensing applications. In particular, a discussion on the FET based pressure sensors for e-skin applications has been reviewed. In this regards graphene is an attractive choice as an active channel material for FET applications owing to its fascinating intrinsic material properties. In this context, electronic property of graphene in regard to FET application has been discussed. Further, popular synthesis methods widely adopted for graphene synthesis has been discussed.

Chapter 3

Fabrication and Characterisation Techniques

3.1 Introduction

This section presents an overview of different fabrication and characterisation techniques adopted for the development of graphene field effect transistor based pressure sensors. In addition, a brief description of principle governing the techniques for the development of graphene-based pressure sensors is presented. A commercially available CVD graphene from Graphenea was used for the development of GFET. This chapter presents the optimised processes adopted for the development of the pressure sensor.

3.2 Fabrication Techniques

3.2.1 Transfer Printing of Graphene

The fabrication process of GFET is initiated with graphene transfer process. This is one of the critical steps in the realisation of CVD grown monolayer graphene (MLG) as graphene quality is often compromised during the process, due to polymeric residues, tears and wrinkles formed on graphene. Graphene transfer was achieved by adopting a wet transfer printing process using cellulose acetate butyrate (CAB). CAB dissolved in the ethyl-l-lactate (2w.t%)was spun on on top of graphene/Cu substrate at 4000 rpm for 30s cured overnight at room temperature. Typically, CVD growth results in graphene on both sides of the Cu substrate which hampers the etching of Cu during the transfer process. Therefore, post-curing of the polymer, graphene on the reverse side of Cu was etched using reactive ion etching (RIE) tool, Oxford Instruments RIE 80+. The underlying Cu substrate was etched in 0.5 M iron (III) chloride solution. The CAB/grpahene stack was rinsed for 15 min in RO water. The stack was then transferred to a modified RCA 2 solution comprising $H_20 : HCl : H_2O_2$ in 20:1:1 ratio for 15 min to remove residual of metallic contaminants [161]. The stack was rinsed

in RO water for a further 15 mins and finally transferred to the target substrate. The substrate was then baked at 50°C for 5 min in a hot-plate and annealed in an N_2 ambient oven at 80°C for 1 h. Finally, polymer scaffold was removed via a 8 h immersion in acetone.

3.2.2 Graphene Etching

Plasma-based dry etch techniques have become the widely-accepted standard within the semiconductor industry. This is due to its ability to scale up for industrial application and its directional etching ability, thereby, enabling highly accurate direct translation of photoresist pattern with high aspect ratio. Reactive ion etching (RIE) is a plasma based dry etch process. RIE system consists of generation of plasma between two parallel plates (one biased and other grounded) by radio frequency (RF) voltage.Plasma is generated by dissociation of the source gas by RF field under vacuum, resulting in the formation of ions, excited neutral and electrons, which play a key role in the etching process. The high mobility electrons in plasma respond rapidly to changing potential and this results in the formation of the negative potential at the substrate surface. This formation of the negative potential attracts the ions in the plasma towards the substrate, resulting in ion bombardments culminating in the removal of the substrate atoms. Further, excited neutrals chemically react with the substrate surface forming volatile products (which are pumped out) thus resulting in the removal of the substrate surface. As the ions travel at 90° towards sample, it results in the anisotropic etching. The patterning of graphene is an important step in the realisation of electronic devices. It involves both definition of GFET channel and isolation of individual devices. Typically, patterning of MLG is often achieved via RIE in O_2 or Ar plasma [162]. Graphene etching was achieved using Oxford Instruments RIE 80 +. Table 3.1 depicts the etching parameters employed for etching of graphene transferred onto SiO_2/Si or polyimide substrate . The etching of graphene was achieved using 4 nm of Al and S1805 as the etch mask during the RIE etch process. Post etching, photoresist is removed by immersing the sample in Microprosist resist stripper 1165 at 50^oC. Figure 3.1 shows the optical micrograph of the patterned graphene channel.

Parameters	Value
Gas	O_2
Pressure (mTorr)	50
Gas flow (sccm)	50
RF Power (W)	300
Temperature (^oC)	20
Etch time (s)	15

Table 3.1: Reactive ion etching recipe of graphene

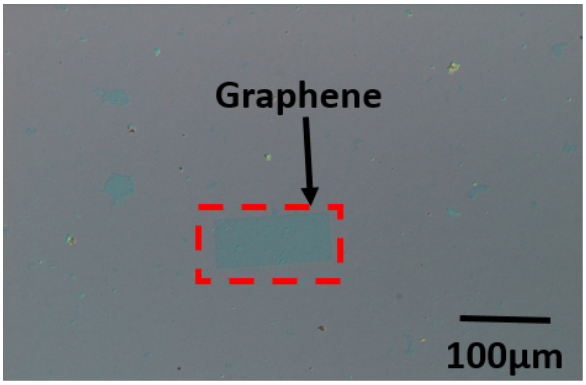

Figure 3.1: Patterned graphene channel via RIE etching

3.2.3 Photolithography

The development of electronic devices relies on the ability to selectively deposit or etch material from a particular location. This selective deposition and etching of the material is achieved by pattern definition on the substrate via lithography. Optical lithography involves the transfer of pattern from a photomask onto a photoresist coated substrate. This is achieved using a mask aligner which aligns the photomask with respect to the substrate, following which the substrate is subjected to a UV radiation exposure. Depending on the photoresist type, the UV exposure radiation can have a different impact on the solubility of the resist. UV exposure on positive resist results in the solubility exposed region, while in negative resist, the exposed region becomes insoluble [163]. The photolithogrpahy process flow adopted for graphene is shown in Figure 3.2.

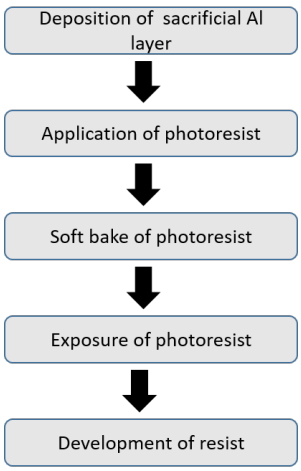

Figure 3.2: Process flow of photolithography steps on graphene

The intricate details of the photolithography on graphene is described below.

(i) **Deposition of sacrificial Al layer:** Photoresist residue on graphene has a detrimental effect on the transferred graphene. Therefore, to reduce the residual remains of photoresist, a 4 nm of sacrificial layer of Al is deposited via electron beam (e-beam) evaporation on top of the graphene. This sacrificial layer of Al

is removed by the photoresist developer (MF319) during the resist development process.

(ii) **Application of photoresist:** This is one of the critical steps in photolithography. This process starts with the preparation of the surface. The substrate surface is modified by application of hexamethyldisilazane (HMDS), which forms a monolayer of the HMDS, resulting in a hydrophobic substrate surface. A few millilitres of a positive photoresist is pipetted on the substrate and spin coated, resulting in an uniform layer of photoresist. During this process, the majority of the solvent is evaporated with residual solvents removed by the subsequent soft bake process. Further, an appropriate choice of the spin speed is vital as it determines the thickness of the photoresist.

(iii) **Soft bake of photoresist:** The photoresist is cured at 115°C on a hotplate. Soft bake evaporates the residual solvent and improves the resist's adhesion to the substrate.

(iv) **Exposure of photoresist:** During the exposure steps, the patterns from the photo-mask is transferred to a 3D pattern onto photoresist on exposure to UV radiation. As mentioned above, the exposure to UV radiation alters the photoresist, due to photochemical reaction, thereby affecting its solubility in the resist developer. The exposure time varies with resist, often with thicker resist requiring higher exposure time.

(v) **Resist Development:** Post exposure, the resist is developed resulting in selective removal of the resist from the substrate.

Two different resists and primers were investigated during the project. The photoresist Shipley S1805 and S1818 were investigated. The choice of the resist and primer were determined by its application. The details of the photolithography process adopted for different resists is summarised in Table 3.2. The exposure was carried out using the mask aligner Suss MA6.

Parameters	HDMS & S1818	HDMS & S1805	MS Primer & S1805
Spin Speed	HMDS @ 4000 rpm for 30 s & S1818 @ 4000 rpm for 30 s	HMDS @ 4000 rpm for 30 s & S1805 @ 4000 rpm for 30 s	MS Primer @ 4000 rpm for 5 s & S1818 @ 4000 rpm for 30 s
Soft bake	115°C for 3 min	115°C for 1 min	115°C for 1 min
Exposure time	6 s	2.3 s	2.3 s
Developer	MF319	MF319	Shipley Microposit developer concentrate: H_2O (1:1)
Development time	150 s	75 s	75 s
Application	Source/Drain electrodes deposition	Graphene channel patterning	Top-gate electrode deposition

Table 3.2: Photolithography recipe

3.2.4 Metallisation, Lift-off and Etching

Metallisation was used for the definition source and drain contacts, gate electrodes and deposition of metal etch mask for the graphene channel definition. Typically, metallisation is carried out using various techniques, such as e-beam evaporation, sputtering and thermal evaporation. The metal deposition was carried out primarily using two main tools, namely Plassys MEB 400S Electron Beam Evaporator and Plassys MEB 550S Electron Beam Evaporator under a high-vacuum environment (2×10^{-6} mbar). The definition of metal pattern is achieved either via lift-off or etching.

Lift-off is one of the widely-adopted techniques for the definition of metal patterns on the substrate. It involves a blank deposition of metal over a sacrificial patterned photoresist. After the deposition of the metal, the resist is solvated in an appropriate solution (acetone or resist stripper) and lift-off. During this process, metal film not in contact with the substrate is removed resulting in the required metal pattern. In addition, metal pattern definition via lift-off requires a poor step coverage, in this regard e-beam evaporation is preferred as a metal deposition technique. Figure 3.3 depicts the metal lift-off process. The optical microscopy image of the electrodes pattern achieved by the lift-off process is shown in Figure 3.4

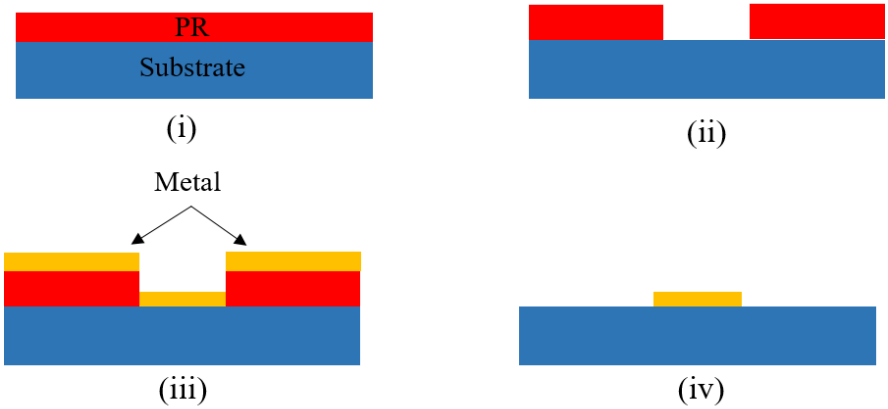

Figure 3.3: Metal-pattern definition via lift-off (i)Photoresist spin coated on top of the substrate. (ii) Development of photoresist post exposure resulting in desired profile for metal deposition. (iii) Evaporation of metal (iv) Dissolution of the resist and metal lift-off leaving the desired metal pattern.

Metal etching is another widely-used technique for the metal patterning. This involves the deposition of the metal over the substrate, following which the metal patterns are achieved by photolithography. The photoresist patterns serve as the etch mask during the etch process, thereby enabling the development of the required patterns. This process was employed for the definition of the Al etch mask used for graphene channel patterning. Al was etched during the photoresist development process by the developer, leaving the desired Al pattern on the substrate.

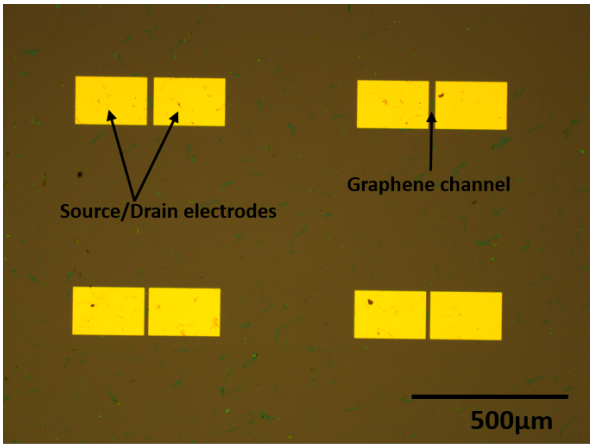

Figure 3.4: Optical microscopy image of source/drain electrodes defined by lift-off.

3.2.5 Atomic Layer Deposition

Atomic layer deposition (ALD) is one of the popular choices within the semiconductor industry for the deposition of the thin film material, owing to its extreme control over material thickness, conformality and composition. ALD belongs to the family of CVD. Unlike CVD, where chemical precursors are purged into the reaction chambers simultaneously and continuously, in ALD the chemical gaseous precursors are sent in the sequential manner, resulting in the surface limited growth process [164]. A typical ALD growth cycle comprises the following [164] :

(1) The first precursor is pulsed into the reaction chamber under vacuum. The precursor gas reacts with the substrate surface in a self limiting growth process resulting in a monolayer on the substrate surface, with no further surface sites available for chemisorption .

(2) Purging of an inert gas such as N_2 to halt the reaction and to remove unreacted precursor and reaction bi products.

(3) The second precursor pulsed into the chamber, resulting in the formation of the required material

(4) 2^{nd} Purging of the inert gas.

Each ALD cycle typically results in the growth of a few angstrom thickness of the desired material. Therefore, the above cycle is repeated until the desired thickness is achieved.This sequential nature of ALD enables the deposition of high quality conformable film. In addition, due to the absence of gas phase reaction particles, ALD enables the growth of pinhole free thin films. Owing to the aforementioned reasons, ALD has become an attractive choice for the growth of high k gate dielectic material for electronic device applications.

ALD growth of Al_2O_3 is a popular choice for the gate dielectric application. ALD growth of Al_2O_3 was carried out in Oxford Instruments FlexAL Atomic Layer

deposition tool. Low damage thermal ALD was used for the deposition of Al_2O_3 as top gate dielectric for the GFET. Thermal ALD growth of the Al_2O_3 was carried out using the trimethylaluminium (TMA) ($Al(CH_3)_3$) and H_2O (water vapour) as the gaseous precursor at 200°. Significantly, this low temperature growth process is advantageous for the development of flexible electronic devices and sensors. The critical parameters of the ALD Al_2O_3 growth process is summarised in Table 3.3 given below.

Parameters	Value
TMA Dose Time (ms)	20
1^{st} Purge time (s)	3
H_2O Dose Time (ms)	150
2^{nd} Purge Time (s)	9
Pressure (mTorr)	80
Temperature (°C)	200
Growth Rate/cycle (nm)	0.1

Table 3.3: Thermal ALD process recipe

3.2.6 Sputtering

Sputtering is one of the popular physical vapour deposition techniques widely adopted for the thin film deposition of the metals and dielectrics. Sputtering deposition system comprises the plasma generated between two electrodes-cathode (target source material) and anode (sample substrate). The high energy ions in the plasma generally Ar^+, accelerate towards the cathode, the resulting bombardment of the ions with the target source results in dislodging of the source material atoms which are carried in vacuum towards the substrate. DC diode sputtering system is used for the deposition of metal, while the RF source is preferred for dielectric deposition, in order to avoid the charging effect. In addition to its ability to deposit dielectric material, RF diode system offers a higher deposition rate than DC sputtering system. Traditionally, diode sputtering system requires high voltage to achieve the required deposition rate. This could have detrimental a effect on the deposited thin films.

In this regard, magnetron sputtering is an attractive choice, as it enables to alleviate the above-mentioned issues with diode sputtering, namely low deposition rate and high voltage. This is achieved by an introduction of magnet behind target. The magnetic field confines the electron movement, thereby increasing the ionisation efficiency, resulting in an improved deposition rate at a low frequency. In addition, sputtering can also be used for the deposition of nitrides and oxides. This is achieved by introduction of gaseous mixture such as nitrogen or oxygen along with Ar to achieve the required nitride and oxide film.This is referred to as reactive sputtering.

Aluminium nitiride (AlN) is one of the popular choices as piezoelectric material, owing to its chemical and mechanical stability, further, its CMOS compatibility is another attractive feature which could be explored for pressure sensing application. A

room temperature AlN deposition process was developed via reactive RF magnetron sputtering using Al as target. The sputtering was carried out using the Plassys MP 900s Sputter tool. The sputtering recipe used for the growth of piezoelectric AlN is given in the Table 3.4. An in-depth details associated with process optimisation of AlN is discussed in the Chapter 5.

Parameters	Value
Pressure (mTorr)	5
N_2 gas flow rate (sccm)	50
Ar gas flow rate (sccm)	30
RF power (W)	500

Table 3.4: Optimised RF magnetron sputtering recipe for AlN deposition

3.2.7 Flexible Substrate Preparation and Passivation

The development of the flexible electronics is expected to bring about unprecedented changes, in which we interact with electronics and open us new avenues for novel applications. One of the fundamental requirements in the development of flexible electronics is the appropriate choice of the the substrate. In this regard, polymers have become an attractive choice as a substrate for the development of flexible electronics, owing to their mechanical flexibility, low cost and compatibility with other printing techniques such as screen printing, roll-to-roll printing process etc.

Among the polymers, polyimide (PI) has been widely adopted within the microelectronics industry as dielectric, substrates and fabrication aids etc. Besides mechanical flexibility, the high glass transition temperature ($\sim 350^{o}$C) of PI would enable the development of devices with a higher processing temperature. The spin-on PI (PI-2545 from HD MicroSystems) was used as the substrate for the development of flexible GFET based pressure sensors. The PI was spun on top of glass substrate, which acted as the carrier substrate during the device processing. The spin-on PI was spun thrice to achieve the required substrate thickness with a partial curing of the polymer after each spin process. The details of the substrate preparation are as follows:

(1) **Application of Adhesion promoter**:The adhesion promoter (VM651) diluted in RO water (1:100) is applied to the edges of glass substrate and cured at room temperature over 10 min.

(2) **Application of PI**: Spin on PI-2545 is pipetted onto the glass substrate and is spin coated in a 2 step process:

   (i) Spin at 500 rpm for 5 s with an acceleration of 100 rpm

   (ii) Spin at final speed of 2000 rpm at an accelration of 1000 rpm for 60 s

(3) **Soft bake at** 140°C **for 5 min**: The soft bake partially cures the spin-on PI. Subsequently, the process is repeated two more times to achieve the required PI thickness

(4) **Finally, the PI is baked in an oven at** 250°C **for two hours**- The remaining residual solvents are removed by a hard bake in N_2 ambient at 250°C.

Post-curing of PI substrate, room temperature inductive coupled plasma chemical vapour deposition (ICP-CVD) Si_3N_X is deposited on PI as a passivation layer. The deposition of Si_3N_X as on PI improves the interface between the PI and carrier substrate, thereby enabling the subsequent process for the device development. A low stress 100 nm thick Si_3N_X was deposited at room temperature on PI using SiH_4 and N_2 as the precursor gases. The deposition is carried out using the Oxford Instruments System 100 ICP 180 PECVD. The process parameter adopted for the room temperature deposition of Si_3N_X is provided in Table 3.5.

Parameters	Value
SiH_4 (sccm)	7
N_2 (sccm)	6
ICP Power (W)	100
Pressure(mTorr)	4
Temperature (°C)	25

Table 3.5: ICP-CVD recipe of low stress SiN_X

3.3 Characterisation Techniques

3.3.1 Raman Spectroscopy

Raman spectroscopy is one of the widely-adopted techniques for the characterisation of graphene and other nanocarbon materials. It is based on the inelastic scattering of light referred to as Raman scattering. Inelastic scattering of light process results in incident and scattered photon having a different energy. If scattering process results in loss of energy of photon due to the creation of phonon, it is referred to as Stokes process, while if the scattering results in the gain in energy of photon due to phonon absorption it is referred to as anti-Stoke process. The inelastic scattering of light occurs due to the phonons which arises due to atomic vibrations. These atomic displacements are only allowed within a given vibrational mode which is unique for a given material owing to their chemical and structural properties [165]. Therefore, Raman spectroscopy is an ideal tool for the investigation of sp^2 nanocarbon material, as each material would have its own characteristic Raman active phonons. Raman spectra of different sp^2 nanocarbon is shown in Figure 3.5. As shown in Figure 3.5, Raman spectra of all sp^2 hybridised graphitic material material comprises two characteristics peak referred to

as G-band and G'-band (also reffered to as 2D band) appearing at $1582\ \text{cm}^{-1}$ and in range of $2500 - 2800\ \text{cm}^{-1}$ respectively [165]. Besides the hybridisation nature of the carbon atom, Raman spectra can provide a wealth of information related to strain, doping, number of layers in graphene, graphene's edge structure (arm chair/zigzag), carbon nanotube's diameter and chirality [166].

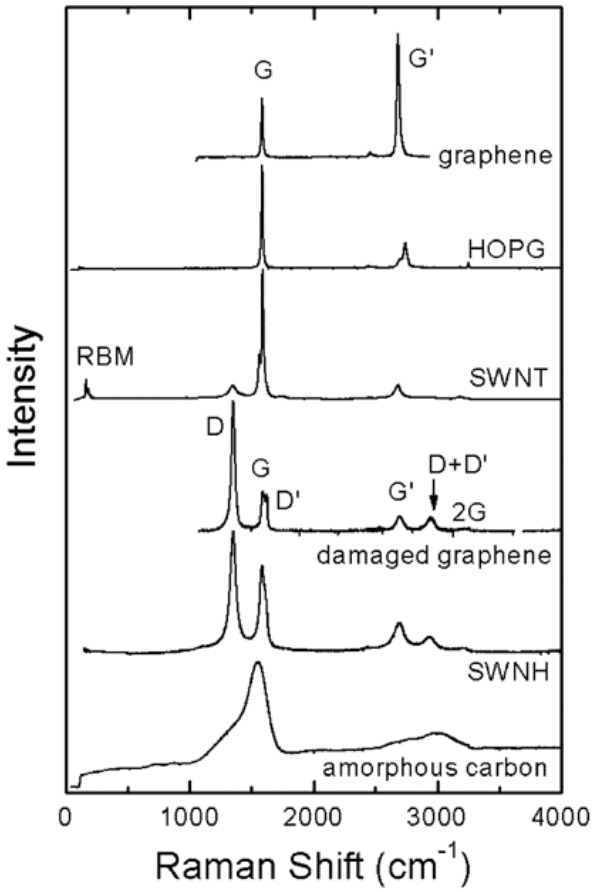

Figure 3.5: Raman spectra of different sp^2 hybridised nanocarbon. Reprinted with permission from [166] Copyright (2010) American Chemical Society

Raman spectra of Graphene

MLG consists of unique characteristics peaks in its Raman spectra. Figure 3.6 depicts the Raman spectra of wet transferred graphene. The spectra was acquired using LabRAM HR system equipped with the Ventus 532 nm laser system (100 nW)and Synapse charge coupled device(CCD) detection system with objective lens of $\times 10$, $\times 50$, $\times 100$. In exception, the data presented in Chapter 4 was acquired using LabRAM ARAMIS with 633 nm laser at Univeristy of Trento. The significance of this distinct bands are discussed in detail below [167, 168].

1. **D-Peak**- This is the peak generally observed around $\sim 1350\ \text{cm}^{-1}$ in the Raman spectra of graphene. It arises as a result of breathing modes of carbon atoms in the hexagon lattice which occurs due to a defect or a disorder in the graphene crystal lattice. D-peak originates from a second order Raman scattering process

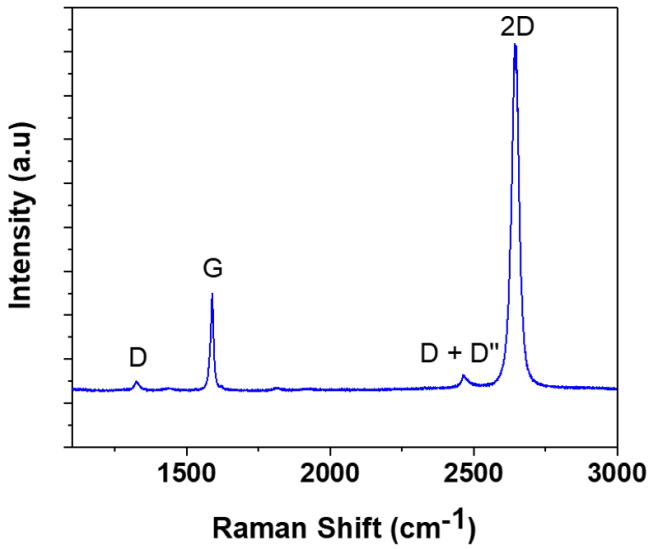

Figure 3.6: Raman spectra of wet transferred graphene acquired using 532 nm laser.

and exhibits a dispersive behaviour, i.e. the frequency of the peak is influenced by the energy of the laser. The intensity ratio between D and G peak (I_D/I_G) can be used to quantify the disorder in the graphene lattice, as the hexagonal lattice of graphene is disrupted, (I_D/I_G) ratio begins to decrease [167, 168].

2. **G-Peak**- This is one of the characteristics peak of the all sp^2 hybridised nanocarbon materials. It originates from the first order of the Raman scattering process, and is observed around $\sim$ 1580 cm^{-1} in graphene's Raman spectra. The G-peak arises from stretching of the carbon-carbon bond, therefore is a common peak in most graphitic based material. As the peak is the origin of the carbon-carbon bond, any change in bond (bond angle/length) arising from the strain will result in a corresponding change in the peak position and full-width half maximum (FWHM). Such strain in graphene arises to interaction with substrate and with other graphene layers. Therefore G-peak could be used to evaluate the strain experienced by graphene layers. Besides strain G-peak is also sensitive to Fermi-level in graphene, and therefore could also be used to study the doping of graphene [167, 168].

3. **D+D"-Peak**-This peak is observed around $\sim$ 2450 cm^{-1} in graphene's Raman spectra. It originates from the double resonance process involving two different phonons [167, 168].

4. **2D-Peak**- 2D peak is another common peak observed in all graphitic-based material. Similar to D-peak, 2D peak originates from a double resonance process of phonon with opposite momentum observed near the ***K*** branch of graphene and exhbits a dispersive behaviour. This double resonance process is very sensitive to phonon wave vector and electronic band structure. The 2D peak of the MLG exhibits a relatively higher intesity than the G peak with a single Lorentzian fit. This line shape of the 2D peak begins to evolve with a number of layers,

and therefore could be used to distinguish between MLG and few layer graphene (upto 5 layers) in an AB stacking graphene [167, 168].

3.3.2 X-Ray Diffraction

X-Ray diffraction (XRD) is a widely-adopted non-destructive technique for study on the crystalline phase of the material. It is based on the characteristic Bragg diffraction finger print of a crystalline structure. X-ray diffractometer comprises an X-Ray cathode ray tube and X-ray detector. X-ray generation occurs by bombardment of highly energetic electrons on a metal target such as Cu, Mo and Fe etc. Typically, the electrons are generated by a heated filament, the generated electrons are accelerated in a vacuum by high electric field towards the metal target. When electrons with sufficient energy displace the electrons of the metal target producing a characteristics X-ray, which is subsequently filtered and collimated and target towards the sample. The X-ray targeted towards the sample produces a constructive interference on satisfaction of Bragg's law ($n\lambda = 2dsin\theta$), which provides the relationship between the electromagnetic radiation's wavelength, diffraction angle and lattice spacing. The constructive interference results in a peak in the intensity, which is detected by the X-ray detector. The sample's crystalline phase is determined by analysing the characteristics diffraction pattern generated due to the crystal orientation of the film over a 2θ range. These characteristics peak when properly studied with reference patterns which can be used to determine the crystalline phase of the material. The piezoelectric property of AlN material is strongly dependent on its (002) crystal orientation of the sputtered film. The crystal orientation of the AlN film deposited at different sputtering condition was studied using Panalytical X'pert Pro MPD(A3-26) equipped with Bruker D8(A4-37) diffractometer with Cu target in X-Ray source ($\lambda = 0.154$ nm). The grain size of the sputtered film was determined using the Scherrer's Equation given in Equation 3.1 [169].

$$t = \frac{0.9\lambda}{Bcos\theta} \tag{3.1}$$

where t is the grain size, λ is the wavelength of X-ray source, B is the full width half maximum (FWHM) and θ is the half diffraction angle in radians of the peak.

3.3.3 GFET electrical characterisation

Current-voltage (I-V) characterisation is one of the widely-adopted techniques to study the electrical properties of graphene. Electrical characterisation of GFET- transfer and output characteristics are used to extract key information of devices, such as its Dirac point, carrier mobility, contact resistance, gate dielectric properties etc. From IV measurements, some of the aforementioned parameters were extracted using two widely-adopted techniques, namely peak transconductance and fitting method with each technique having their own pros and cons.

Peak Transconductance Method

Peak transconductance method (PTM) is a widely-adopted technique to determine the carrier mobility of the device using the field effects model. In PTM, the carrier mobility is extracted using the gate voltage dependence transconductance and carrier density, ignoring the contact resistance of the devices. As a result, the carrier mobility of the device is underestimated. However, the discrepancy between the actual and extracted carrier mobility can be improved with devices with longer channel length and low contact resistance. In PTM, the carrier mobility of the device is determined using the Equation 3.2.

$$\mu = g_m \frac{L_g}{W_g.C_g.V_{ds}} \tag{3.2}$$

where μ is carrier mobility, g_m is the peak transconductance,W is the channel width L_g is the gate length and C_g is the gate oxide capacitance and V_{ds} is the drain bias. The hole and electron carrier mobility is determined individually using the peak transconductance value.

Diffusive Transport Model

Diffusive Transport Model (DTM) is another popular method widely adopted for determining the carrier mobility in graphene. It is based on the model proposed by Kim et al [170]. The method is based on fitting the transfer curve of the GFET using the Equation 3.3. Based on the fitting model, parameters such as carrier mobility, contact resistance and the residual charge carriers are determined. Further, often due to the asymmetry in the transfer curve of the GFET, the hole and electron branch of the devices are fitted separately, to calculate the aforementioned parameters.

$$R_{total} = R_{series} + \frac{L_g}{W_g} \frac{1}{e\mu\sqrt{n_o^2 + n^2}} \tag{3.3}$$

where R_{total} is the total resistance of GFET, L_g and W_g are the channel length and width respectively, e is the electronic charge, μ is the carrier mobility, n_o is the residual carrier density, n is the carrier density modulated by top gate and R_{series} is the series combination of channel resistance under the gate and the access resistance of the device. Access resistance refers to the un-gated region of graphene between the gate and source/drain contacts. In DTM, the carrier mobility and contact resistance are assumed to be constant, when in fact both are dependent on the carrier density of the channel. The carrier density, n, is related to the top gate bias by

$$V_{tg} - V_{tg,Dirac} = \frac{ne}{C_{ox}} + \frac{\hbar v_f \pi n}{e} \tag{3.4}$$

where v_f is the Fermi Velocity and $V_{tg} - V_{tg,Dirac}$ arises from the carrier density modulated by the top gate and quantum capacitance of the graphene.

3.4 Chapter Summary

This chapter presents an overview of the different fabrication techniques adopted to for the development of GFET based pressure sensors. The fabrication process of the device was achieved using a low temperature CMOS compatible process to enable the development of flexible device and sensors. Graphene channel patterning and electrode definition was achieved using the photolithography, in order to attain a low cost high throughput process for the development of large area electronics. Post-fabrication process various characterisation techniques such as electrical measurements, Raman spectroscopy, XRD, were employed for material and device characterisation. The significant of these techniques has also been discussed in this section.

Chapter 4

Impact of Polymer Scaffold on Graphene Transfer

4.1 Introduction

The first isolation of graphene via mechanical exfoliation represented one of the major breakthroughs in material engineering in the past decade [97]. This triggered a wide interest in graphene, owing to its fascinating intrinsic material properties. Since the first isolation of graphene, a number of methodologies has been explored for the synthesis of graphene. Among them, CVD grown graphene is an attractive choice due to its capability to grow large area high quality graphene at a low cost which could satisfy industrial requirements [13,14]. Traditionally, CVD synthesis of graphene often employs transition metal on which the growth of graphene is achieved. In order to exploit the properties of graphene, requires the transfer of graphene over an insulating substrate. Therefore transfer printing of graphene is one of the critical steps in the realisation of graphene-based devices.

A wide range of techniques has been adopted for transfer of CVD grown graphene. Among them, polymer assisted transfer (PAT) of graphene is one of the widely-adopted techniques for the transfer of high quality graphene. PAT involves the use of polymer, which acts as a supporting scaffold during the etching of the transition metal.In this regard, various polymers such as poly(methyl methacrylate) (PMMA) [161,171], poly (bisphenol A carbonate) (PC) [172–174], thermal release tape (TRT) [13,175,176] have been investigated as the temporary support layer for graphene during the transfer printing process. Etching of metal is carried out using wet etchant and electrochemical de-lamination process [161,177]. PAT of graphene is an attractive choice owing to its versatility, cost-efficiency and mechanical flexibility. However, the quality of graphene is often compromised by the residual remains of the polymers and cracks formed during the transfer process, which would have a detrimental effect on the electrical and mechanical properties of graphene. A number of thermal and chemical methods have been adopted for the removal of polymeric residues. This includes high temperature vacuum annealing [178], Ar/H_2 annealing [179]. Chemical methods involves the use of

hot acetone and chloroform [161, 174]. Dry transfer of graphene (DTG) is another popular choice for the transfer of graphene, which involves the direct transfer of graphene to the target substrate (by peeling the graphene from the target substrate), while enabling the re-use of Cu for the future growth process. Transfer of graphene via DTG relies on higher adhesion strength between the graphene and target substrate, in comparison to graphene and its growth substrate. Various polymers, such as PI and UV curable PET, have been used to demonstrate the transfer of graphene via DTG [180, 181].

Hot lamination and roll-to-roll techniques have been employed for large area transfer of graphene to flexible substrate. Similar to DTG, this transfer process relies on higher adhesion strength between graphene and target substrate thereby limiting its potential to a limited substrate [182, 183]. Hot lamination and roll-to-roll techniques are often two-step transfer process: (1) Lamination of the graphene to the target substrate; (2) Removal of underlying metal by etching process. Simplicity and scalability of the transfer process makes it an attractive choice for transfer of graphene. However, high stress generated on graphene (often leading to voids and cracks) and limitations placed on the substrate limit its use in comparison to the wet transfer of graphene.

This chapter presents the study on the impact of polymers used during the transfer process on graphene.Three polymers, namely PMMA, PC and CAB, have been investigated as the polymer scaffold for the transfer of graphene. The impact of these polymers on the transferred graphene is studied by means of optical microscopy, atomic force microscopy (AFM), Raman spectroscopy and back-gate graphene field effect transistor (GFET).

4.2 Materials and Methods

Copper is one of the widely used substrates for CVD growth of graphene owing to low carbon solubility, thereby leading to predominantly a monolayer graphene. Commercially available CVD grown graphene on Cu (from Graphenea) is used in this study. During the transfer process the underlying Cu foil is etched. In this study, the Cu foil is etched in 0.5 M iron (III) chloride hexahydrate (Sigma Aldrich 236489) dissolved in RO water. The schematic describing the general PAT transfer process is shown in Figure 4.1. The transfer process of all three investigated polymers remain majorly the same with a few alterations depending on the polymer compatibility. Graphene samples are cut into small pieces and flattened with a piranha cleaned glass slides for the transfer process. During the CVD synthesis of graphene, the growth of graphene occurs at both sides of the Cu foil. Therefore in all PAT, post application and curing of the polymer, back side graphene was etched via RIE in O_2 plasma at 100 W for 20 s. The transfer process adopted for each polymer is described in the subsequent section.

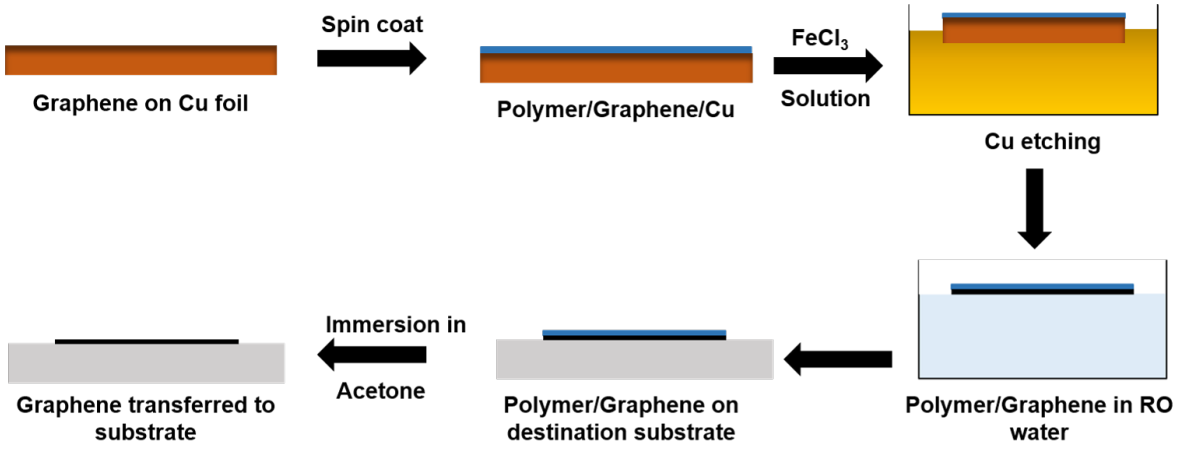

Figure 4.1: Schematic representation of major step of graphene transfer process.

4.2.1 PMMA Assisted Graphene Transfer

PMMA 495 A4 from Microchem (4% dissolved in anisole) was used as the polymer scaffold during the transfer process. The polymer was spun at 3000 rpm for 30 s and cured over 8 h at room temperature. During the transfer process the underlying Cu foil was etched effectively using iron (III) chloride hexahydrate solution. Post etching PMMA/graphene stack was rinsed in RO water for 15 min and transferred to modified RCA-2 solution as described in [161]. The modified RCA-2 solution comprised $H_2O : HCl : H_2O_2$ (20:1:1) aids in the removal of metallic residues from the prior steps of the transfer process. These metallic residues act as scattering sites for the charge carriers, would have detrimental effects on the potential devices, hence it is critical to remove such metallic residues from the transferred graphene. Following, the RCA-2 solution, PMMA/graphene stack was transferred again to RO water for 15 mins. Finally, the stack was transferred to destination substrate. The destination substrate was highly doped n-type SiO_2/Si substrate. Prior to transfer of the stack, the substrate was subjected to O_2 plasma treatment at 100 W for 35 s using Oxygen Barrel Asher - PlasmaFab 505, to increase the hydrophilicity of the substrate. Following, the transfer of graphene a two-step baking process was carried out. The stack on the substrate was baked at 55°C for 5 mins and gradually the temperature was raised to 150°C. The baking step assisted in the removal of the trapped water between the graphene and the substrate and improved the contact between graphene and substrate. The substrate was further annealed at 150°C for 1 h in vacuum. Finally, the PMMA was removed by overnight immersion in acetone. The sample was then immersed in the isopropanoal (IPA) and blow-dried using N_2 gas.

4.2.2 PC Assisted Graphene Transfer

Polycarbonate is another polymer which has been investigated as an alternative to PMMA for transfer of graphene. PC is an attractive alternative, owing to ease of removal using organic solvent without the need of high temperature annealing.

A 2 w.t% by volume of poly(bisphenol A carbonate(Sigma Aldrich 181625)solution was prepared by dissolving the PC pellets directly in chloroform. PC was spun on graphene/Cu substrate at 4000 rpm for 30 s and cured at overnight at room temperature. Post etching of Cu substrate, similar steps related to PMMA assisted transfer were adopted to transfer of graphene. PC scaffold was then dissolved by 8 h immersion in the chloroform. The substrate was degressed in methanol, IPA and blow-dried using the N_2 air gun.

4.2.3 CAB Assisted Graphene Transfer

CAB is a cellulose-based polymer used for transfer printing of graphene. A 2 w.t% by volume of CAB (purchased from Sigma Aldrich 180963) dissolved in the ethyl-l-lactate was used as support polymer. A similar step to that outline above was adopted to achieve CAB assisted transfer of graphene. Post transfer of graphene, the substrate was baked at 55°C for 5 mins and then annealed at 80°C for 1h in N_2 ambient oven. CAB was removed by adopting the similar steps described in PMMA assisted graphene transfer.

4.3 Results and Discussions

4.3.1 Optical Microscopy and AFM Analysis

PAT of CVD graphene often results on unavoidable wrinkles, residues and cracks which will have a detrimental effect on the transferred graphene. Therefore the presence of them is a good indication to evaluate the quality of transferred graphene. The optical micrograph of the graphene transferred with different polymers is shown in Figure 4.2. PMMA and CAB assisted transfer led to graphene transfer with a continuous film with less noticeable residues. Figure 4.2b shows PC transferred graphene, the transferred graphene was not continuous and consists of the noticeable residues on the graphene surface. AFM scan of surface of graphene transferred with different polymer is shown in Figure 4.3. Among the transferred graphene sample PC transferred sample exhibited the highest roughness of 1.54 nm indicating the presence of higher residues. PMMA and CAB samples exhibited a similar surface roughness if 1.28 nm and 1.29 nm respectively.

4.3.2 Raman Spectroscopy

Raman spectroscopy is a powerful non-invasive tool widely adopted for the characterisation of graphene, which provides vital information such as its crystalline quality, strain,doping and edges etc. In this regard, Raman spectra of graphene is an ideal tool to evaluate the impact of of polymer scaffold on the transferred graphene. Raman frequencies of graphene G(ω_G) and 2D (ω_{2D})are sensitive to both strain and doping of the transferred sample. The sensitivity to strain results from the change in

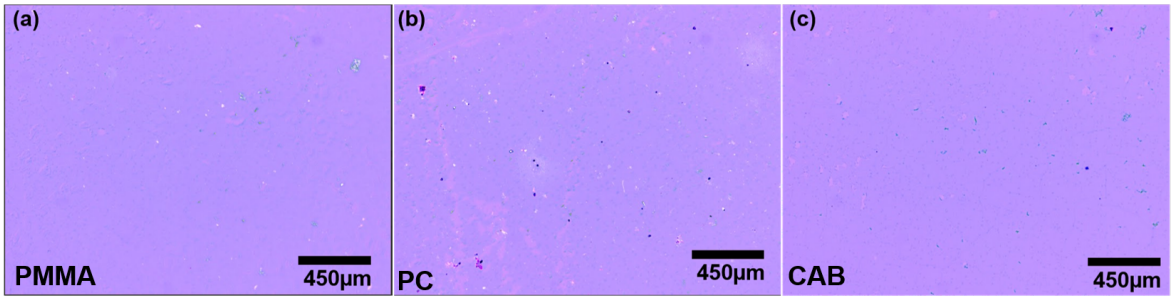

Figure 4.2: Optical microscopy image of graphene surface transferred using different polymer scaffold (a) PMMA (b) PC (c) CAB.

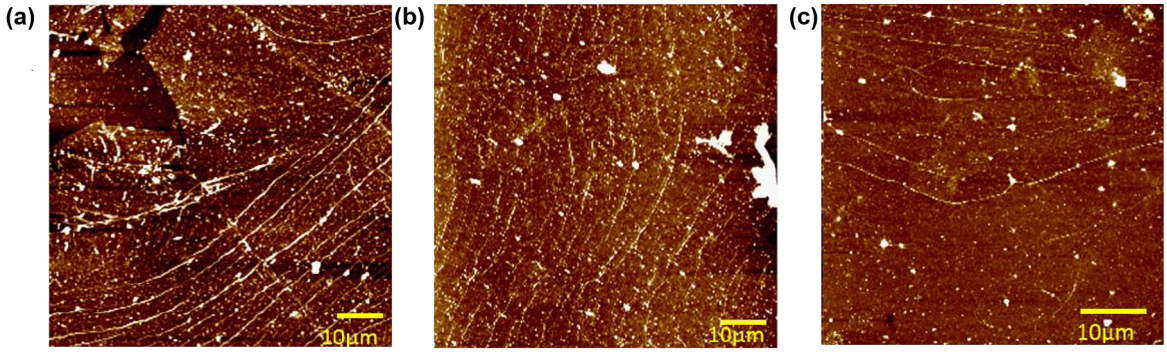

Figure 4.3: AFM scan of 10 μm$\times$ 10 μm of graphene transferred using (a) PMMA (b) PC (c) CAB. The average surface roughness of the film were 1.28 nm, 1.54 nm and 1.29 nm respectively.

the lattice constant of transferred film, resulting in a change in the Raman frequency of phonon [184] while the doping results in alteration of bond length due to static effect and electron-phonon coupling, resulting in the shift in the frequencies of the ω_G and ω_{2D} [185]. Since G and 2D peak are affected by both strain and doping, asserting the independent influence of strain and doping on ω_G and ω_{2D} becomes more complex. Therefore, individual contribution of strain and doping on the Raman spectra, was decoupled using the modified model proposed on [185].

The representative Raman spectra of graphene transferred via different polymer scaffolds and Lorentzian fittings of G and 2D peaks are shown in Figure 4.4. The presence of two prominent peaks- G (1586 cm^{-1}) and 2D (2648 cm^{-1}) and sharpness of 2D peak typifies MLG [186]. Further,the absence of significant D peak (1330 cm^{-1})and high intensity ratio of 2D and G peak (I_{2D}/I_G>2) are an indicative feature of a high quality transfer of graphene. The statistical variation in the Raman data of graphene transferred via different polymer scaffold is shown in Figure 4.5. Table 4.1 summaries the statistical data of different graphene samples transferred using three polymers- PMMA, PC, CAB.

Raman vector model

The G and 2D peaks are affected by both strain and doping, thereby resulting in change of peak position, FWHM and intensity, respectively. Increasing electron and

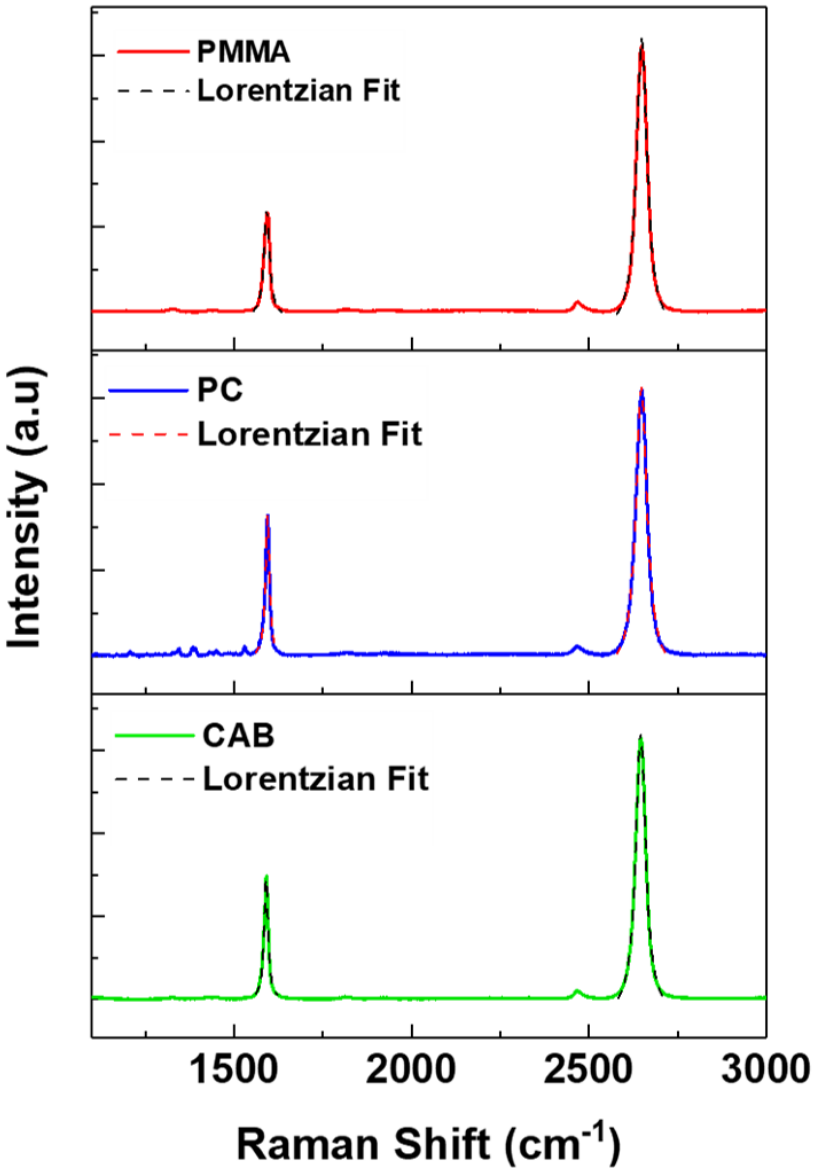

Figure 4.4: Representative Raman spectra of graphene transferred via different polymer scaffolds- PMMA (Red), PC (Blue) and CAB (Green) using 633 nm laser. Lorentzian fitting of G and 2D peaks of transferred graphene samples are shown.

Polymer	Pos(D)(cm^{-1})	FWHM(D)(cm^{-1})	Pos(G)(cm^{-1})	FWHM(G)(cm^{-1})	Pos(2D)(cm^{-1})	FWHM(2D)(cm^{-1})	I_{2D}/I_G	I_D/I_G
PMMA	1325.99 ± 1.95	25.93 ± 5.24	1587.87 ± 1.69	14.31 ± 2.31	2644.63 ± 3.15	33.94 ± 4.08	2.63 ± 0.59	0.083 ± 0.05
PC	1332.24 ± 4.56	42.67 ± 43.04	1589.56 ± 1.81	15.35 ± 1.53	2646.09 ± 1.23	35.15 ± 2.06	2.40 ± 0.30	0.058 ± 0.021
CAB	1326.92 ± 2.45	32.30 ± 14.14	1589.56 ± 1.88	13.89 ± 1.63	2645.39 ± 1.22	31.88 ± 1.69	2.44 ± 0.22	0.085 ± 0.064

Table 4.1: Statistical data of Raman mapping of different PAT graphene via Lorentzian fitting

hole concentration results in up-shift of G-peak, while the FWHM of G-peak decreases for a similar trend. 2D peak is influenced by the carrier type, increasing electron (hole) concentration results in down-shift (up-shift) of 2D peak [186]. Similarly, increasing tensile strain on CVD graphene results in the up-shift of both G and 2D peaks. Such observed trends make it difficult to quantify the individual contributions on the Raman spectra. The individual contribution of strain and doping can be determined by considering the fractional variation in the $\Delta\omega_G/\Delta\omega_{2D}$ in the $\omega_G - \omega_{2D}$ space arising due to either strain and doping. Therefore a modified Raman vector model proposed

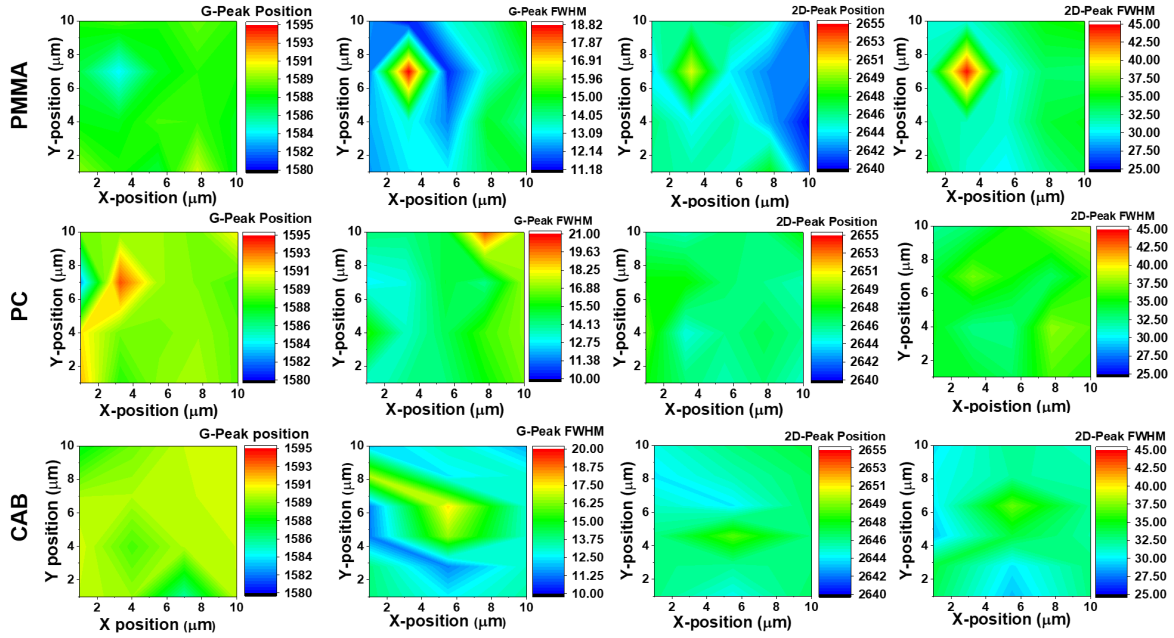

Figure 4.5: Representative 10 point Raman spectra maps of graphene transferred via different polymer scaffolds- PMMA (Red), PC (Blue) and CAB (Green). Lorentzian fitting of G and 2D peaks of transferred graphene samples are shown.

in [185] is used to determine the strain and doping contribution by analysing Raman Data in $\omega_G - \omega_{2D}$ space. The proposed Raman vector model is achieved by considering the three parameters:

(i) **Origin Point:** Origin points $(\Delta\omega_G^0, \Delta\omega_{2D}^0)$ refers to intrinsic Raman frequency of unstrained and un-doped graphene. Raman spectra of suspended graphene is considered to unaffected from strain or excess charge carriers and substrate induced doping, therefore the Raman data from [185] is adopted for $\Delta\omega_G^0$ ($\sim 1583.06 \pm 0.6$ cm^{-1}) while for the $\Delta\omega_{2D}^0$ ($\sim 2639.5 \pm 1.2$ cm^{-1})the data from [187] is used owing to similar laser energy. The charge density, n_0, of the suspended graphene is estimated to be a 2×10^{11} cm^{-2} [185].

(ii) **Fractional variation due to strain $((\Delta\omega_{2D}/\Delta\omega_G)\varepsilon)$ and doping $((\Delta\omega_{2D}/\Delta\omega_G)n)$:** The ω_{2D} and ω_G are highly influenced by strain and doping, as mentioned above, however, the fractional variation due to strain, $(\Delta\omega_{2D}/\Delta\omega_G)\varepsilon$ is significantly different to the frctional variation caused due to doping $(\Delta\omega_{2D}/\Delta\omega_G)n$. The fractional variation due of $(\Delta\omega_{2D}/\Delta\omega_G)\varepsilon = 2.2 \pm 0.2$ and $\Delta\omega_{2D}/\Delta\omega_G)n = 0.70 \pm 0.05$ proposed in [185] was used in this work.

(iii) **Strain and doping sensitivity:** The strain influence on graphene was determined using the proposed experimental values in [184]. This was achieved by considering the strain dependent G-peak position. The strain dependent G-peak behaviour for exfoliated and CVD graphene differ significantly, owing to polycrystalline nature of CVD graphene. In this study, experimentally determined strain induced G-peak shift of CVD graphene $(\delta\omega_G/\delta\epsilon)$ of 41.1 cm^{-1} was used as

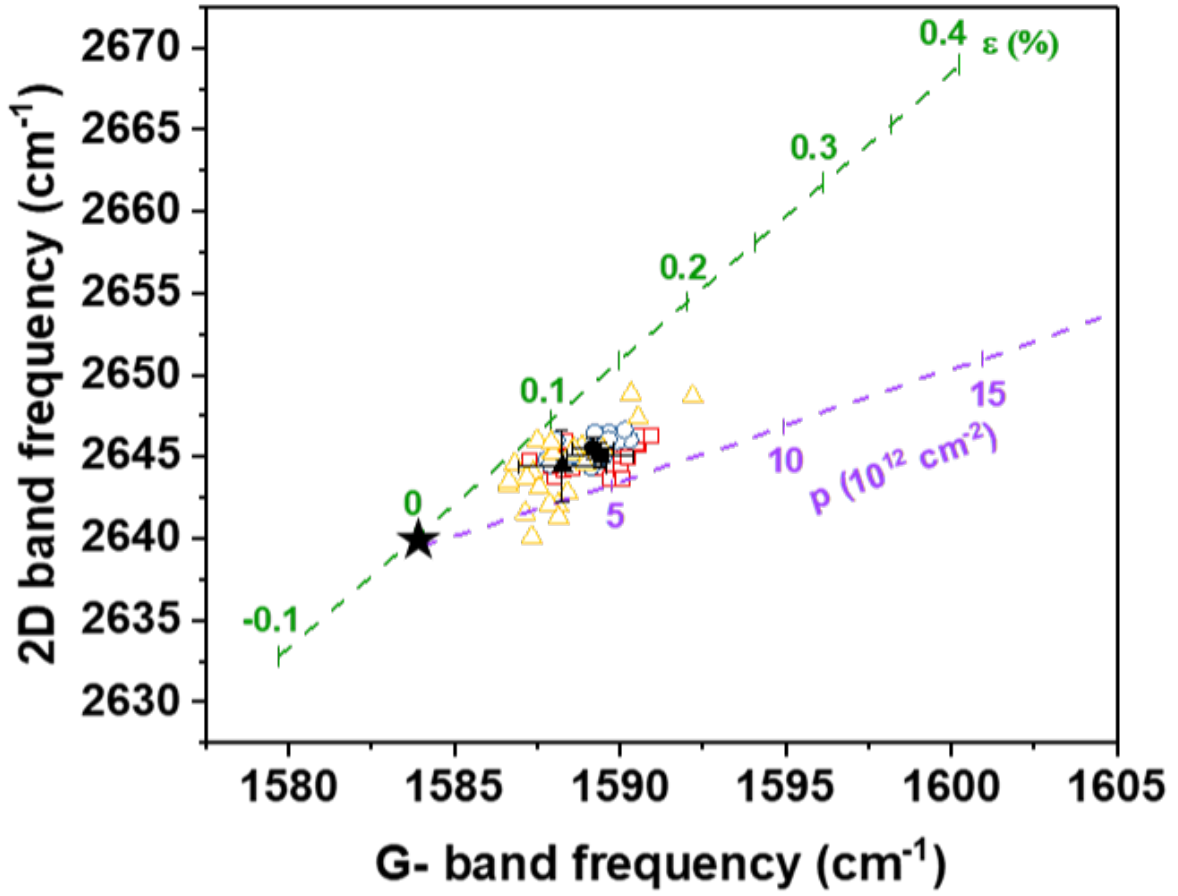

Figure 4.6: The G and 2D peak position distribution for graphene, transferred with different polymer scaffolds. The green line (dashed) shows the experimental trajectory of G and 2D position for as function of strain for a CVD graphene extracted from Bissett et al [184]. The purple line (dashed) represents the variation in the G and 2D peak distribution as a function of the doping determined using the data from Das et al [186]. The origin point of $\omega_G - \omega_{2D}$ is indicated by the star. The distribution of the G-2D peak position of graphene transferred for different polymers- CAB (red square), PC (blue circle), PMMA (yellow triangle) is shown. The strain and doping contribution was decoupled using the Raman vector model. The black symbols represent the average and standard deviation in the distribution of G ans 2D peak for different polymers- CAB (black square), PC (black circle) and PMMA (black triangle).

the strain sensitivity graphene was determined using the proposed experimental values in [184]. The influence of doping on Raman spectra of graphene was determined by observing the evolution of 2D-peak's positions. The was achieved using the theoretical and experimental values reported by Das et al [186].

Subsequently, by considering the above parameters, the individual influence of strain and doping on the Raman spectra can be extracted. The impact of the polymers on the doping and strain on the transferred graphene is determined by analysing the $\omega_G - \omega_{2D}$. The distribution of the G and 2D peak frequencies due to variation in strain and doping for different polymers is shown in Figure 4.6. All polymers exhibited a strain on the transferred graphene, among them CAB exhibited the least strain ($\epsilon \approx 0.045$ %) with PC and PMMA transferred graphene exhibiting a strain of 0.051 % and 0.050 % respectively. In addition, graphene transferred via CAB exhibited the lowest doping of

14.26×10^{11} cm^{-2}, while PC has the highest doping of 16.01×10^{11} cm^{-2} with PMMA transferred graphene showing a doping level $\approx 15.5 \times 10^{11}$ cm^{-2}. Further, the up-shift of 2D-peak position with respect to intrinsic graphene position indicates hole doping in all transfer polymer scaffold cases.

4.3.3 Electrical Characterisation

The impact of the polymer scaffold on the electrical transport of graphene was investigated by analysing the electrical performance of back-gated GFET. The polymeric residues of the scaffold on graphene act as a charge scattering point and dopants affecting its electrical property. Post PAT of graphene to SiO_2/Si substrate, graphene was patterned via RIE etching in O_2 plasma defining graphene channels of width 1 mm. The source and drain electrodes (20 nm / 100 nm Ti/Au) of graphene were deposited via e-beam evaporation using the metal shadow mask (from Ossila)resulting in 16 devices with a varying channel length of 15 μm to 60 μm. Figure 4.7 depicts the schematic representation and optical microscopy image of GFET. The electrical characterisation of the GFET was carried out in ambient conditions and was used to determine the average carrier mobility of graphene, charge neutrality point (CNP) also referred to as Dirac point and device to device variation.

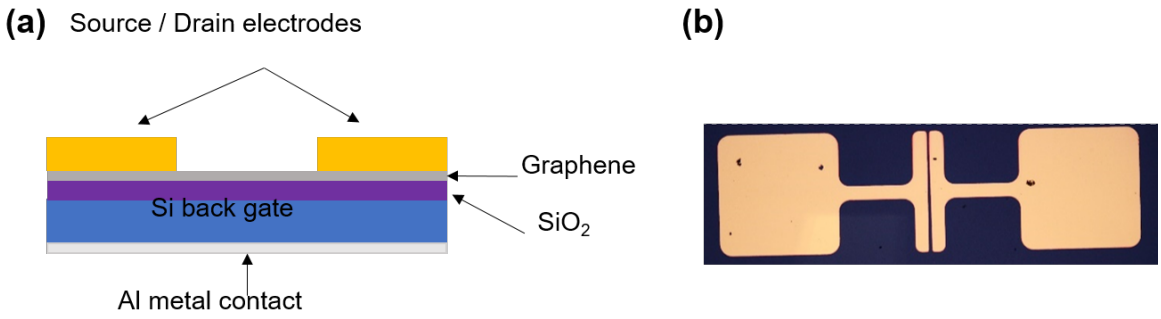

Figure 4.7: (a)Schematic representation of back gate GFET structure (b) Optical microscopy image of GFET

The fabricated GFET devices exhibited the typical ambipolar behaviour, where the electrical transport occurs due to both holes and electrons. The typical transfer and output characteristics of GFET are shown in Figure 4.8. Figure 4.9 (a)-(c) shows the variation in carrier mobility and Dirac points of GFET with graphene transferred with different polymer scaffolds. Further, devices were not subjected to additional high temperature annealing treatment typically employed to remove the polymeric residues and volatile dopants such as water. This step was avoided in order to evade any thermal budget restriction that could affect the development of flexible electronic devices. CAB ($\mu_{\text{hole}} = 1586$ cm^2/V.s & $\mu_{\text{electron}} = 1698$ cm^2/V.s) and PMMA ($\mu_{\text{hole}} = 1536$ cm^2/V.s & $\mu_{\text{electron}} = 1531$ cm^2/V.s) transferred graphene devices exhibited a higher carrier mobility in comparison to PC transferred graphene devices ($\mu_{\text{hole}} = 340.07$ cm^2/V.s & $\mu_{\text{electron}} = 374.07$ cm^2/V.s). This observed trend can be described by extracted

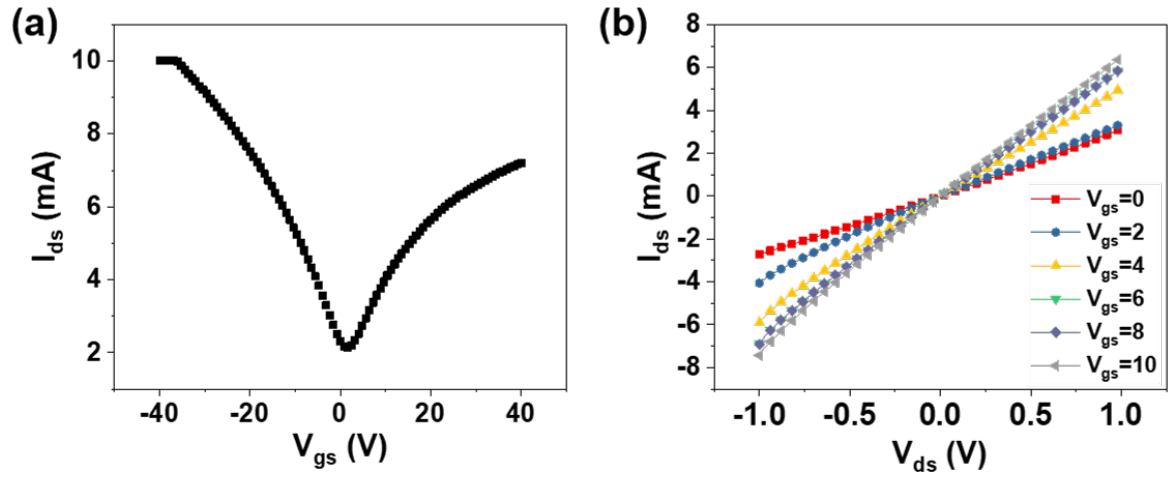

Figure 4.8: Electrical characteristics of GFET.(a)Typical ambipolar transfer characteristics of GFET at V_{ds}=1 V. (b)Output Characteristics of GFET for varying back gate voltage

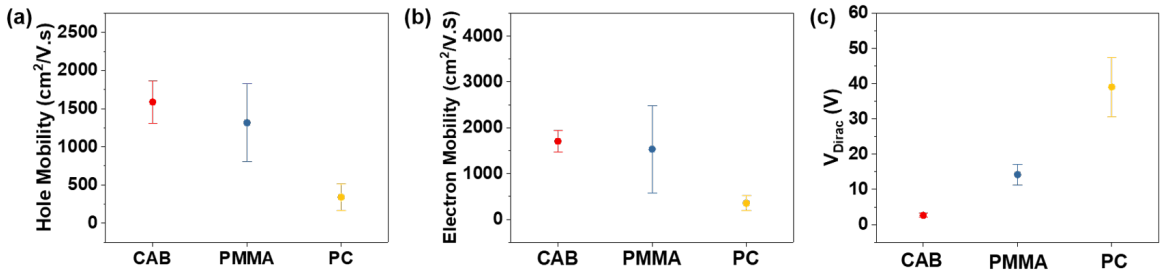

Figure 4.9: Variation in (a)hole mobility (b)electron Mobility (c)Dirac point of GFET with graphene transferred using different polymer scaffold CAB, PMMA and PC. The presented data is an average of 10 devices for each transferred case.

residual carrier density of devices for each transferred case. Table 4.2 shows the average residual charge density for different polymer scaffolds. As observed from Table 4.2, PC transferred graphene samples exhibited approximately 5.7 times more residual charge density in comparison to CAB transferred graphene devices. Higher residual charge density results in higher charge scattering points, leading to observed degradation in the carrier mobility in PC transferred samples. This is further evident by higher Dirac point voltage for PC transferred GFET samples, as shown in Figure 4.9c confirming the higher doping effect of PC scaffold. Further, this result is in good agreement with the Raman data where PC transferred graphene exhibited a higher doping levels. It must also be noted the graphene's Raman data was extracted from graphene regions not in contact with metal electrodes. The observed variation in the charge density between electrical characterisation and Raman data could be attributed to the aforementioned reason. Besides, higher carrier mobility and lower doping effects, CAB transferred devices exhibited lower device to device variability as depicted in Figure 4.10. This further confirms that CAB based PAT of graphene results in a uniform large area transfer. Further, the lower CNP also confirms that CAB can be more efficiently removed in the comparison to other polymers.

Polymer Scaffold	Residual density (n_0) (cm^{-2})
CAB	$6.14 \times 10^{11} \pm 2.56 \times 10^{11}$
PMMA	$1.08 \times 10^{12} \pm 4.45 \times 10^{11}$
PC	$3.51 \times 10^{12} \pm 2.18 \times 10^{11}$

Table 4.2: Extracted average residual carrier density of GFETs with graphene transferred via different polymer scaffolds

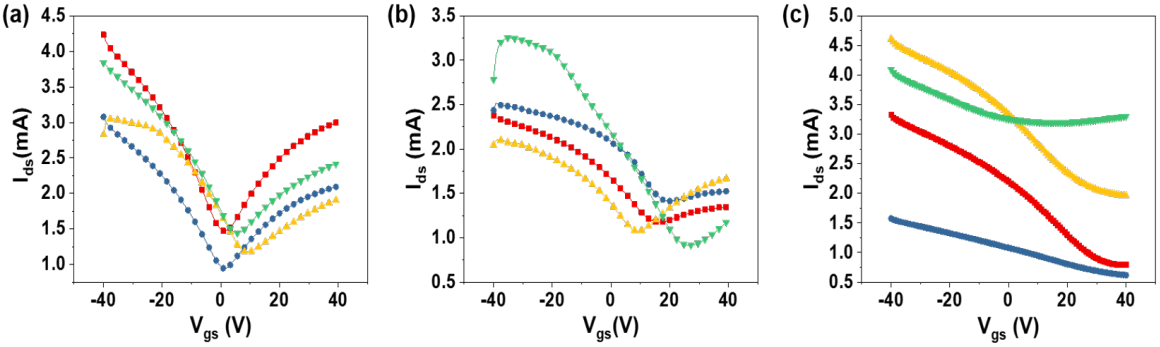

Figure 4.10: Device to Device variation of GFET devices of similar channel length for different transfer polymer scaffold (a) CAB (b) PMMA (c) PC at $V_{ds} = 300$ mV.

4.4 Chapter Summary

PAT of graphene is one of the widely-adopted techniques for transfer of large area CVD graphene. Transfer printing is one of the critical steps in the realisation of CVD based graphene devices as the quality of graphene is often compromised during the transfer process due to cracks, wrinkles and polymeric residues. This chapter investigates three different polymers, namely CAB, PMMA and PC as a supporting polymer for the transfer of graphene using the anneal-free process. Post transfer of graphene to the destination substrate, the polymers were removed by immersion in an appropriate solution. PMMA and CAB were removed using acetone, while PC was removed using chloroform.

A comparative study between graphene transferred with different polymer scaffold demonstrated CAB assisted transfer yielded a higher quality transfer of graphene. Though CAB and PMMA transferred graphene exhibited a similar average carrier mobility, the lower CNP and device to device variation in CAB transferred devices makes it an attractive polymer for graphene transfer. Among the three polymers PC device exhibited lower carrier mobility and higher doping effects. The electrical characterisation is also supported by the Raman spectrum data of graphene transferred for different polymer scaffolds, where PC transferred graphene exhibited a higher doping. Additionally, CAB transferred graphene also exhibits a lower strain, as is evident from the Raman vector model. The CVD growth process results in a compressive strain on graphene, which is partially released by thermal expansion folds. During the process, this strain is partially released due to the plasticity nature of the polymer. CAB due to its higher plasticity nature than PMMA and PC, is able to release the strain leading to smaller folds and lower strain, with PC exhibiting the

highest strain. Therefore, owing to lower strain and superior electrical performance, CAB is determined to be the appropriate polymer for the transfer of graphene, hence in all the subsequent studies in the upcoming chapters, the graphene transfer printing was achieved using CAB as the polymer scaffold.

Chapter 5

Dielectric Characterisation

5.1 Introduction

Graphene is a promising material for various emerging applications in the post-silicon era, owing to its intrinsic material properties where the zero band-gap nature of graphene is not a limiting factor. For applications such as RF transistors and flexible electronics it is critical to to achieve a high quality graphene-dielectric interface. The deposited dielectrics are widely used as for electrostatic gate dielectric and for electric spin injections [188]. Such applications require growth of a high quality thin gate dielectric layer. Various techniques, such as physical vapour deposition (PVD) and ALD, have been explored for the deposition of high-k on graphene. PVD techniques such as sputtering and pulse laser deposition leads to undesirable structural damage of graphene, resulting in degradation of its electronic properties eventually resulting in a low performance device [189,190]. On the other hand, ALD is an attractive alternative to PVD techniques and enables the the growth of uniform coverage high-k dielectric on graphene. Especially, thermal ALD process is favoured over plasma-enhanced ALD (PEALD) process, owing to the existence of energetic or reactive species in the latter causing structural damage to the graphene lattice [191]. In spite of its advantages over other PVD processes, the ALD growth on pristine graphene is a challenge, owing to lack of dangling bonds in graphene required for the ALD growth. The nucleation sites for the ALD growth on graphene can be achieved by : ultrathin oxidised metallic layer [170]; use of organic polymer buffer layer [192]; functionalisation of graphene [193] Besides the above mentioned factors, ALD growth is also affected by: graphene synthesis and transfer technique; underlying substrate; precursor chemistry; growth temperature. For instance, ALD growth on CVD graphene is much easier in comparison to HOPG. This observed behaviour is attributed to higher probability of finding defect or wrinkle in the transferred CVD graphene in comparison to HOPG. The presence of wrinkles or defects acts a nucleation site, thus promoting the ALD growth. The polymeric residues from the transfer scaffold in CVD graphene can either prompt or inhibit the ALD initiation based on the ALD precursor chemistry. In addition, based on the precursor the reactivity with graphene edges, wrinkles and defects vary. For instance

TMA is less reactive with graphene grain boundary in comparison with $MeCpPtMe_3$ (Pt precursor) [188].The deposition temperature is a crucial factor, especially where H_2O is used as the precursors, where low deposition temperature leads to a more uniform coverage of film. Despite its advantage of uniform film, the low temperature deposition has a negative impact on the deposited film, such as low dielectric constant. Further, with lower temperature ($< 100^oC$) precursors such as H_2O are difficult to remove and would require additional purging time to successfully remove the residual H_2O precursors to prevent any unnecessary reaction from the subsequent ALD cycles. Therefore it is critical to chose the optimal conditions for the ALD window for a successful growth of uniform film.

The dielectric deposition by PVD process like sputtering causes structural damage to graphene. This has limited its use in development of flexible electronics. Nonetheless, its low temperature deposition process is attractive feature. In this regards, AlN is investigated as a piezoelectric layer for a GFET based pressure sensor. To prevent any structural damage to graphene, AlN is sputtered on top of a ALD Al_2O_3 and forms a top gate dielectric stack of the flexible GFET.

This chapter presents an investigation of dielectric and dielectric stack used in the development of top-gate GFET and flexible pressure sensor respectively. The first section of the chapter focuses on the investigation of the thermal ALD growth of the Al_2O_3 as top gate dielectric, while the second section of the chapter focuses on the deposition and optimisation of the AlN layer deposited via RF sputtering as a piezoelectric transducer layer for the pressure sensing application. The process development of the piezoelectric AlN layer was carried out in collaboration with another PhD student-Shoubhik Gupta.

5.2 Thermal ALD growth

5.2.1 Materials and Methods

A CVD grown MLG on Cu (from grpahenea) was used in this study. The graphene was transferred to a highly doped n-type Si substrate using the method described in Chapter 3. Post transfer, 3 nm of Al was deposited on top of graphene at slow rate (0.05 nm/s) in an O_2 ambient (3 sccm) using Plassys MEB 550s e-beam evaporator. This deposited Al film serves as the nucleation layer for the subsequent ALD process. Al_2O_3 was deposited via thermal ALD process using Oxford Instruments FlexAL Atomic Layer Deposition. Al_2O_3 growth was achieved using a thermal ALD process instead of plasma ALD to evade the plasma induced damagae to graphene. ALD of Al_2O_3 was carried out at 200^oC using TMA and H_2O as the precursors with a deposition rate of 0.1 nm/cycle. The intricate details of ALD of Al_2O_3 growth conditions are given in Table 3.3.

The impact of nucleation layer on ALD growth of Al_2O_3 and the surface morphology

of the deposited film was investigated using AFM. In addition, the dielectric property of the Al_2O_3 was investigated via development of metal-insulator-semiconductor (MIS) and metal-insulator-metal (MIM) structure. The top electrodes (Ti/Au-10/50) of both MIS and MIM structures were defined by photolithography, metallisation and lift-off using the photolithography process for top-gate electrode deposition process described in Table 3.2.

5.2.2 Results and Discussion

Surface Morphology Study

The absence of any surface groups, or out of plane bonds on graphene makes it harder to initiate ALD growth on graphene. In this work, a thin layer of oxidised 3 nm of Al layer was employed as the nucleation layer for the growth of ALD Al_2O_3. To evaluate the surface coverage and roughness of the Al_2O_3 deposited via thermal ALD process, ALD was performed on a reference Si substrate. The Si substrate was degreased by sonication in acetone, IPA and RO water and dried with N_2 gas. Subsequently, substrate was treated with HF to remove the native oxide and immediately loaded into the ALD chamber. The film thickness, its deposition and uniform coverage was confirmed by J.A.Woollam. Co M2000XI spectroscopic ellipsometer at JWNC. Figure 5.1 depicts the AFM image of 2 μm$\times$ 2 μm area of Al_2O_3 deposited on Si substrate. The deposited film exhibited an average roughness (R_a) of the 0.67nm.

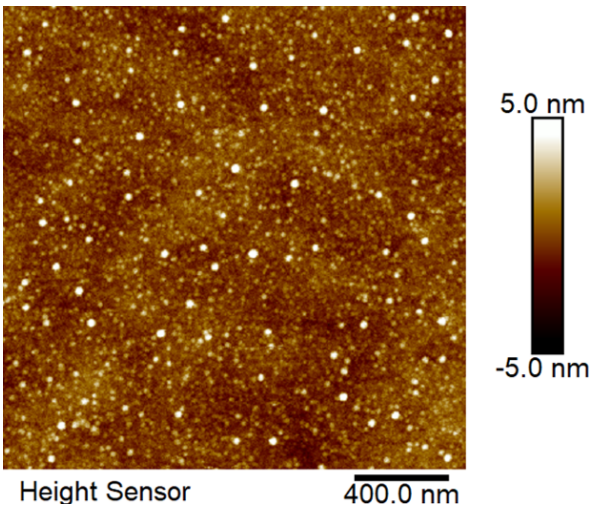

Figure 5.1: AFM scan of surface morphology of ALD Al_2O_3 on reference Si substrate exhibiting an average roughness of 0.67 nm.

The impact of nucleation layer on the Al_2O_3 deposition on graphene is investigated by performing an ALD deposition on graphene samples with and without the Al nucleation layer. Figure 5.2 shows the AFM images of surface morphology of graphene, Al_2O_3 directly deposited on graphene and Al_2O_3 deposited on graphene with thin Al nucleation layer. Figure 5.2a shows the surface morphology of graphene transferred onto SiO_2/Si substrate with an average roughness, R_a, of 1.09 nm. The graphene

comprises wrinkles and residues, which are inevitable in the transfer process. The presence of wrinkles, defects and residues can act as preferential sites for the ALD growth. The direct ALD growth of Al_2O_3 on graphene resulted in the formation of clusters of Al_2O_3 as depicted in Figure 5.2b. This is attributed to the hydrophobic nature of graphene, thus resulting in film with pinholes and an average roughness of 1.84 nm. This issue could be alleviated by the use of a thin Al seed layer, thus promoting a conformal coverage of Al_2O_3 film. Figure 5.2c shows an AFM scan of 2 μm$\times$ 2 μm area of Al_2O_3 deposited on graphene with Al layer. The presence of a thin Al layer promotes a conformal coverage of graphene. Post deposition of Al_2O_3 the wrinkles on graphene surface becomes unnoticeable with surface roughness of the film reducing to 0.79 nm, thus confirming the uniform ALD deposition.

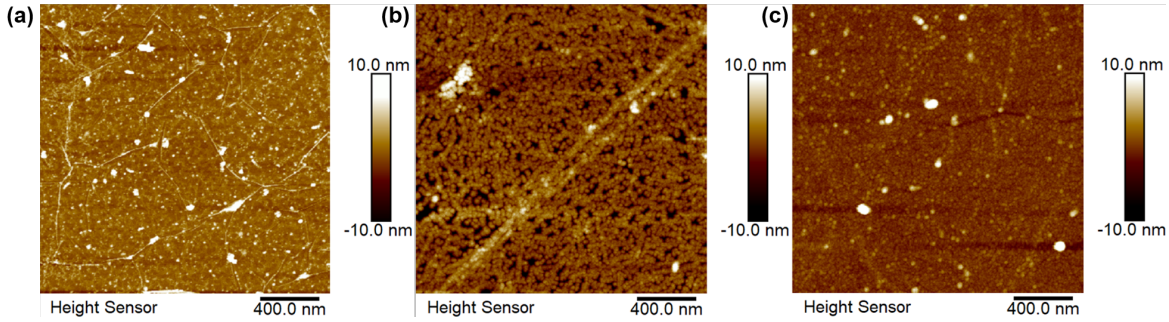

Figure 5.2: AFM image of surface morphology of (a) graphene (b)Al_2O_3 on graphene (c)Al_2O_3 on graphene with a Al nucleation layer.

Electrical Characterisation of Dielectric

The ALD Al_2O_3 serves as the top-gate dielectric for GFET. Therefore it is critical to ensure the deposition of high-quality gate dielectric. The electrical property of the dielectric was investigated via capacitance voltage (C-V) measurement of MIM structure. The MIM strucutre comprises of 100nm thick Al as the bottom electrode with Al_2O_3 and top electrode of Ti/Au. The C-V characteristics of the dielectric at different frequency is shown in Figure 5.3. As shown in Figure 5.3, the capacitance density of the MIM structure decreases with the increasing frequency. This is attributed to the change in the dielectric constant of the film with the increasing frequency. The dielectric constant of the film is strongly influenced by the polarisation of charges within the film. At high frequency the polarisation of charges are not able to follow voltage variation thereby leading to the observed change in the capacitance with the frequency. The dielectric constant (ϵ_r) of the ALD film was 7.46 calculated using $\epsilon_r = (C_{ox} \times t_{ox})/\epsilon_0$, where C_{ox} is the gate oxide capacitance per unit area, t_{ox} (30 nm) is the gate dielectric thickness, ϵ_0 is the permittivity of free space.

To further, evaluate the electrical characteristics of dielectric, I-V measurements were performed on the Au/Al_2O_3/graphene/Si substrate. Th I-V characteristics of the device is shown in Figure 5.4. The 30nm Al_2O_3 film exhibited a breakdown voltage of 6 MV/cm. The film exhibited a leakage current density of 52 nA/cm^2 at 1.6 MV/cm.

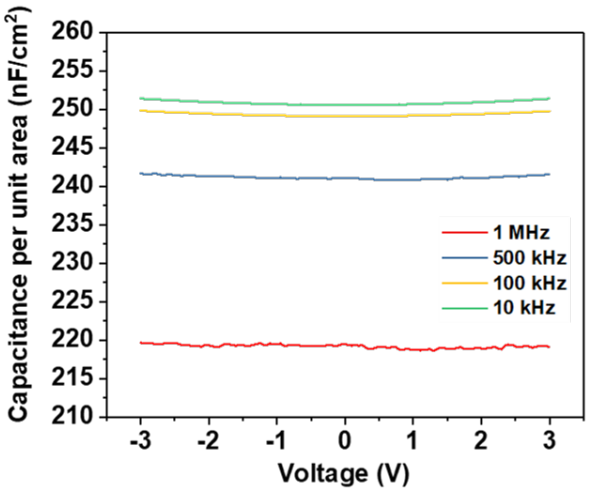

Figure 5.3: C-V characteristics of Al_2O_3 MIM structure at different frequencies of 10 kHz, 100 kHz, 500 kHz, 1 MHz

The leakage current observed is attributed to the electrons tunnelling from the interface traps to the oxygen vacancies observed at the graphene dielectric interface. The low leakage current and dielectric constant of 7.46 confirms the ALD resulted in deposition of high quality gate dielectric.

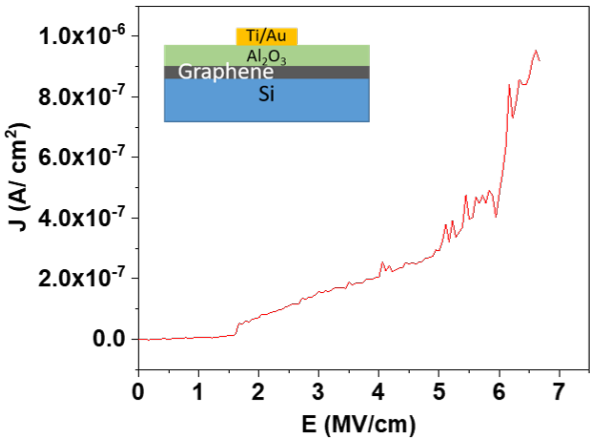

Figure 5.4: Leakage current of MIS structure with 30nm thick ALD Al_2O_3. The insert shows the scheme of the cross-section of the device on which the I-V characterisation was carried out.

5.3 Piezoelectric Aluminium Nitride

Aluminium nitride (AlN) is III-V nitride with closely packed wurtzite structure which has become a significant interest in recent times, owing to its unique properties such as high thermal conductivity, high thermal stability, its piezoelectric properties and wide-band gap [194, 195]. PZT and AlN are a popular piezo-material widely used as a transducer layer for micro-electro-mechnical-system (MEMS) and actuators application [196]. However, the ability to deposit AlN at low temperature, its CMOS compatibility, high dielectric strength makes it a distinct candidate among

the two aforementioned materials. AlN is also non-ferroelectric material, therefore it does not require any additional pre-processing steps, such as high voltage pooling or stretching often employed in piezoelectric material such as PZT, poly-vinylidene fluoride (PVDF) and poly-vinylidene fluoride trifluoroethylene [P(VDF-TrFE)] to enhance its piezoelectric property [38, 58]. The piezoelectric property of AlN is strongly influenced by its crystal orientation, with the highest piezoelectric property reported for film with excellent c-axis orientation (0002). Such c-axis orientation has been often achieved by adopting a high temperature process, which would limit its use in CMOS process and flexible electronics application due to thermal budget restrictions. Among the investigated deposition techniques, sputtering is an attractive choice due to its low temperature, inexpensive, large area process compatibility. Besides deposition temperature, substrate is another key parameter which influences the crystal orientation of the deposited AlN film. In general, c-axis oriented AlN film has been achieved by depositing on a rigid substrate such Si. However with the recent development of flexible electronics,polymers have been investigated as an alternate substrate for depsoition of AlN film. Various polymers such as polyimide (PI), polyethylene terephthalate (PET) have been investigated as substrate.Frequently, the deposition is carried out on metal/polymer stack with deposited AlN film exhibiting an enhanced piezoelectric coefficient [197].

This section discusses the process optimisation for highly oriented c-axis AlN film deposited via room temperature RF sputtering process. Various process parameters such as pressure, RF power, gas composition were varied and their impact on the crystal orientation of the film was studied. The optimisation of the AlN recipe was achieved by studying the XRD pattern evolution on variation of different sputtering parameters described above. Finally, the film stoichiometry deposited via a optimised sputtering recipe is studied using electron dispersive spectroscopy EDX.

5.3.1 Crystalline and Piezoelectric Property of AlN

AlN is a closely-packed non-centrosymmetric hexagonal wurtzite structure. The Al and N sublattices are displaced by 0.192 nm (c-axis)in a tetrahedral coordination, leading to the observed non-centrosymmetric lattice, which results in different properties along different polar directions. The non-centrosymmetric structure of AlN also plays a key role in the observed piezoelectric property of the material [198].

AlN lattice comprises two types of Al-N bonds within its crystal lattice- B_1 & B_2. B_1 requires low energy for its formation and is often found in {1010} plane, while {0002} and {1011} plane comprises both B_1 and B_2 and requires higher energy for the bond formation. Therefore highly energetic adatoms are favoured for the formation of {0002} and {1011} planes. Besides, higher energetic adatoms, lower deposition rate also favours the formation of highly c-axis oriented AlN [199].

5.3.2 Experimental methods

Plassys MP 900s Sputter Tool housed in JWNC at the University of Glasgow was utilised for the deposition of the AlN. AlN was deposited via low temperature RF reactive magnetron sputtering process. The film deposition was carried out in a low temperature process to enable the deposition over a wide range of polymer substrate.

AlN was sputtered using high purity Al target (150 mm in diameter) in N_2 and Ar gaseous mixture. Ar^+ in the plasma discharge are accelerated towards the target (anode) where the collision results in the ejection of the target atoms, which are carried towards the substrate in a vacuum. During the sputtering process the high energy sputtered particles and other species in the plasma collide with the Ar atom and cool down in a process called thermalisation. This process results in the reduction of the flux of energetic particles towards the substrate, resulting in a thinner film. Besides flux, energy of the flux of particles towards the substrate is another key parameter, as it can have a positive or negative influence on the substrate. The higher energy of flux can improve the adhesion of the film to the substrate, resulting in a denser film. However, too high energy flux can also result in damage to the film and substrate.

A n-type Si substrate was cleaned via ultrasonication acetone, isopropanol and RO water successively and blow-dried with N_2 gas. A 100 nm Al was deposited via e-beam evaporation at pressure of 2×10^{-6} mbar. Following the deposition, the substrate was immediately loaded into the load-lock chamber of Plassys MP 900s Sputter Tool for the sputtering. After the chamber was evacuated to 2×10^{-7} mbar, high purity Ar gas was introduced into the chamber. Prior to sputtering, a pre-sputtering was performed for 10 mins in Ar atmosphere with a closed target shutter, ensuring the removal of any oxides or contaminants from the target which could affect the deposited film. The AlN deposition was carried out with the substrate held at a constant distance of 59 mm from the target, thus ensuring the deposition of uniform film. The AlN film was initially sputtered at the following conditions: sputter chamber pressure- 3 mTorr; RF power- 700 W, N_2 : Ar gas flow rate of 50 sccm: 20 sccm, which resulted in the first observation of (0002) orientation in the AlN film. Subsequently, parameters were individually varied, while ensuring the other two parameters were kept constant during the deposition process. The influence of the varying of the sputtering conditions on the crystal orientation and surface morphology of the film was studied using XRD and AFM. Finally, electrical and EDX characterisation was performed on the AlN film deposited via optimised recipe, where optimised recipe refers to the sputtering conditions that yielded in the high c-axis oriented film. Table 5.1 summaries the different sputtering conditions adopted for the optimisation of the c-axis oriented AlN film.

Parameters	Value
Pressure (mTorr)	3, 4, 5
RF power (W)	500, 600, 700
N_2 : Ar gaseous flow(sccm)	50:20, 50:30, 50:50
Deposition time (min)	120

Table 5.1: Sputtering conditions used during AlN sputtering process to achieve a highly c-axis oriented film.

5.3.3 Results and Discussion

Pressure Influence on c-axis Orientation

The influence of pressure on the c-axis orientation of the film was studied for different pressure of 3 mTorr, 4 mTorr and 5 mTorr respectively, while other parameters were kept constant. The XRD spectra of the AlN sputtered at different pressure is depicted in Figure 5.5 .The peaks observed at $2\theta = 33.2^o, 36.03^o, 37.87^o$ correspond to AlN $(10\bar{1}0)$, AlN(0002) and AlN$(10\bar{1}1)$ respectively. The peak observed at $2\theta = 38.6^o$ corresponds to (111) of face centred cube of Al [200]. As depicted in Figure 5.5, higher sputtering pressure resulted in a highly c-axis oriented film with other peaks associated with AlN(100) and AlN(101) disappearing at higher pressure. Higher pressure results lower mean free path thereby resulting in atoms with lower kinetic energy due to multiple collisions, thereby favouring the (0002) orientation. The surface morphology of AlN film sputtered at different pressure is shown in Figure 5.6. The lower pressure results in higher mean free path, attributing to atoms with higher energy bombarding the sputtered film, thereby resulting in film with higher roughness.

Sputtering Power Influence on c-axis Orientation

Sputtering power is another key parameter whose influence on c-axis orientation was investigated. AlN film was sputtered at 3 different powers of 500 W, 600 W and 700 W. The XRD scan of AlN film deposited at different power is shown in Figure 5.7a. The deposition rate increased with higher power leading to a thicker film as shown in Figure 5.7b owing to higher sputtering yield. Higher RF power results in more efficient collisions between the Ar^+ in the plasma discharge and target, ensuing more Al atoms being ejected from the target, leading to a film with a higher thickness. However, higher RF power affected the crystal orientation of the sputtered film as is evident from the XRD pattern of the AlN film depicted in Figure 5.7a. Increasing RF power results in the origin of new peaks associated with other AlN crystal orientations. Higher RF power leads to highly energetic flux of atoms towards the substrate. This highly energetic atoms results in the formation of $(10\bar{1}1)$ plane which requires a higher bond energy.

Besides, the high energy closer packing of adatoms are prerequisite to achieving a well-oriented (0002) plane. This requires a longer dwelling time of adatoms to

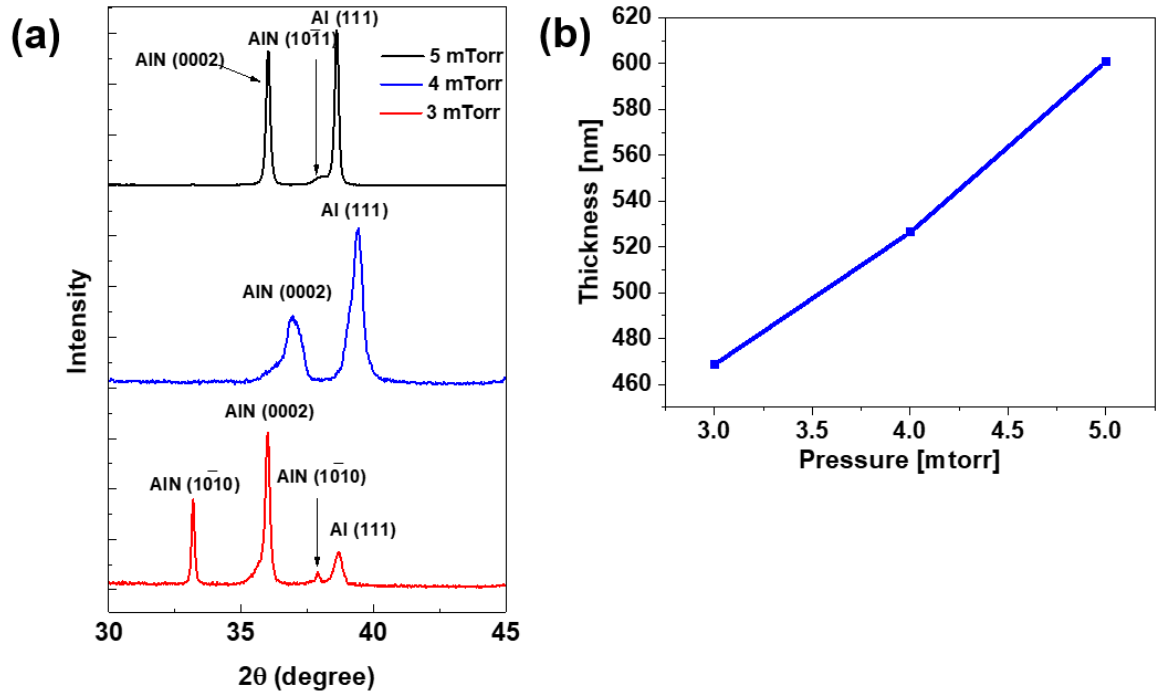

Figure 5.5: XRD spectra of AlN sputtered at a pressure of 3 mTorr (black), 4 mTorr (blue) and 5 mTorr (red) with higher pressure resulting in more highly oriented film. (b)Thickness of AlN deposited at different pressure.

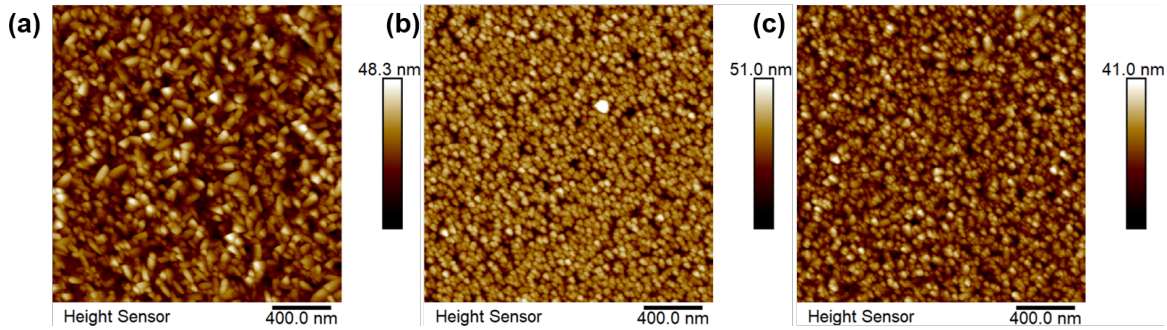

Figure 5.6: Surface morphology of AlN film sputtered at different sputtering pressure of (a) 3mTorr, (b)4 mTorr (c) 5 mTorr. The surface roughness of the film decreased with increasing pressure with Ra= 5.87nm(3 mTorr), 5.63 nm(4 mTorr) and 4.79nm (5 mTorr)

accommodate into lower energy lattice sites before the arrival of the next adatoms,thus a low deposition rate is key to achieving a (0002) oriented film. A higher power leads to a faster deposition rate, hence as a result at higher power we observe origin of (10$\bar{1}$1) orientation, which is favoured by loose packing and high energy. Further, highly energetic flux leads to a rougher surface morphology of the film, as is evident from AFM scan shown in Figure 5.8. The surface roughness of the film increases from 2.89 nm to 5.87 nm for the highest RF power.

Gas Flow Ratio Influence on c-axis Orientation

Figure 5.9 shows the XRD pattern of AlN deposited at various gaseous compositions. The impact of gas flow ratio on the sputtered AlN film is investigated for varying gas

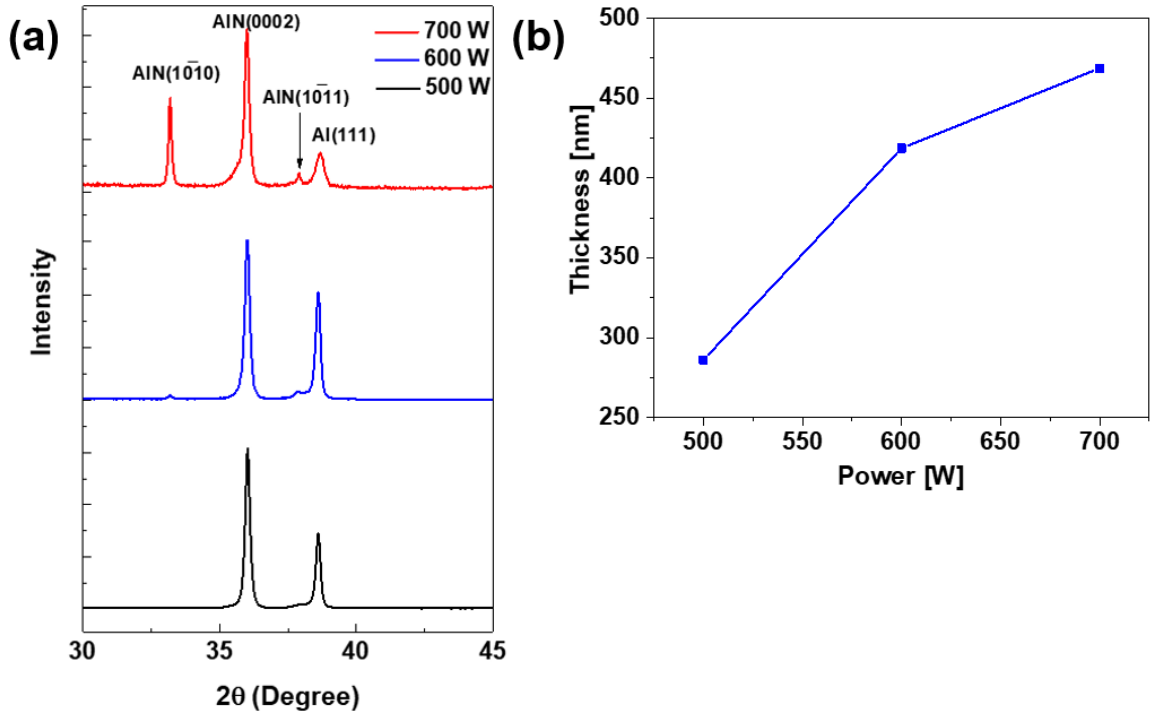

Figure 5.7: (a)XRD spectra of AlN sputtered at a pressure at different RF power of 500 W (black), 600 W (blue) and 700 W (red). (b) Thickness of AlN film deposited at different power.

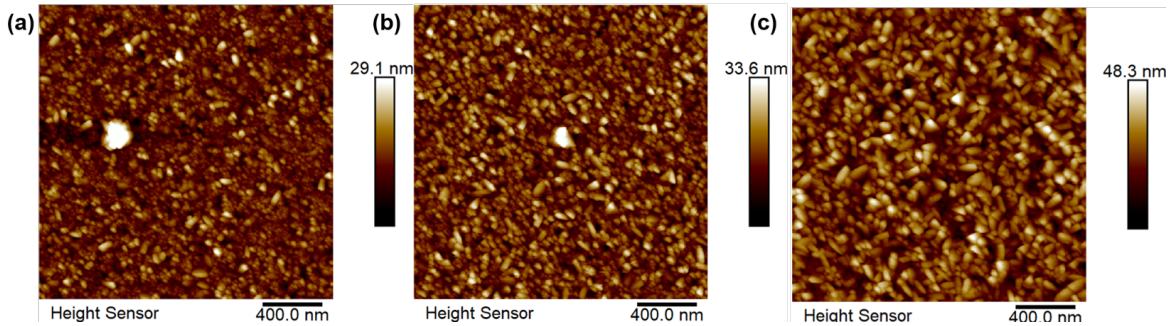

Figure 5.8: AFM scan of film deposited at RF power of (a) 500 W (b) 600 W and (c) 700 W. Average roughness of the films were 2.89 nm, 3.77 nm and 5.87 nm for RF power of 500 W, 600W and 700 W respectively.

flow ratio, while the pressure and RF power are held at constant value of 3 mTorr and 700 W respectively. The composition of gas within the sputtering chamber affects the stoichiometry of the film and may introduce defects within the film, affecting its property. During the process, the flow of N_2 was maintined at constant value of 50 sccm, while the Ar flow rate was varied to 20 sccm, 30 sccm and 50 sccm attributing to a gas flow ratio of 2.5:1, 1.6:1 and 1:1. The evolution of the XRD results shown in Figure 5.9a for varying gas flow ratio can be explained as follows: At a gas flow ratio of 2.5:1 results in the film comprising (10$\bar{1}$0), (0002) and (10$\bar{1}$1) orientation. The formation of such orientation is due to the formation of reactive species with varying kinetic energy. The increase in the Ar flow results in sharp peak associated (0002) orientation. The increase in Ar flow ratio results in higher Ar neutral atoms within the chamber. The bombardment between Ar atoms and adatoms results in

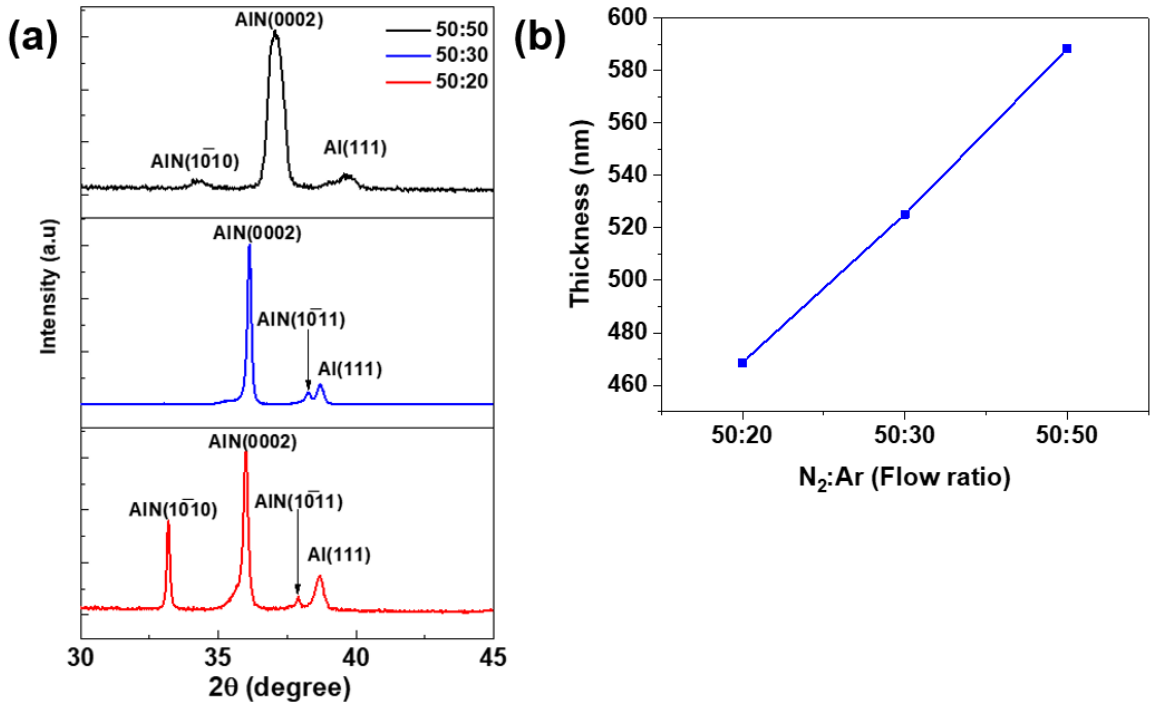

Figure 5.9: (a)XRD spectra of AlN sputtered at 700 W, 3 mTorr and varying N_2 : Ar flow ratio of 50:20 (red spectra), 50:30 (blue spectra), 50:50 (black spectra). (b) AlN film thickness for varying gas flow ratio.

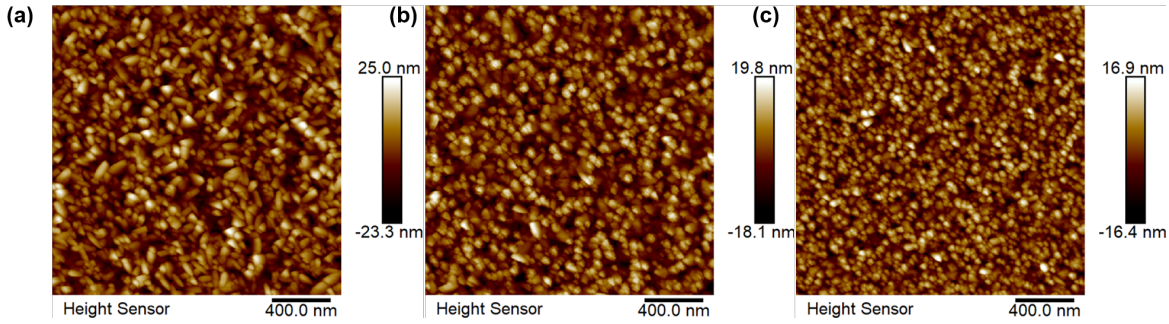

Figure 5.10: AFM image of surface morphology of AlN sputtered at N_2 : Ar flow ratio of (a) 2.5:1 (b) 1.7:1 (c) 1:1.

the re-sputtering of the film with adatoms with lower kinetic energy. This provides optimal conditions with required deposition rate and energy for the (0002) orientation of the film [199]. Further increase in Ar (results in higher deposition rate due to higher sputtering yield of Ar^+ resulting in thicker film (Figure 5.9b)) results in loosely-packed film, thus resulting in beginning of (10$\bar{1}$0) orientation as shown in the XRD pattern. The AFM image of AlN film sputtered at varying gas flow ratio is shown in Figure 5.10. The average roughness of the sputtered film increases with higher N_2 flow, which is attributed to the lower sputtering yield.

c-axis Oriented AlN Film

AlN was sputtered at the following condition post investigation of the influence of different parameters: RF power- 500W; sputtering pressure- 5 mTorr; N_2 : Ar flow

ratio- 50:30. The XRD pattern shown in Figure 5.11 reveals the deposited film with high c-axis orientation due to the observed peak at 36.03^o and absence of peak associated with $(10\bar{1}0)$ and $(10\bar{1}1)$ peak. Figure 5.12 shows the SEM image of surface morphology and cross-sectional of the sputtered AlN film. The pebble like surface morphology of AlN depicted in Figure 5.12a is a common feature of (0002) orientation growth which has also been reported other research groups [199]. Further, the cross-sectional image of the AlN depicts a columnar growth, which is another feature associated with (0002) orientation of AlN film.

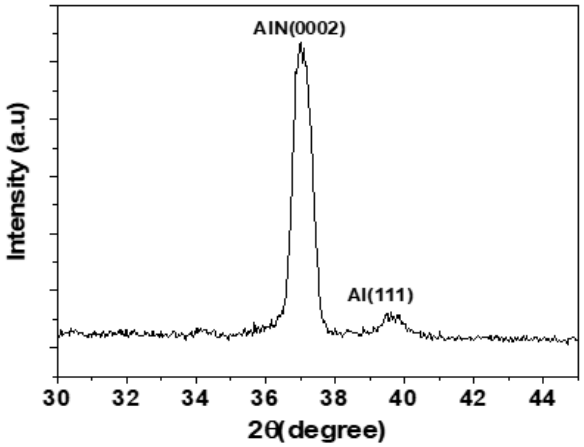

Figure 5.11: XRD pattern of AlN sputtered using the optimised sputtering recipe. The observed peaks are attributed to (0002) orientation of AlN and (111) of Al bottom electrode.

The EDX was performed on sputtered film using the X-Flash EDX detector equipped with SEM SU8240 to determine the atomic composition of the sputtered film. The EDX spectra of AlN is shown in Figure 5.13. The percentages of Al and N composition in the sputtered film are 40.36% and 38.91% respectively corresponding Al:N ratio of 1.03:1 which is closer to the ideal stoichiometry ratio of AlN. The Si and O content observed in the EDX spectra arises from the substrate and its native oxide.

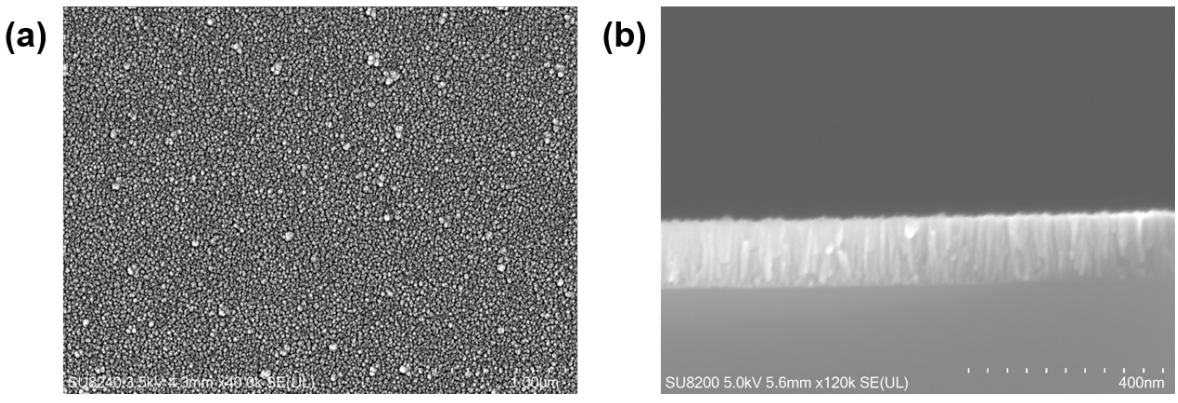

Figure 5.12: SEM micrograph of sputtered AlN film (a) Surface morphology (b) Cross-section of sputtered AlN film exhibiting a columnar growth characteristics of (0002) orientation.

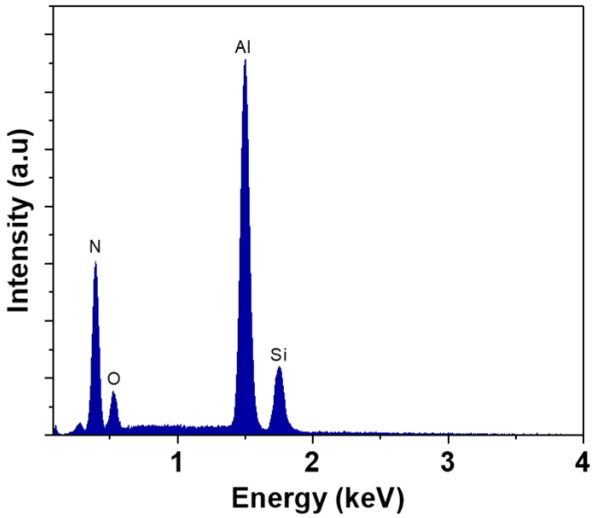

Figure 5.13: EDX spectra of AlN on Si substrate depicting the elemental composition of the film. The Si and O observed in the EDX spectra arises form the substrate (Si) and the native oxide formed on the Si substrate.

5.4 Chapter Summary

The ability to deposit high-quality uniform high-κ dielectric on graphene would be a crucial step towards the development and integration of graphene-based devices. Especially, with regard to the development of top gate GFET, it is critical, as it would enable good electrostatic control of the channel and improve device performance and reliability. ALD is one of the most promising routes for the deposition of high-quality dielectric on graphene. In this regard, thermal ALD process was adopted for the deposition of the high-K Al_2O_3 on graphene. A thin layer of Al deposited in O_2 ambient was used as the seed layer for initiation of uniform ALD of Al_2O_3 on graphene. The ALD deposited film on the graphene exhibited a uniform coverage and average roughness of 0.79 nm confirmed by AFM scan. Further, the Al_2O_3 also exhibited a good electrical characteristics as is evident from its C-V and I-V characterisation respectively, showing its promise as gate dielectric for the development of top gate GFET. A 30 nm Al_2O_3 exhibited a dielectric constant of the 7.46 with low leakage current, showing the good insulating property of the deposited film, therefore enabling its use as a gate dielectric for the top gate GFET.

The second section of the chapter discusses the optimisation of the low temperature sputtering process to achieve a highly c-axis oriented film. The highly c-axis oriented film was investigated as piezoelectric transducer layer for pressure sensing application. The AlN deposition was carried out using a low temperature RF reactive magnetron sputtering system. The impact of different sputtering parameters such as pressure, gas flow ratio, RF power on c-axis orientation of the film, is investigated. A highly c-axis oriented film was achieved at the following conditions RF power 500 W, N_2 : Ar flow ratio of 50:30 and 5 mTorr pressure. The film sputtered at this optimal condition exhibited a good stoichiometry ratio and colomunar growth, as confirmed by EDX and SEM analysis. Further, AlN/Al_2O_3 stack is investigated as a gate dielectric for

a flexible GFET and electrical characterisation of the deposited film is discussed in Chapter 7.

Chapter 6

Graphene Field Effect Transistors

6.1 Introduction

Graphene has become one of the most sought after materials in recent times, owing to its intrinsic material characteristics such as fascinating electrical, mechanical , thermal and optical properties. One of the most promising applications of graphene is in the field of nanoelectronics and optoelectronics devices, due to its high carrier mobility, single atomic layer thickness and broadband absorption etc. However, the lack of band-gap in graphene limits its potential for digital applications and make it more suitable for RF device applications. Recent demonstration of devices with high cut-off frequencies have shown its potential for such applications [201]. Initial electrical studies on graphene were based on the exfoliated graphene, however the industrial scalability of the process limits its potential. In this regard CVD grown graphene is an attractive choice as it would enable a commercially viable route for large area synthesis of graphene. This chapter presents a study on the development of top gate GFET which is employed as the active device in the development of GFET based pressure sensor.

6.2 Materials and Methods

The fabrication of GFET was initiated by wet transfer printing process of graphene (CVD grown graphene from Graphenea) to SiO_2/Si substrate using CAB as polymer scaffold. The transfer process is described in detailed in Chapter 4. The key steps of the fabrication process are represented schematically in Figure 6.1. A 4 nm of Al was deposited at slow rate (0.05 nm/s) using Plassys-e-beam evaporator on graphene as a sacrificial layer. Direct photolithography on graphene, leaves photoresist residue on graphene affecting its electrical property and source/drain metal electrode-graphene interface. Traditionally, the organic residues are removed by subjecting the sample to O_2 plasma. However, such methods cannot be employed in graphene device fabrication owing to the poor selectivity between graphene and the residues. Therefore, to minimise the residues from photolithography, a sacrificial Al layer was employed. This sacrificial Al layer was removed by the photoresist developer MF319 (consists

of dilute tetramethylammonium hydroxide (TMAH) which aids in the removal of Al) during the development of the photoresist for source and drain electrodes deposition. Following the transfer of graphene to the destination substrate, the graphene channel definition and isolation was achieved using photolithography and RIE etching in O_2 plasma at 300 W for 13 s, resulting in a channel width of 50 μm. Post definition of the graphene channel, the source and drain electrodes (10 nm/40 nm Ti/Au) were defined via photolithography, metallisation and lift-off. To ensure uniform ALD growth, the remaining Al sacrificial layer was removed using the developer, rinsed in RO water and blow-dried with a N_2 gun. Subsequently, a 3 nm thick Al was deposited via e-beam evaporation prior to ALD in O_2 ambient, serving as the seed layer for the subsequent ALD process. The top gate dielectric, Al_2O_3 was deposited via thermal ALD using TMA and H_2O as the gaseous precursor at 200^{o}C. The details of the ALD process is presented in Chapter 3. Subsequently, top gate electrode (10 nm/40 nm Ti/Au) of GFET was defined via photolithography, e-beam evaporation and lift-off, resulting in gate length of 50 μm - 20 μm respectively. The via to the source/drain contacts were opened by controlled etching of Al_2O_3 with diluted HF (100:1 H_2O : HF). The optical microscopy image and the cross-sectional scheme of the top-gate GFET is shown in Figure 6.1g and h respectively. The impact of the different process involved in the fabrication of devices on the transferred graphene was investigated using AFM, and Raman spectroscopy. The electrical measurement of the fabricated GFET was performed using Keysight B1500A semiconductor device parameter analyser in ambient conditions.

6.3 Results and Discussions

Figure 6.2 shows the AFM scan surface morphology of graphene before and after (prior to ALD deposition) the photolithography on graphene. The surface roughness of the graphene evolved from average roughness of 0.89 nm to 1.65 nm post processing prior to the ALD deposition. The observed residues are attributed to the residual remains of polymer scaffold and photoresist residue used for the patterning of graphene. It is critical to achieve a clean graphene surface as the residues act as a charge scattering point, limiting the transistor performance. Therefore it is of interest to achieve a highly cleaned graphene surface. In addition to the AFM scan the quality of the transferred graphene was also evaluated via Raman spectroscopy. A representative Raman spectra of the transferred graphene is shown in Figure 6.3. The absence of D-peak (associated with defect in the crystal lattice of graphene) in Raman spectra indicates a transfer of high quality graphene. Further, a sharp 2D peak with Lorentzian fitting of FWHM of 30 cm^{-1} and with intensity $\sim$ 2 times higher than G-peak are a further indications of a high quality transfer of graphene.

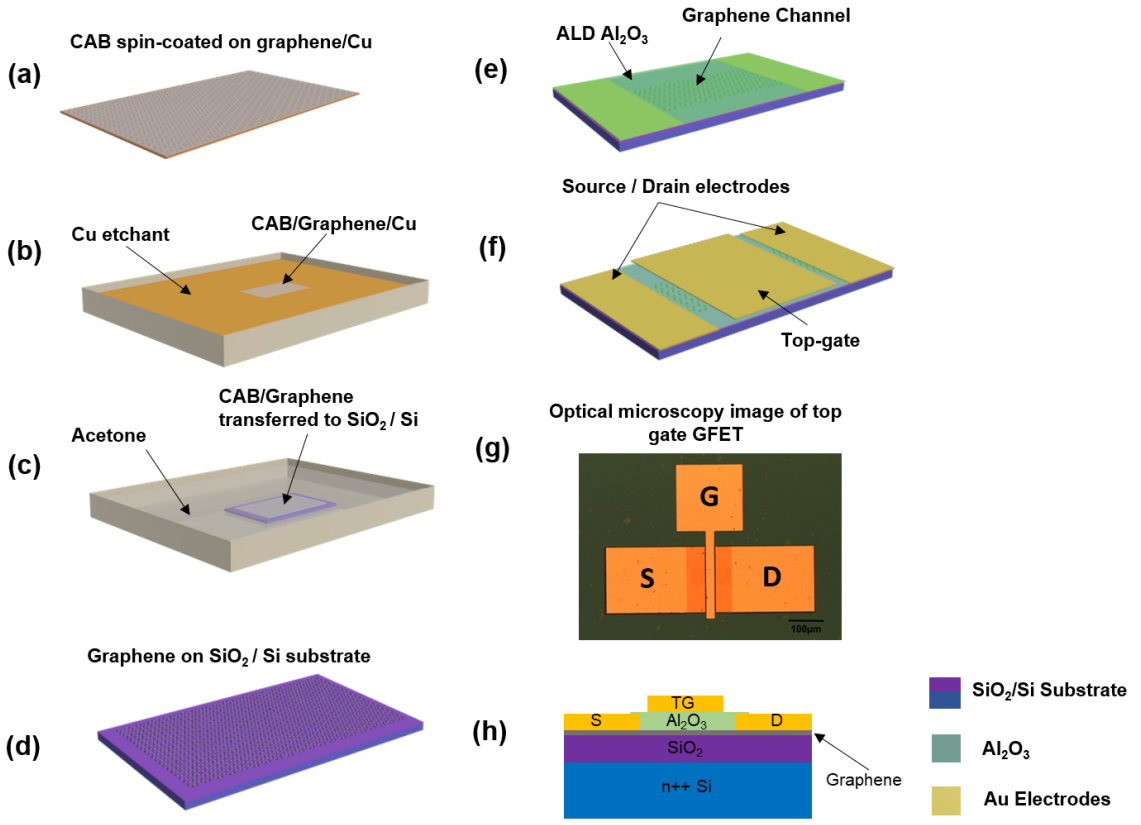

Figure 6.1: Schematic representation of key fabrication process of top-gate of GFET: (a) CAB spin-coated CVD graphene on Cu (b) Etching of underlying Cu in iron (III) chloride. (c) Graphene transferred to destination substrate (SiO_2/Si) and solvation of CAB by immersion in acetone. (d) Graphene on SiO_2/Si substrate. (e) Deposition of source and drain electrodes post definition of channel and ALD of top-gate dielectric (Al_2O_3). (f) Defintion of top gate electrodes (Ti/Au). (g) Optical microscopy image of top-gate GFET. (h) Cross-sectional scheme of top-gate GFET.

6.3.1 Electrical performance

Among the various intrinsic properties of graphene, its electronic property has attracted significant interest, with a promise as material of choice in the post-silicon era. In this regard, GFET offers an ideal platform to investigate graphene's electrical properties. This significant interest in graphene is a result of its high carrier mobility, which has a significant influence on the current intensity and frequency response of the device. However, often such high performances are achieved using the suspended graphene channel devices with measurements being carried out at cryogenic temperature ($\sim$ 5 K). The aforementioned scenario would resemble an intrinsic graphene free from any external influences such as substrate-graphene interaction (resulting in doping, phonon scattering interaction), presence of grain boundaries and reduction in impurities scattering and thermally generated charge carriers. Nonetheless, such conditions are not ideal, as they limit the scalability of graphene-based devices. In this aspect, graphene supported on substrate has become a natural choice for the development of graphene-based devices. However, it should be noted that such a device demonstrates a slightly lower mobility ($\sim 10^4$ cm^2/V.s) due to the above discussed detrimental effects.

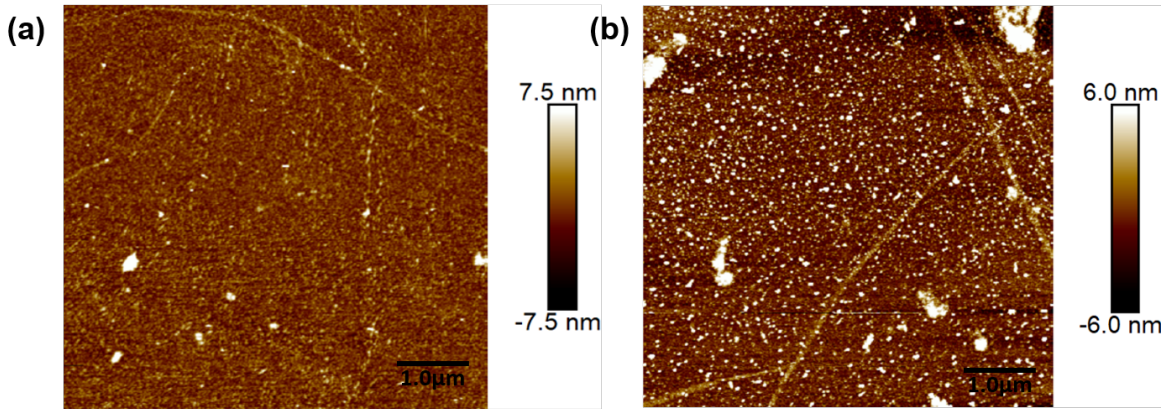

Figure 6.2: AFM scan of surface morphology of graphene (a)Post transfer to destination substrate. (b) After definition of graphene channel.

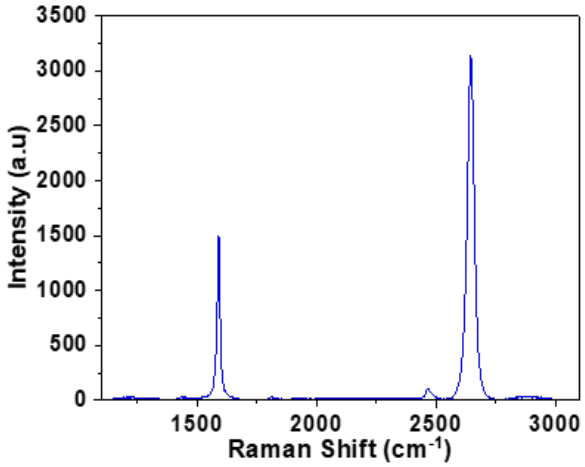

Figure 6.3: Representative Raman spectra of transferred graphene with 532 nm laser.

The impact associated with substrate-graphene interaction can be minimised by the development of 2D material heterostructure. For instance, hexagonal boron-nitride (h-BN) as a substrate resulted in an improved carrier mobility in comparison to devices developed on SiO_2/Si substrate. This is due to similar lattice constant between h-BN and graphene and lower charge impurities due to single atomically flat surface.

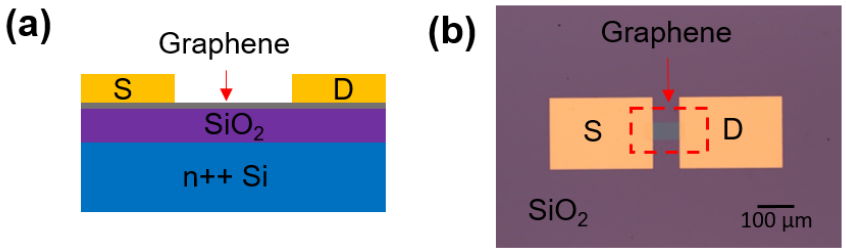

Figure 6.4: (a) Scheme of device cross section. (b) Optical microscopy image of back-gate GFET

Back-gate GFET

The electrical characterisation of graphene requires it to be transferred to an insulating substrate. Therefore, CVD graphene was transferred to a SiO_2/Si substrate. The transferred graphene was patterned to achieve the channel definition and isolation. The source and drain electrodes were defined, resulting in a back-gate GFET. It should be noted that in comparison to back-gate GFET discussed in Chapter 4, source/drain electrodes and channel definitions were achieved via photolithography and metallisation and lift off, thereby offering an ability of further scaling of devices. Figure 6.4 depicts the scheme of the device cross-section and optical microscope image of back-gate GFET. The electrical characterisation of the device was performed in ambient conditions and typical electrical characteristics of the device is shown in Figure 6.5. The transfer characteristics of the devices exhibited a typical ambipolar behaviour, as shown in Figure 6.5a , where the current conduction occurs both due to holes and electrons. The device exhibited a p-type doping and hysteresis behaviour, with a positive shift in the CNP of the GFET. On an average CNP of 34 GFET devices exhibited a a positive shift of 8.98 V. The positive CNP and its positive shift during the gate bias sweep is attributed to the doping from the ambient and polymeric residues on the graphene. The origin of the hysteresis is the result of trap charges at the interface and at the bulk. As the gate is swept from a negative bias towards a positive bias, the holes from the graphene are trapped into the trap centres present at graphene-SiO_2, and as a result the graphene is subject to higher positive bias than one from gate (opposite behaviour would be observed as the bias is swept from positive to negative bias). These trapped charges remain until the polarity of the gate bias is switched. Further, the observed vertical shift in the CNP of GFET is due to the effect of the charge screening from the trapped charge carriers. If the gate bias is swept from negative to a positive bias, CNP of the GFET would be shifted downwards as a result of holes being injected into the trap sites. However, if the gate bias is swept from positive bias, it would result in injection of electrons into the trap sites resulting in CNP being shift up [202].

The magnitude of observed hysteresis is influenced by factors such as gate voltage range, its sweep rate. A larger gate voltage range and lower sweep rate would result in higher hysteresis. A lower sweep rate would result in a longer duration for charge trapping thereby resulting in higher hysteresis. The SiO_2 dielectric of the back-gate GFET comprises interface and bulk oxide traps whose charge states are influenced by the gate bias. The interface charge traps states are continuously altered with the gate bias, while the change in bulk oxide traps would require a higher electric field. Therefore, at higher gate voltage range, charge carriers from graphene channel are injected into the bulk oxide traps, thereby resulting in higher hysteresis. The carrier mobilities of the devices were evaluated using the peak transconductance methods and fitting methods described in Chapter 3, with each method having its own pros and cons. In PTM the mobility is determined by using Equation 3.2, where the mobility, $\mu = (L_g/W_g.C_g.V_{ds})g_m$, where L_g is the channel length, C_g is the back oxide gate

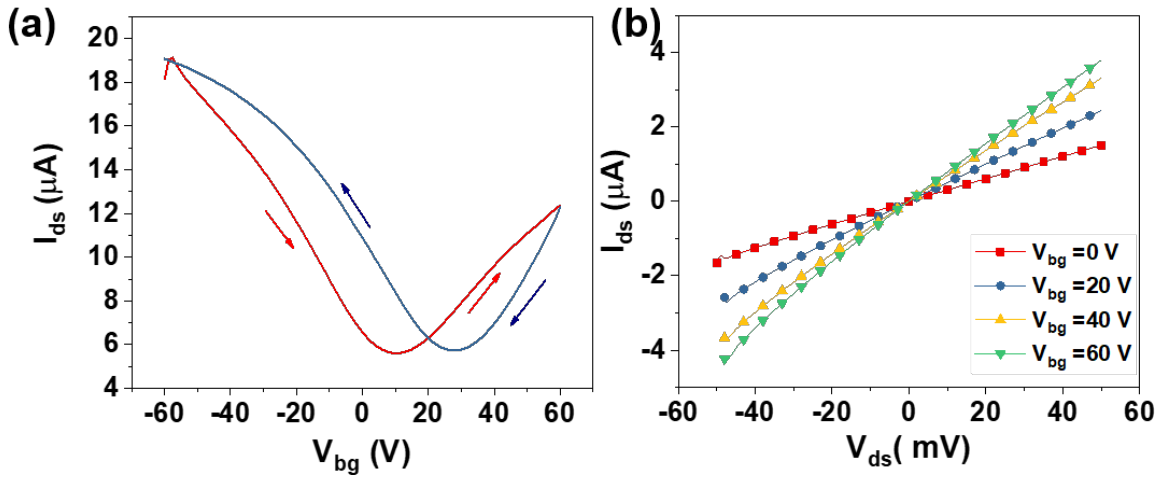

Figure 6.5: Electrical characteristics of back-gate GFET measured at ambient conditions (a) Transfer characteristics of GFET at V_{ds}= 50 mV. A double sweep of gate bias (i.e. sweeping the gate voltage from negative value to positive and positive to negative) results in a hysteresis (17.5 V). The direction of sweeping of gate bias is shown indicated by the arrows. (b) Output characteristics of GFET for varying gate voltage, V_{bg}.

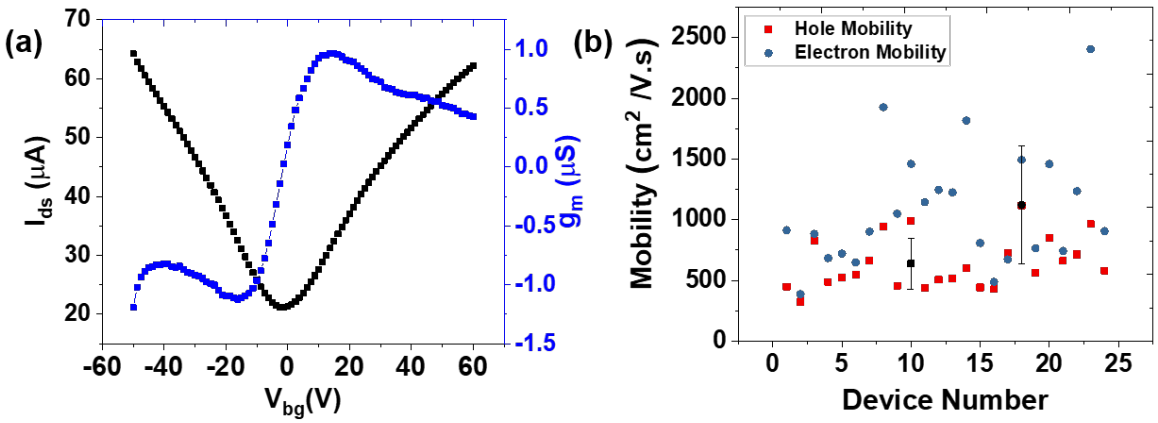

Figure 6.6: (a) Transfer characteristics and transconductance of GFET at V_{ds} = 100 mV. (b) Statistics of hole and electron mobilities determined using PTM method.

capacitance of 300 nm SiO_2 , V_{ds} is the drain bias and g_m is the peak transconductance. The typical transfer curve and transconductance of the device is shown in Figure 6.6a. The hole and electron mobility statistics of different devices shown in Figure 6.6b. The PTM method generally tends to underestimate the mobility at any carrier density, as the contact resistance is not taken into account during the extraction of the mobility. However, the accuracy of the PTM can be improved by using long channel devices with the good contact. The average electron and hole mobilities of GFET devices extracted via PTM are 1121 $cm^2.V^{-1}s^{-1}$ and 638 $cm^2.V^{-1}s^{-1}$ respectively.

Another widely-adopted method for determining the carrier mobility in graphene is DTM, discussed in Chapter 3. Similar to PTM, the carrier mobility is extracted using the transfer curve of GFET. This is done by fitting the transfer curve with Equation 3.3 and Equation 3.4. In addition to mobility, the DTM model also provides series resistance,R_s and residual carrier density.The average hole and electron mobilities

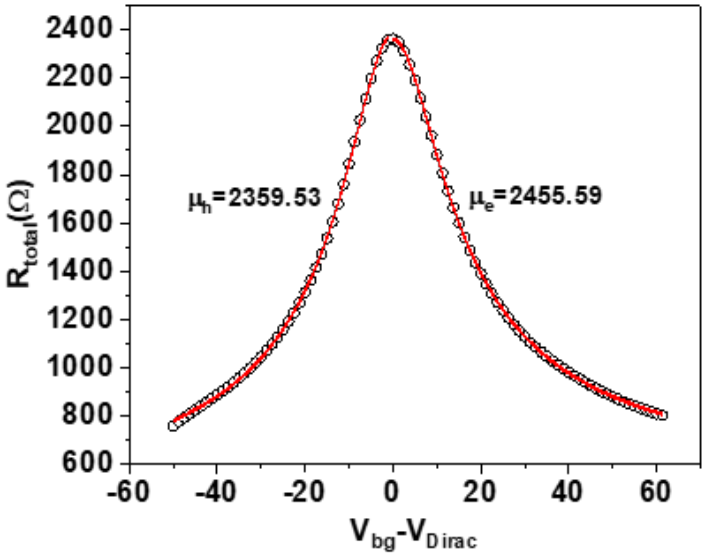

Figure 6.7: Carrier mobility extraction of GFET at V_{ds}=100 mV using DTM methods. Black circles represent the experimental data, while the red lines indicate the fitting.

of GFET extracted from DTM method are 2544.27 cm^2/V.s and 2457.74 cm^2/V.s. The carrier mobility extraction using the DTM method is shown in Figure 6.7 .

The series resistance, R_s extracted from DTM method is the sum of channel resistance,$R_{channel}$ and source and drain contact resistance, R_c i.e. $R_s = R_{channel} + 2R_c$. The average series resistance for hole and electron branch are 762.93 Ω and 1167.31 Ω respectively. The channel resistance of the device is given by Equation 6.1 [203]. Graphene's sheet resistance at Dirac point is given by $\rho_G = \frac{R_{channel}}{L/W}$ [204].

$$R_{channel} = \frac{L/W}{\mu n(V_{bg})q} \tag{6.1}$$

The contact resistance of graphene arises as a result of carrier transport at metal-graphene interface. The transport can be considered as two cascading events: injection of carriers from metal to underlying graphene; Subsequent transport of carrier into the graphene channel [205]. The transport of charge carriers into the channel is impeded by the formation of pn junction near the metal-graphene contact. The formation of pn juction is due to charge transfer doping due to work-function difference between graphene and metal and lower density of states [206–208]. This results in the Fermi-level of graphene being shifted in order to attain the equilibrium [208], thereby resulting in an observed asymmetry in as gate bias dependent R_{total} (Figure 6.7) as the gate voltage is swept [209]. The contact resistance and sheet resistance of graphene can be determined from slope and intercept of R_{total} vs channel length, L graph at a constant net gate bias ($V_{bg} - V_{Driac} = 30V$) [210].The extracted average contact resistance and sheet resistance of the devices are 414.43 Ω and 57.86 Ω/□.

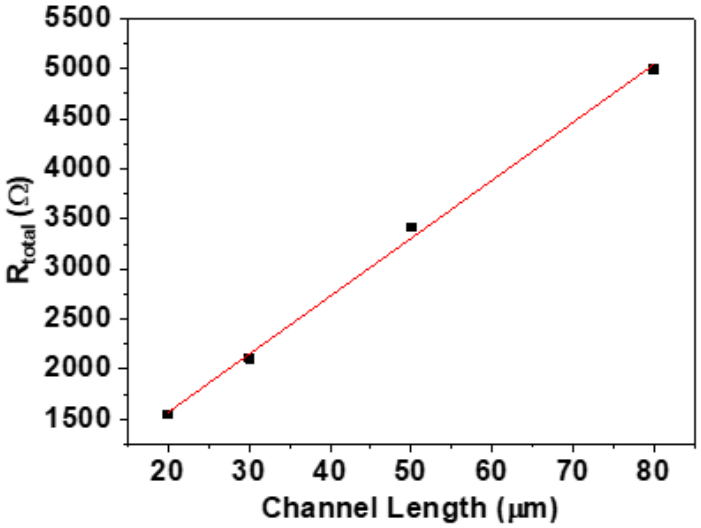

Figure 6.8: Total resistance of GFET at net gate bias of $V_{bg} - V_{Driac} = 30$ V.

6.4 Top Gate Graphene Field Effect Transistors

The top-gate GFET was used as active component of the pressure sensor. Post development of back-gate GFET, the sacrificial Al layer deposited for photolithography was removed for electrical characterisation of back-gate GFET. Subsequently, a 3 nm of Al was deposited as a seed layer in O_2 ambient to ensure a conformable and uniform deposition of ALD Al_2O_3. Al_2O_3 was deposited via a 200^{o}C thermal ALD process using TMA and H_2O as the precursors. The ALD growth condition is presented in Table 3.3. Finally, the top-gate GFET was realised via deposition of top gate electrode (Ti/Au 10/80 nm) via photolithography, metallisation and lift-off. The schematic cross section of the device is shown in Figure 6.9.

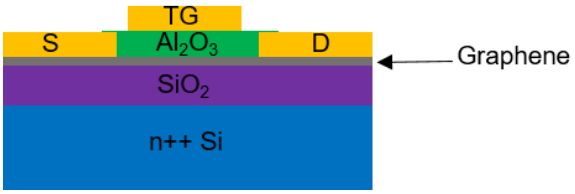

Figure 6.9: Scheme of cross-section of top-gate GFET.

To understand the impact of ALD deposition on graphene, Raman spectroscopy study was performed on graphene before and after the ALD process. Figure 6.10 shows a representative Raman spectra of graphene before and after the ALD process. The negligible D-Peak in the Raman spectra of graphene confirms that no significant damage occurs to graphene during the ALD growth process, possibly due to the Al nucleation layer protecting the graphene underneath at elevated temperatures [211]. The uniformity of ALD film was further confirmed by the AFM scan presented in Figure 5.2. As observed in Figure 6.10, ALD on graphene results in the up-shift of G-peak in the Raman spectra, this is attributed to the compressive strain on graphene due to the ALD process, thereby confirming good adhesion between the ALD Al_2O_3

and graphene [212, 213].

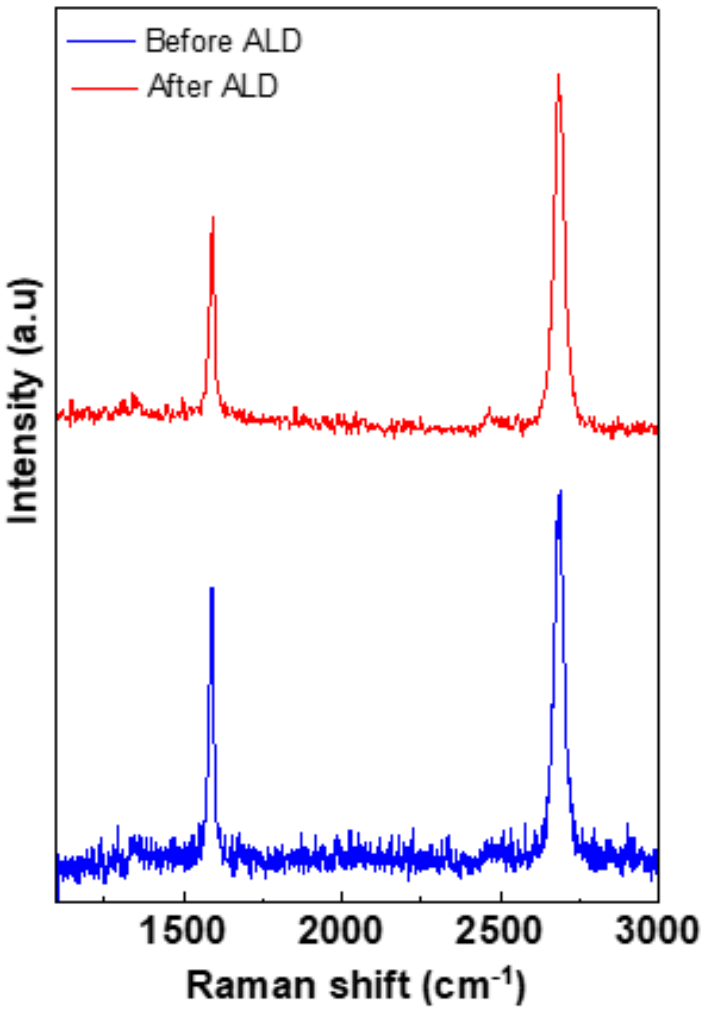

Figure 6.10: Representative Raman spectra of graphene before (blue) and after (red) thermal ALD process (laser 532 nm). The blue shift in G-Peak of Raman spectrum is a result of compressive strain in graphene.

The electrical characterisation of top-gate GFET was performed using Keysight B1500A semiconductor parameter analyser at ambient conditions. The devices exhibited typical ambipolar transfer and output characteristics of GFET is shown in Figure 6.11. As observed in transfer characteristics at V_{ds}= 100 mV, the device exhibited a hysteresis of 105 mV during the during the sweeping of gate voltage from negative to positive voltage and vice-versa. The small hysteresis indicates a minimal present of trap charges at the top-gate dielectric and graphene. As the fabricated GFET devices as relatively a longer channel length(>15 μm), the carrier mobilities of the devices were extracted using DTM. In order to extract the carrier mobility from the transfer curve of GFET via DTM method, top-gate oxide capacitance of GFET must be determined. The graphene channel's carrier concentration and type can be controlled by both top-gate and global back-gate (Si). The change in drain current, I_{ds}, for an applied top-gate bias, V_{tg}, at different back back gate voltage,V_{bg}, is shown in Figure 6.12a. The top-gate Dirac point shifts in a linear manner with respect to the applied back-gate voltage, as shown in Figure 6.12b. This observed

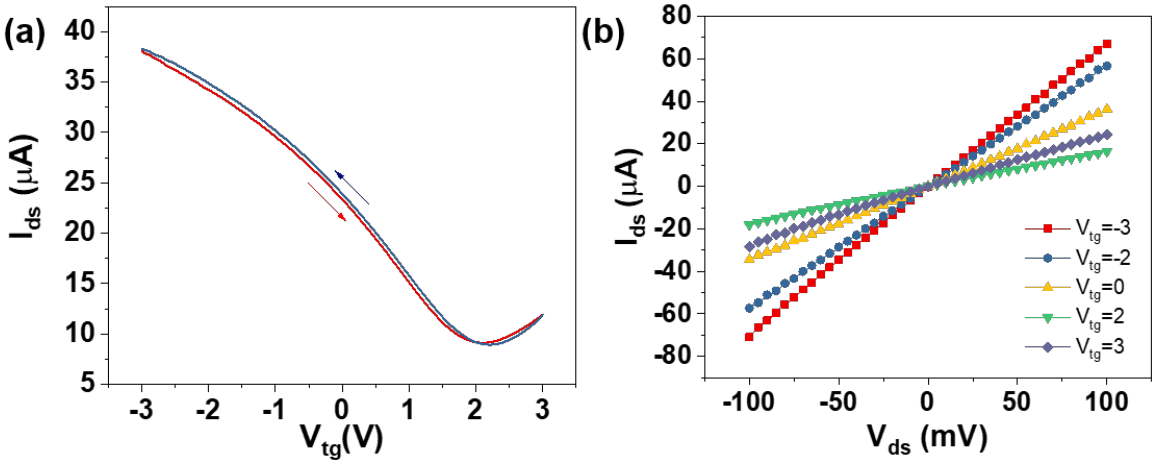

Figure 6.11: Typical electrical characteristics of top-gate GFET (a) Transfer characteristics at V_{ds} = 100 mV. (b) Output characteristics for varying gate voltage.

trend in the Dirac point shift can be described as follows: An application of negative V_{bg} results in the holes becoming the dominant charge carrier in the channel region. This requires an application of positive V_{tg} in order to for the device to reach the minimum conductance(Dirac) point. For a positive V_{bg} an opposite behaviour to the one described above would take place. The observed vertical shift in top-gate Dirac point is attributed to change in the un-gated channel resistance (refers to the region not gated by the top-gate) [170]. The inverse of the slope of V_{Dirac} vs V_{bg} is the equal to the ratio of top-gate oxide capacitance, C_{ox}, and back-gate capacitance,C_{bg} i.e. $C_{ox}/C_{bg} = -\Delta V_{bg}/\Delta V_{Dirac} = 21.51$. Using a back gate capacitance of 11.51 nF/cm^2 (This is for 300 nm thick SiO_2 with a dielectric constant of 3.9), the top-gate oxide capacitance is derived to be 247.58 nF/cm^2. Based on the capacitance value the dielectric constant of the 30 nm ALD Al_2O_3 film is derived to be 8.39. This value is closer to the dielectric constant of Al_2O_3 ($\varepsilon_r = 9$) [211] thereby confirming the deposition of high quality ALD film. However, it should also be note the derived value is higher than reported in Chapter 5, which we attribute to run to run variations of the deposited film.

The carrier mobility of top-gate GFET is extracted by fitting R_{total} vs $V_{tg} - V_{Dirac}$ with Equation 3.3 and Equation 3.4. The top-gate capacitance is a series combination of gate oxide capacitance (247.58 nF/cm^2) and quantum capacitance of graphene (2 μF/cm^2) [114]. As top-gate oxide capacitance is much smaller than the graphene's quantum capacitance, graphene's quantum capacitance could be ignored from the fitting equation.However it should also be note the derived value is higher than that reported in chapter 5, which we attribute to run to run variations of the deposited film. The carrier mobility of top gate GFET is extracted by fitting R_{total} vs $V_{tg} - V_{Dirac}$ with Equation 3.3 and Equation 3.4. The total resistance of device, R_{total} is determined by $R_{total} = V_{ds}/I_{ds}$. Figure 6.13 shows the fitting of R_{total} vs $V_{tg} - V_{Dirac}$ of a top-gate GFET to extract the carrier mobility, series resistance (access resistance(due to un-gated graphene channel), channel resistance and contact resistance) and top-gate

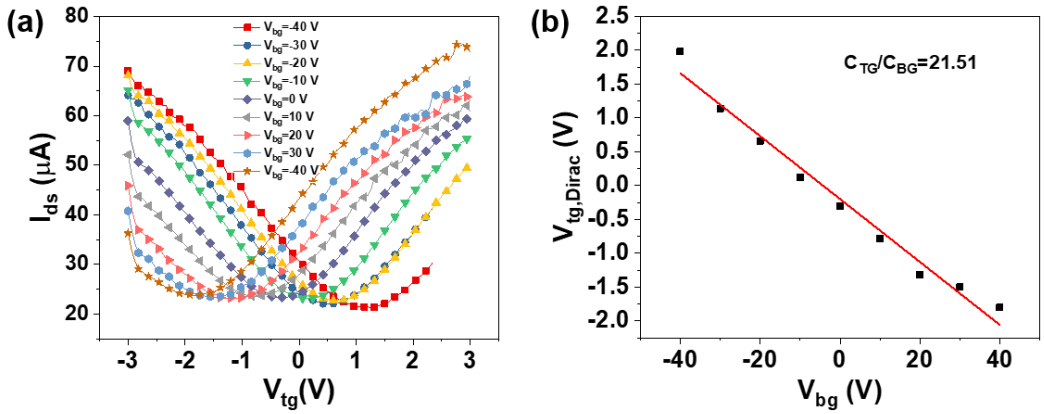

Figure 6.12: (a) Measured I_{ds} vs V_{tg} for different V_{bg}- +40 V (left) to -40 V (right) in steps of 10 V, V_{ds} =100 mV. (b) Top gate Dirac point voltage as a function of back-gate V_{bg}.

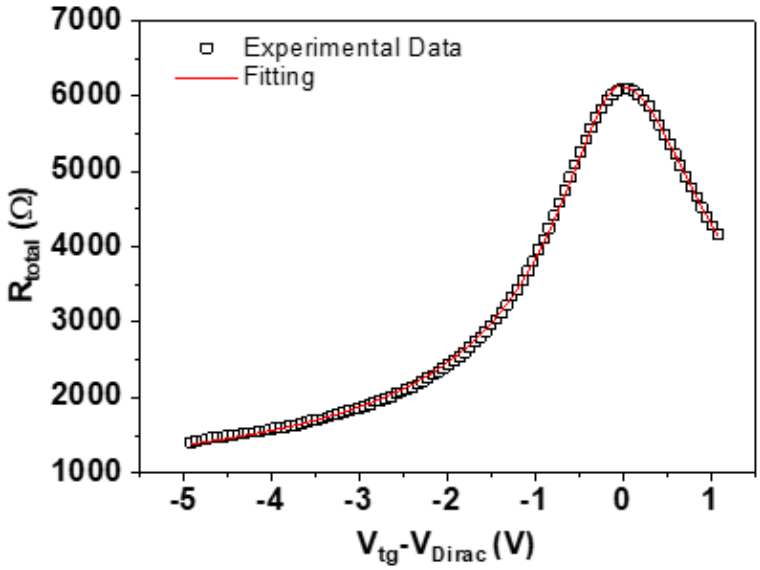

Figure 6.13: The total GFET resistance (R_{total}) vs top-gate voltage with respect to Dirac point ($V_{tg} - V_{Dirac}$) at V_{ds} = 100 mV. The experimental data are represented by the square symbols, while the fitting is represented by the red line.

modulated carrier density. The typical fitting of R_{total} vs $V_{tg} - V_{Dirac}$ of top-gate graphene field effect transistor is shown in Figure 6.13. The extracted average hole and electron mobilities of the top gate GFET was 1222 cm^2/V.s and 1339 cm^2/V.s respectively.

6.5 Chapter summary

This chapter presents the fabrication and characterisation of top-gate GFET which is used as the active component of the pressure sensor. A thermal ALD process was used for the deposition of high quality Al_2O_3 as the top-gate dielectric of the GFET. The compatibility of the adopted thermal ALD process on graphene was confirmed by Raman spectroscopy study on graphene before and after the ALD process. The absence

of significant defect associated D-peak in the Raman spectrum of graphene confirmed the compatibility of the ALD process. In addition, the electrical characterisation of the GFET were performed, confirming a good gate control of the device with an average hole and electron carrier mobility of 1222 $cm^2/V.s$ and 1339 $cm^2/V.s$ respectively.

Chapter 7

Piezoelectric GFET Pressure Sensor for Tactile Sensing Applications

7.1 Introduction

An integration of tactile sensors for robotic and prosthesis application would have a huge impact on how robots or amputees interact with physical objects. The sense of touch aids humans to gather key parameters of an object being handled, such as its stiffness, temperature, texture etc. Such parameters gathered via tactile sensing, aids in various functionality such as object manipulation, differentiation of objects where sense of vision could be deceived, reflex action such as regulation of grasp force [27]. Therefore, human skin would provide a good starting point for the development of electronic skin for the tactile sensing for robotics and prosthesis application [22]. The tactile sensing of human skin can be classified into two categories, namely: cutaneous and kinesthetic based on site of the input into the sensory organs. In cutaneous tactile sensing the tactile information is received from the receptors embedded within the skin, while for kinesthetic sensing the tactile information is received from the receptors embedded within the muscles and joints etc. Human skin comprises a large number of tactile sensors embedded within it, responsible for various tactile sensory information. The physical stimuli such as pressure/force, vibration are sensed via mechanoreceptors, while thermoceptors and nociceptors are responsible for stimuli related to temperature and pain, respectively [16]. Among the various sensors,mechnoreceptor is the most critical, thereby leading to various exploration of various transduction mechanism for the development of the pressure sensors such as piezoelectric, piezoresistive and capacitive. Amongst such device architecture, FET based pressure sensors are attractive as it would enable the development of sensors with high spatial resolution in an active matrix configuration to truly imitate the distributed nature of tactile sensors within the human skin. Further, FET based pressure sensors would also enable reduction of signal cross-talk, ease of integration

with electrical circuitry [94]. The development of FET pressure sensors relies on integration of transducer material with the device. Besides e-skin, development of pressure sensors would also have a profound impact on various applications such as tactile IOT [214], wearable and portable electronic devices [35]. In this regard, various novel material has been investigated for the development of FET pressure sensors such as organic material, CNT, nanowire,and graphene [45,88,90,91], with each material offering its own pros and cons for the development of pressure sensors. For instance, the development of OFET offers devices with inherent flexibility, however OFET suffers from lower carrier mobility, often requires high operational voltage and therefore are not efficient solution for the aforementioned applications [24]. In comparison, GFET is an attractive choice, owing to its high carrier mobility, excellent mechanical stability and low operation voltage. Gaining from the excellent properties of GFET, the reported tactile sensor would enable the development of high density power efficient pressure sensors vital for true mimicking of human skin. This chapter presents piezoelectric GFET based pressure sensors for tactile sensing application. The pressure sensors comprises of GFET in an extended gate configuration with a piezoelectric MIM structure. Namely,two piezoelectric material: lead zirconate titanate (PZT) and aluminium nitride (AlN) have been explored as a transducer material for pressure sensing applications. The key results of the chapter has been published in [56] [215].

7.2 Extended Gate Piezoelectric GFET Based Pressure Sensor

The pressure sensor comprises two main components: (a)GFET; (b)piezoelectric MIM structure. Two piezoelectric materials PZT and AlN were investigated as piezoelectric transducer layer for the pressure sensing applications. The extended gate configuration was achieved by forming an electrical contact between top gate electrode of GFET and bottom electrode of piezoelectric MIM structure as shown schematically in Figure 7.1.

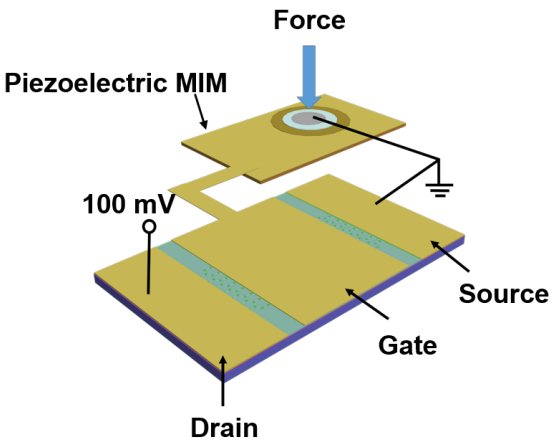

Figure 7.1: Scheme of piezoelectric GFET pressure sensor [56].

7.2.1 Lead Zirconate Titanate (PZT)

Lead zirconate titanate (PZT) is a solid solution comprising of lead titanate ($PbTiO_3$) and lead zirconate ($PbZrO_3$). PZT is one of widely used pizeoelectric material owing to its high piezoelectric constant. It is polycrystalline ceramic material belonging to perovskite family. A number of techniques have been adopted for synthesis of PZT including the sol-gel, molten salt synthesis, spray pyrolysis etc [216, 217]. In this study PZT is used as piezoelectric transducer layer for the pressure sensing application.

PZT MIM structure comprises the brass substrate with PZT as a piezoelectric layer and Ag as the top electrode. Figure 7.2 shows the SEM micrograph of surface morphology and cross-section of the PZT MIM structure.

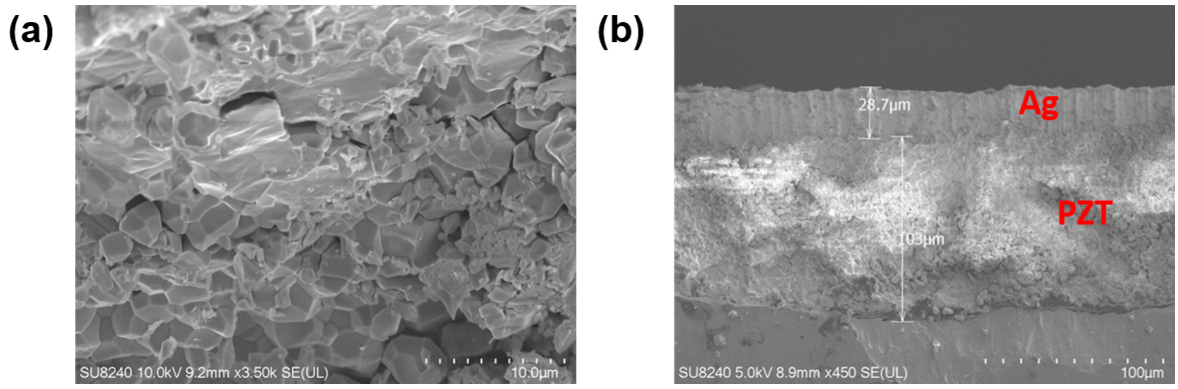

Figure 7.2: SEM micrograph of PZT (a) Surface topography of PZT. (b)Cross-sectional image of PZT MIM structure

Electrical Characterisation of GFET

The cross sectional schema and the optical microscopy image of the fabricated top-gate GFET (top-gate length- 35 μm and channel width- 50 μm) is shown in Figure 7.3a & b, respectively. The electrical characterisation of GFET was carried out using Keysight B1500A semiconductor device parameter analyser. The electrical characteristics of the GFET is shown in Figure 7.3c & d. As observed from Figure 7.3c, the fabricated device exhibited a typical ambipolar characteristics of GFET. The observed shift in the Dirac point of GFET is attributed to the unintentional doping of graphene arising from the polymeric residues and ambient doping. The carrier mobility of GFET was extracted using the widely adopted the diffusive transport model described in Equation 3.3. The carrier density, n, is related to top gate bias by Equation 3.4, where v_f is the Fermi velocity $= 1.15 \times 10^6$ m/s. $V_{tg} - V_{tg,Dirac}$ arises from the carrier density modulated by top gate capacitance and quantum capacitance of graphene. Therefore, it is critical to determine the gate oxide capacitance, in order to extract the carrier mobility of the device using the DTM method. The GFET channel can be modulated by both the top and bottom gate of GFET. The top gate Dirac point voltage ($V_{tg,Driac}$) shift with respect to back gate (V_{bg}) voltage is shown in Figure 7.3e. The inverse of the slope of graph shown in Figure 7.3e represents the ratio between the top and back gate

capacitance (C_{ox}/C_{bg}=20.41). The capacitance of the top gate dielectric (25 nm thick Al_2O_3) was calculated to be be $\sim$ 234.8 nF/cm^2 using a back gate oxide capacitance of 11.5 nF/cm^2 for 300 nm thick SiO_2.

The carrier mobility of holes and electrons were extracted by separate fitting, owing to the asymmetry in the electron and hole branch around the Dirac point. This asymmetry arises due to doping of graphene due to the metal contacts and owing to different long range scattering strength of different charge carriers at oxide/ graphene interface, thereby resulting in suppression of particular charge carriers. The fitting of the transfer curve is shown within the inset of Figure 7.3c. The extracted hole and carrier mobilities of the GFET are 873 cm^2/V.s and 830 cm^2/V.s respectively.

Electromechanical Characterisation of the Sensor

The electromechanical characterisation of the sensor was carried out using an in-house custom setup. The schematic of the pressure sensing setup is shown in Figure 7.4. The sensor performance was evaluated by applying a dynamic force of varying magnitude using the linear motor (VT-21 Linear stage from MICRONIX USA) with 1 μm precision movement controlled via a LabVIEW programme. Prior to pressure sensor characterisation, set-up was calibrated using using a load cell (RS 414 0843). Further, the sensor was biased using KeySight USB modular source measurement unit (SMU-U2722A). The biasing condition of the pressure sensor is depicted in Figure 7.4.

Results and Discussion

The sensor performance was evaluated under an application of varying magnitude of pressure at a bias voltage,V_{ds} of 100 mV. The underlying pressure sensing mechanism of the PZT based pressure sensor is illustrated in Figure 7.5 and can be described as follows: The application of force to piezoelectric transducer layer results in the net dipole moment within the material due to the non-centrosymmetric nature of PZT, resulting in generation of piezopotential. The generated piezopotential is applied as the gate bias to GFET, thereby leading to the modulation of drain current. The relationship between the generated charge and applied force is approximated by the Equation 7.1

$$Q = d_{33}F \tag{7.1}$$

where Q is the generated charge, d_{33} is the piezoelectric coefficient and F is the applied force. As observed from Equation 7.1 the charge generated exhibits a linear relationship with the applied force, therefore the generated piezopotential is directly dependent on the applied force. Increasing magnitude of force results in larger piezopotential, leading to a larger modulation of drain current of the device. Figure 7.6a shows the piezopotential generated by the extended gate for varying pressure. The application of pressure to PZT MIM structure, generates a positive piezopotential which acts as a gate bias to GFET. The positive piezopotential applied results in repulsion of the majority

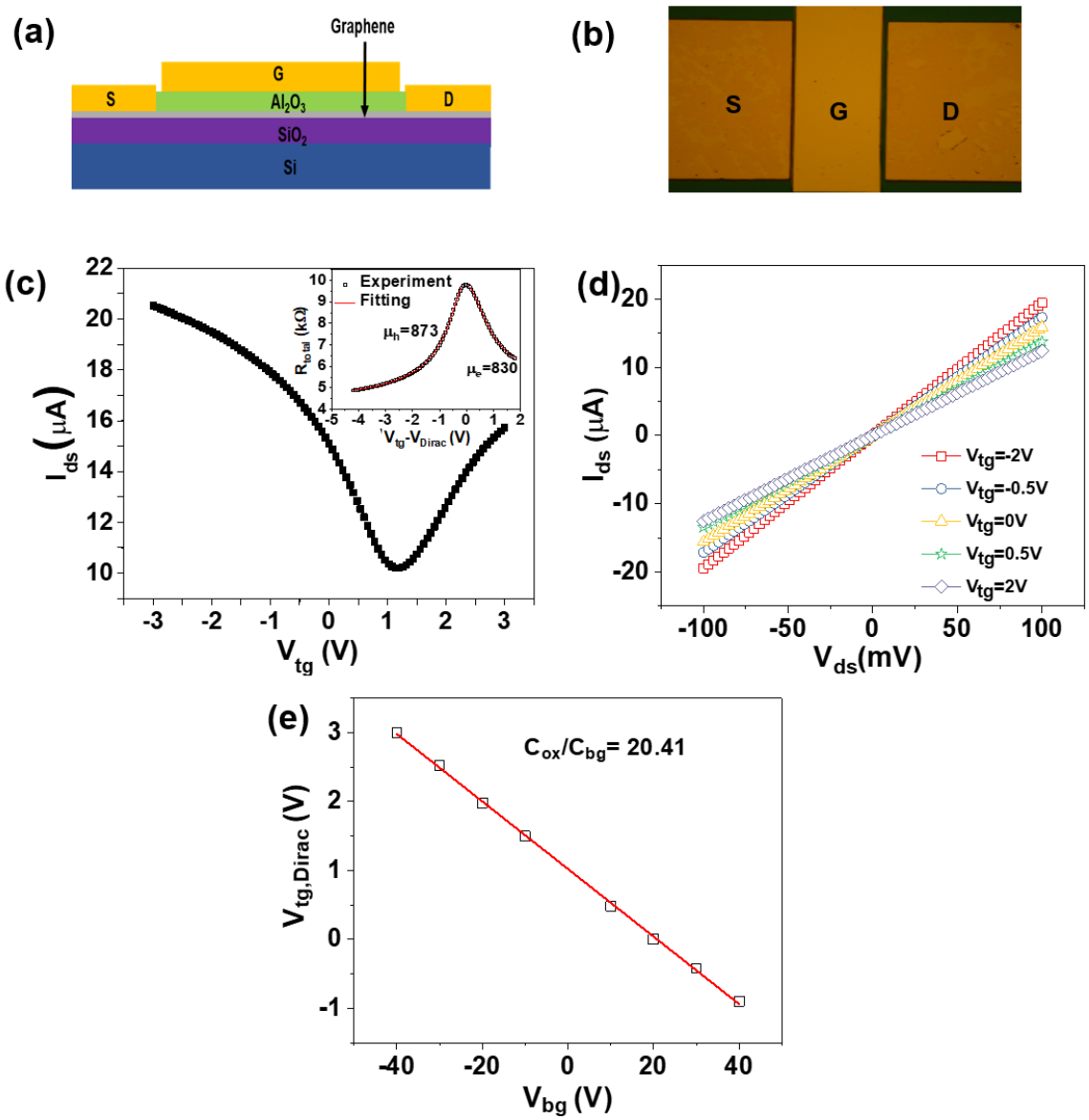

Figure 7.3: Electrical characterisation of GFET (a) Cross-sectional schematic representation of GFET. (b) Optical micrograph of top-gate GFET. (b)Transfer characteristics of GFET at V_{ds}=100 mV. The inset shows the total device resistance at V_{ds}=100 mV with respect to Dirac voltage and equation fit (solid red line)for R_s of 4.77 kΩ for hole branch and 4.47 kΩ for electron branch. (c)Output characteristics of GFET for different top-gate voltage (d) Top-gate Dirac point voltage to varying back-gate voltage, V_{bg}, of GFET [56]

charge carriers (holes) at this biasing condition, resulting in decrease in drain current of GFET. The release event results in the graphene channel regaining its previous carrier density and the drain current returning to its original value. The dynamic response of the sensor to varying magnitude of force is shown in Figure 7.6b. The investigated pressure regime is associated with touch event and object manipulation.

The sensitivity, S, of the pressure sensors is defined as change in the ratio drain current of GFET and is given by $S = ((\Delta I/I_0)/\Delta P)$ where ΔP is the applied pressure. The sensor exhibited a sensitivity of $4.55 \times 10^{-3}\text{kPa}^{-1}$ with linear response for investigated pressure range, as shown in Figure 7.7.

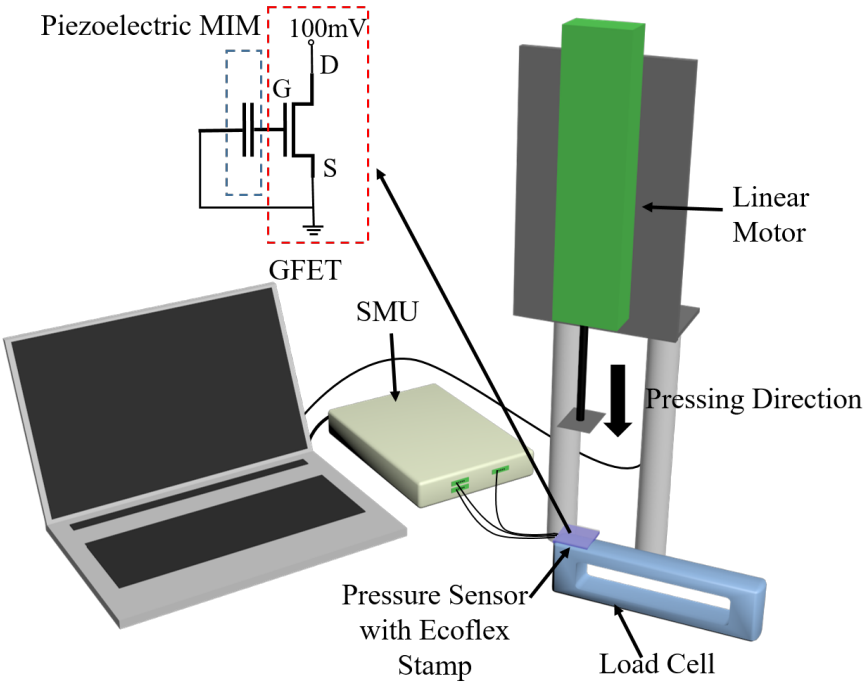

Figure 7.4: Schematic of pressure sensing characterisation set-up. The system comprises the Linear stage motor and Load cell controlled via Labview programme. The biasing condition of the sensor during the pressure sensing characterisation is also shown [215].

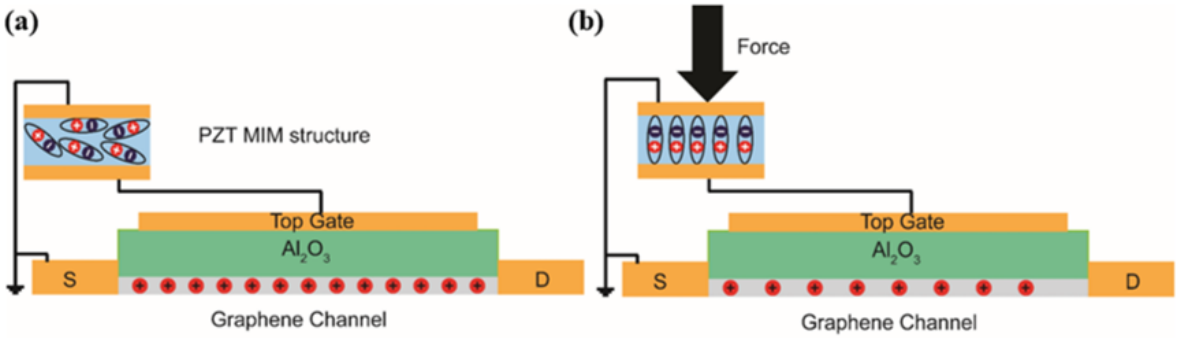

Figure 7.5: Scheme of depicting the underlying sensing principle of the sensor (a) In absence of any force application. (b)Application of force results net dipole moments within the PZT MIM structure, leading to piezopotential generation applied as the gate bias to GFET, like charge carriers are repulsed leading to change in the drain current [56].

Further, the sensor performance with respect to state-of-art pressure sensors is summarised in Table 7.1. Long term stability of the sensor under constant loading and unloading is another key performance metric of the sensor for real world applications. The sensor stability was evaluated by performing the switching cyclic test under a pressure of 94.18 kPa. The sensor exhibited good stability, with no noticeable degradation in the sensor performance over 400 cycles, as shown in Figure 7.8.

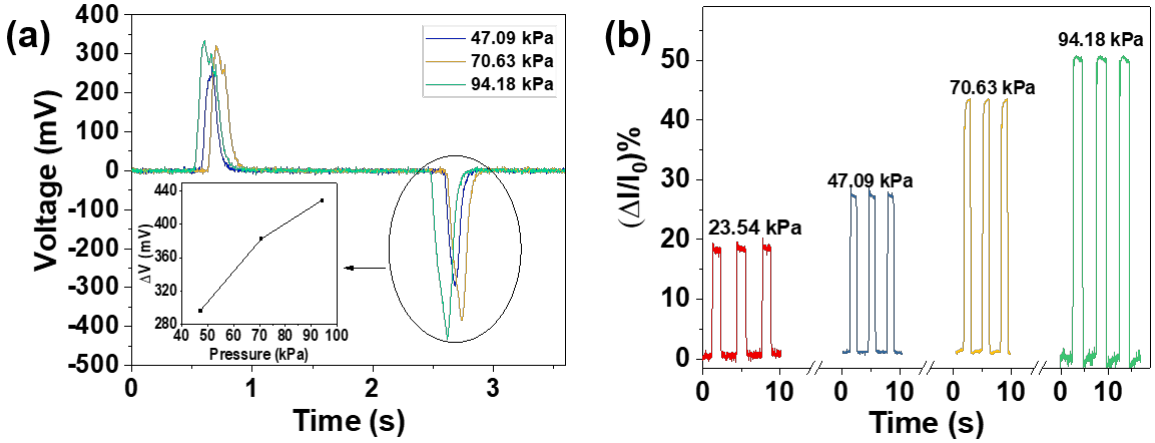

Figure 7.6: (a) Response of piezoelectric MIM structure under varying magnitude of pressure, inset shows the generated piezopotential. (b) The response of the pressure sensor for different applied magnitude pressure [56].

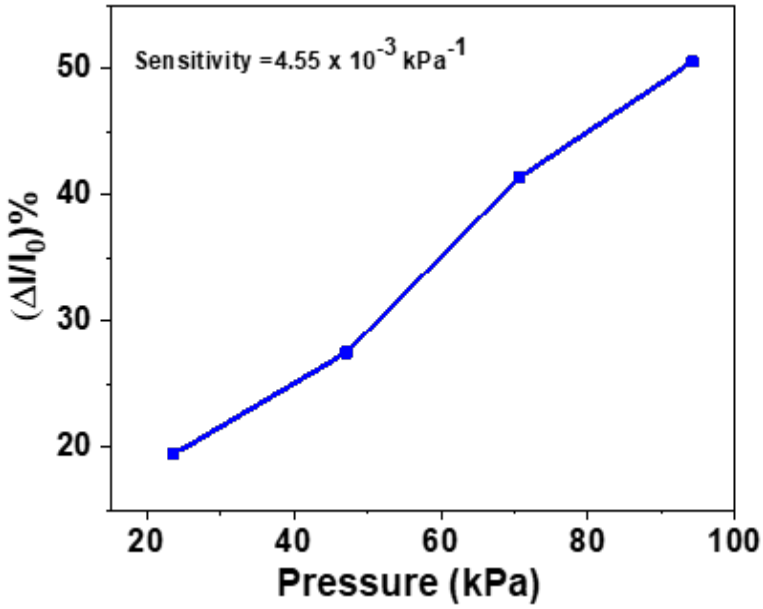

Figure 7.7: Normalized change in the drain current of GFET vs pressure [56].

Parameters	Organic FET (DNTT)	Silicon FET	GFET	GFET (This work)
Sensitivity (GPa^{-1})	1.96	6.12	205	4550
Operating Voltage (V)	$V_{ds} = V_{gs}$=-2	$V_{ds} = V_{gs}$=5	V_{ds}=0.1 V_{gs}=25	V_{ds}=0.1 V_{gs}=0
Mobility (cm^2/V.s)	0.56	696	μ_h= 212,μ_e= 96	μ_h= 879,μ_e=828
Pressure regime (kPa)	0-320	0-5550	0.250-3000	0-94.18

Table 7.1: Comparison of key performance indicators of reported pressure sensors.

7.2.2 Aluminium Nitride (AlN)

Aluminium nitride, III-V nitride of closely packed wurtzite structure, is another attractive piezoelectric material investigated as a transducer layer for pressure sensing applications. Though AlN exhibits a low piezoelectric constant in comparison to PZT, the ability to deposit high quality AlN film via a low temperature CMOS compatible process is an attractive feature for flexible electronic applications. Similar to PZT, AlN

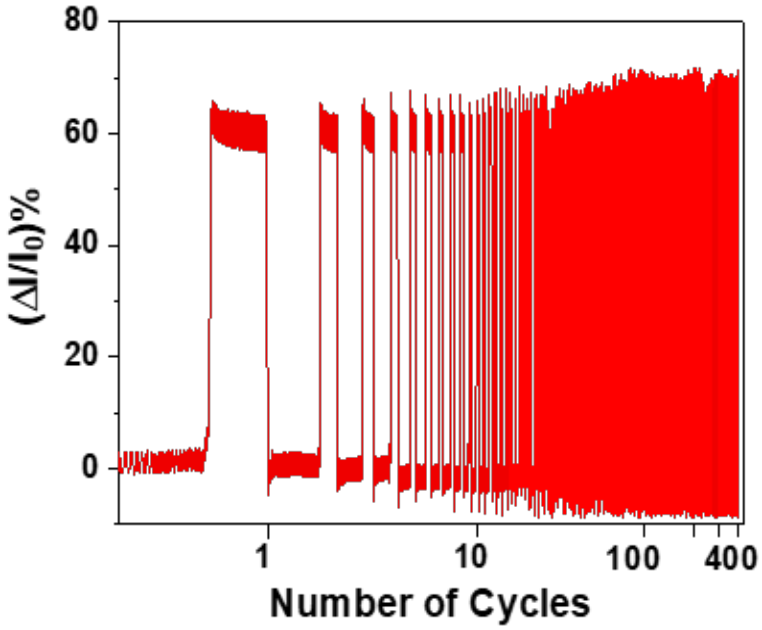

Figure 7.8: Switching cyclic measurement of the sensor over 400 cycles for pressure of 94.18 kPa. The sensor exhibited a stable performance with no noticeable change in the sensor response [56].

as a piezoelectric transducer layer was investigated in an extended gate configuration for tactile sensing applications.

The AlN MIM structure for the extended gate configuration was fabricated by adopting a low temperature CMOS compatible process. A 500 nm thick AlN was deposited by reactive RF magnetron sputtering on top of 100 nm Al deposited on PI substrate. The sputtering was carried out in N_2 (40 sccm) and Ar (20 sccm) atmosphere using the Al as target under a pressure of 3 mTorr and 700 W RF power. Prior to deposition of AlN on the substrate, pre-sputtering was carried out for 5 mins with a closed shutter. Finally, MIM structre was realised by the deposition of the top electrode (NiCr/Au- 20 nm/ 100 nm) via e-beam evaporation using a hard mask. Post sputtering the crystalline structure of the film was studied by XRD. The XRD scan of sputtered AlN film is depicted in Figure 7.9. The sputtered film exhibited the strong peak related (0002) orientation at $2\theta = 36.03^{o}$ responsible for the piezoelectric property of film. In addition, peaks associated with $(10\bar{1}0)$ and $(10\bar{1}1)$ orientation can also be observed at $2\theta = 33.3^{o}$ and 37.9^{o} respectively. The peak observed at $2\theta = 38.4^{o}$ arises due to the bottom Al electrode of the MIM structure [200].

Electrical Characterisation of GFET

Similar to PZT based pressure sensor, AlN MIM structure was connected in an extended gate configuration to GFET with a channel length and width of 45 μm and 50 μm respectively. The electrical characteristics of GFET is shown in Figure 7.10. The carrier mobility of GFET was extracted by separate fitting of hole and electron branch using the DTM. The hole and electron mobility of the device were 868 cm^2/V.s and 718 cm^2/V.s respectively.

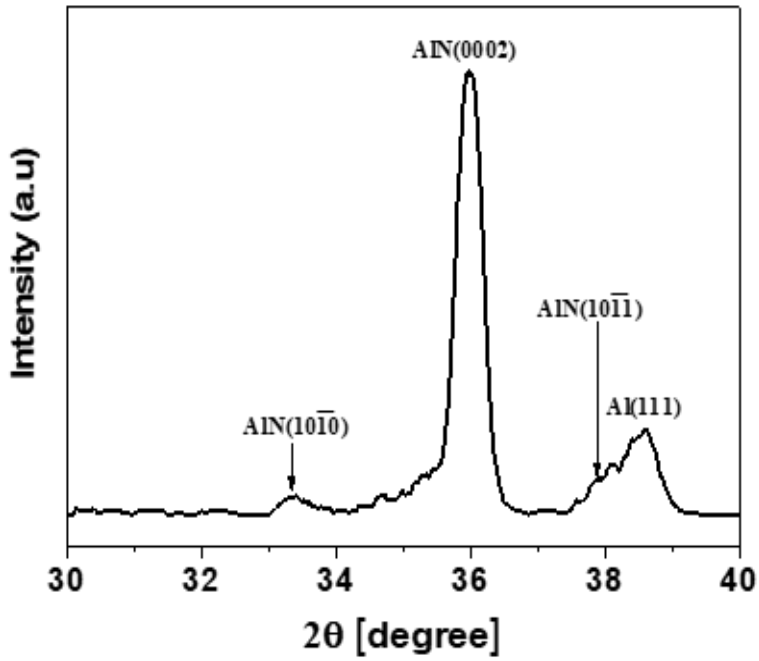

Figure 7.9: XRD scan of AlN sputtered on top of Al deposited PI subsrate [215].

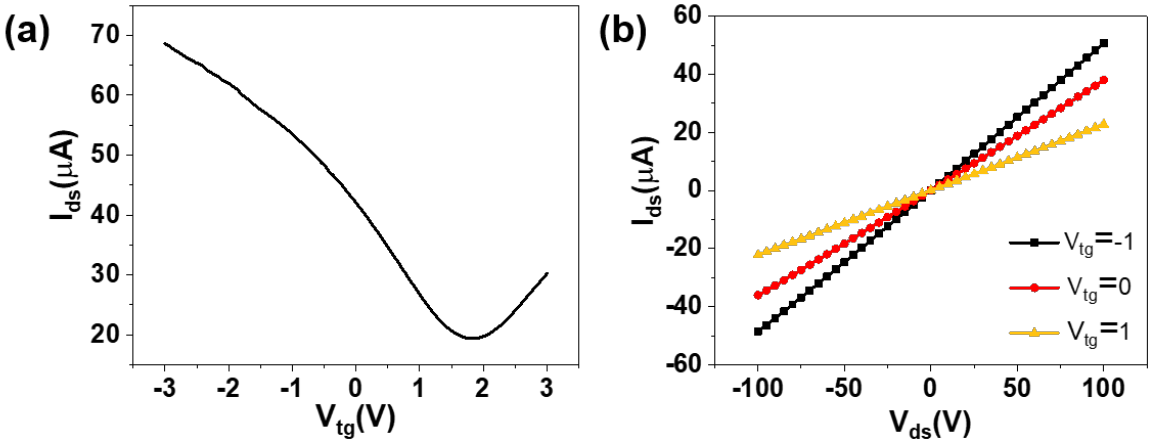

Figure 7.10: Electrical characterisitcs of GFET (a) Transfer characteristics at V_{ds}= 100 mV. (b)Output characteristic of GFET for varying top gate voltage [215].

Results and Discussion

The sensor performance was evaluated for a pressure range of the 0 kPa - 13 kPa using the above-described pressure set-up. During the sensor characterisation, the GFET was biased at V_{ds}= 100 mV. The sensor response to varying pressure is presented in Figure 7.11. For the pressure regime of 0-9.74 kPa, the sensor exhibited a sensitivity of 7.18×10^{-3} kPa^{-1} with a minimum detection limit of 0.89 kPa. The pressure regime investigated denotes pressure range associated with intra body pressure measurement. Therefore, the reported pressure sensors could find applications associated with wearable health monitoring devices where the low voltage operation is another prerequisite.

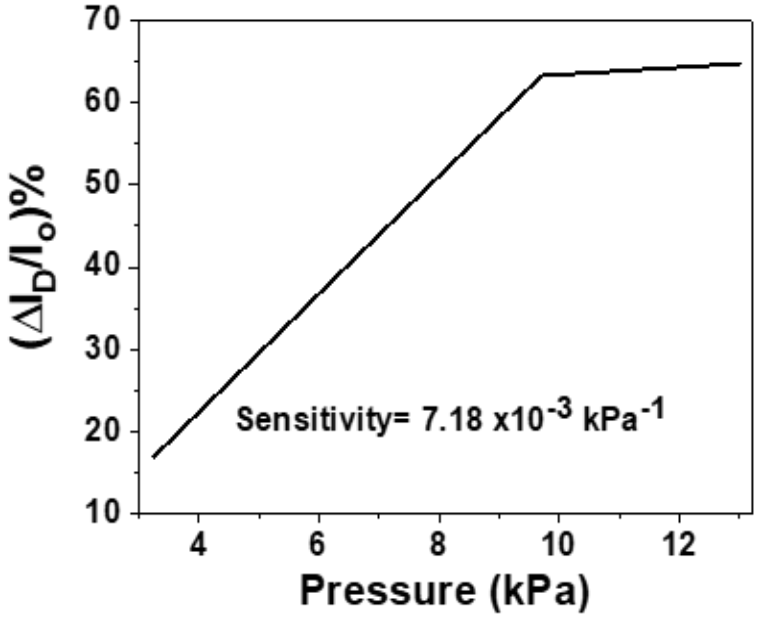

Figure 7.11: Sensitivty of the sensor for varying magnitude of pressure in the range of 3.25 -9.74 kPa [215].

7.3 Towards Development of Flexible Pressure Sensor Array

The development of tactile sensors for human skin requires the sensors to meet certain prerequisites such as high sensitivity, fast response, conformability. In this regard, development of flexible pressure sensors has become a growing area of interest. Besides e-skin, development of such sensors could also benefit future flexible electronic applications in wearable healthcare monitoring and other consumer electronic devices. The development of flexible electronics devices is often carried out on inherently flexible polymeric substrate. Polymer substrates often have low thermal budget, thereby limits, the use of any high temperature process. Therefore various other novel fabrication strategies have been adopted in the development of the large area flexible electronics. This section presents the development of flexible GFET-based pressure sensors. A low temperature CMOS compatible process was adopted for the fabrication of GFET, thereby enabling the further scaling and development on flexible substrate. Further, for the development of flexible pressure sensors, the piezoelectric transducer layer was integrated along with the top-gate dielectric stack. Figure 7.12 shows the schematic and optical microscopy image of the flexible GFET. The adopted architecture enabled higher resolution and improved signal to noise ratio.

7.3.1 Methods and Methodology.

The spin-on PI (HD Microsystems PI 2524) was used as the substrate for the development of flexible GFET-based pressure sensors. The PI was spin-coated on to glass wafer, which served as the temporary supporting substrate during the device

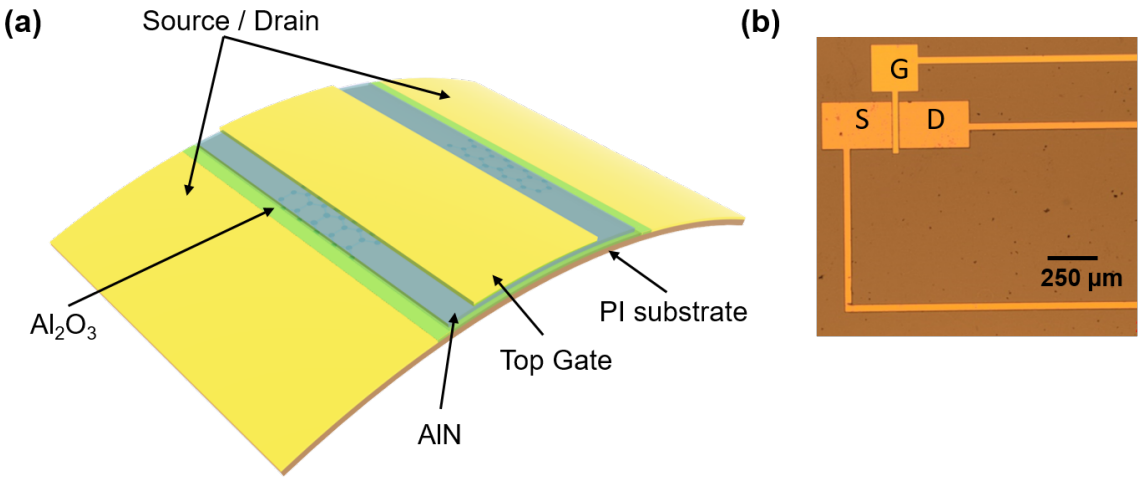

Figure 7.12: (a)Scheme of flexible pressure sensors with piezoelectric transducer layer integrated within the dielectric stack. (b)Optical microscopy image of flexible GFET based pressure sensor on the PI substrate.

fabrication process. The glass was used as a temporary supporting substrate due to its poor adhesion with PI film, hence aiding in facile removal from the carrier substrate post device fabrication. To retain a good adhesion between PI and glass during the fabrication process the adhesion promoter VM 651 was used on the edges of the glass substrate. An in-depth details of the substrate preparation for the development of the flexible pressure sensors is provided in Chapter 3. Post preparation of the substrate, a similar fabrication process to that described above was adopted for the development of devices, with slight modifications carried out in order to integrate the piezoelectric AlN transducer layer within the gate dielectric stack. Post ALD of Al_2O_3, 90 nm of AlN was RF-sputtered at the following optimised conditions : RF power- 500W; sputtering pressure-5 mTorr; N_2 : Ar flow ratio-1.6:1. Finally, top-gate electrode was defined via metallisation and lift-off. Post completion of the device fabrication, the PI film was detached from the glass carrier wafer using a PDMS stamp assisted transfer to a commercially available Kapton film. The transferred PI film with the completed device is shown in Figure 7.13.

7.3.2 Results and Discussion

Dielectric Stack characterisation

Figure 7.14a shows the cross-sectional image of the sputtered AlN film on the Al_2O_3. The sputtered film exhibited a columnar growth characteristics of (0002) oriented AlN film. Though the film was deposited using the optimised recipe reported in Chapter 5, the crystal orientation of the film is strongly influenced by the underlying substrate. Therefore, to evaluate the influence of the underlying ALD Al_2O_3 on the crystal orientation of sputtered AlN film, a XRD scan was performed. The XRD scans of the ALD Al_2O_3 and dielectric stack of AlN/ALDAl_2O_3 films are shown in Figure 7.14b. As observed from Figure 7.14b, in addition to the AlN (0002) orientation peak at 36.0^o an

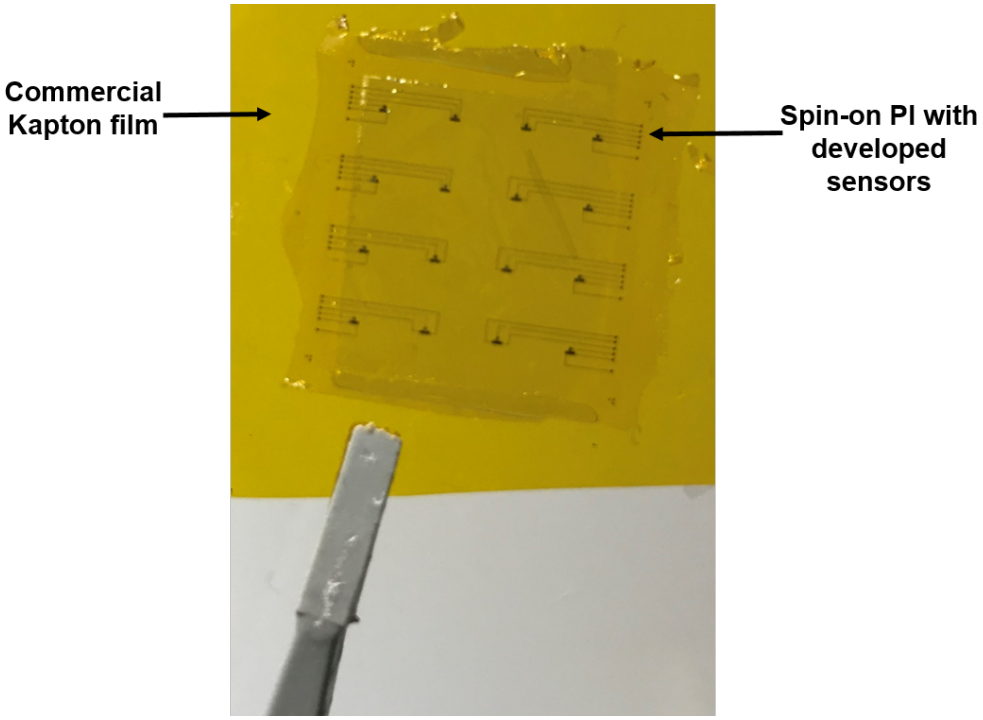

Figure 7.13: Photograph of transferred spin-on PI with sensors to a 20 μm thick Kapton film. Post completion of fabrication of the sensor, the spin-on PI film with the devices was transferred to a Kapton film using a PDMS stamp assisted transfer process.

additional peak is observed at $2\theta = 33.2^o$ corresponding to the AlN$(10\bar{1}0)$ orientation. The presence of additional peaks associated with other crystal orientation can have a detrimental effect on the sputtered AlN film. AFM scan of ALD Al_2O_3 and AlN film sputtered on Al_2O_3 is shown in Figure 7.14c and d, with roughness of 0.77 nm and 1.17 nm respectively. The piezoelectric constant of AlN sputtered on Al_2O_3, was determined using d_{33} meter. Two different thickness of AlN film was deposited and their respective piezoelectric coefficient shown in Figure 7.15. The 90 nm AlN film on Al_2O_3 exhibited a higher piezoelectric coefficient and therefore was used as optimal thickness for AlN within the dielectric stack.

7.3.3 Electrical characterisation

The transfer and output characteristics of GFET comprising 90 nm AlN/15 nm of Al_2O_3 top-gate dielectric stack is shown in Figure 7.16. The devices exhibited a typical electrical characteristics of GFET. As observed in Figure 7.16a , devices exhibited a good gate control with a low gate leakage current. However, it should be noted that during the double sweep of gate voltage a larger hysteresis ($\approx$ 1.20 V) was observed in comparison to GFET with Al_2O_3 as the gate dielectric, indicating the presence of trap charges within the top gate dielectric stack and graphene. The estimated capacitance of top-gate dielectric stack is 94.3 nF/cm^2, determined from a MIM structure. The extracted average hole and electron mobility GFETs were 1567.54 cm^2/V.s and 1612.47 cm^2/V.s respectively. Further, the effect of mechanical bending on electrical performance of the device was evaluated under a 30 mm bending radius.

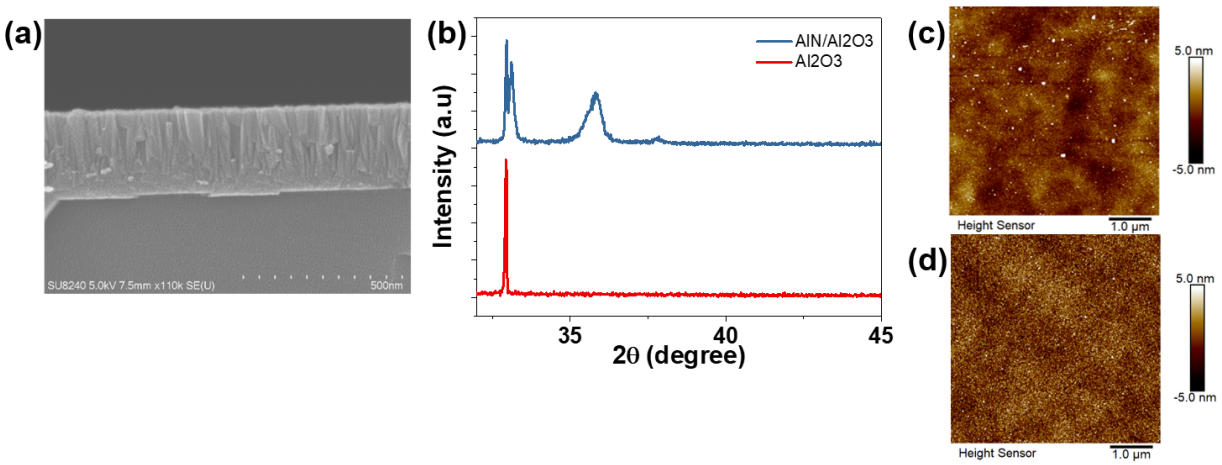

Figure 7.14: Characterisation of the dielectric stack (a) Cross-sectional SEM image of AlN sputtered on ALD Al_2O_3. (b) XRD scan of ALD Al_2O_3 (bottom XRD scan) and AlN/ ALD Al_2O_3 (top XRD scan)dielectric stack. The deposition of AlN film on Al_2O_3 resulted in an additional peak observed associated with AlN $(10\bar{1}0)$ orientation. (c) AFM scan of ALD Al_2O_3 (R_a=0.77 nm) (d) AFM scan of AlN/ALD Al_2O_3 with (R_a=1.17 nm)

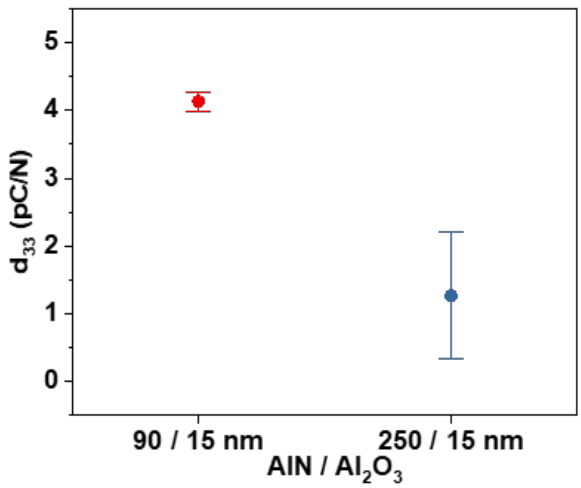

Figure 7.15: Average d_{33} coefficient of the AlN/Al_2O_3 stack with varying AlN thickness of 90 nm and 250 nm. The average piezoelectric coefficient of 90 nm/15 nm of AlN/Al_2O_3 stack is 4.13 and while 250 nm/ 15nm of AlN/Al_2O_3 dielectric stack exhibited an average piezoelectric coefficient of 1.26

The device exhibited a stable performance under a bending condition. The increase in the drain current in the hole branch of the device could be due to piezopotential generated under the mechanical strain and due to mechanical anomaly. Therefore, a further analysis is required to understand the bending effect.

The GFET based pressure sensor comprising of AlN/Al_2O_3 dielectric stack was developed on a spin-on PI substrate. The spin-PI substrate with the sensors was transferred onto a commercial Kapton film (Figure 7.13) using a PDMS stamp assisted process. The film was subsequently bonded on to flexible PCB using the low-stress epoxy for electro-mechanical characterisation of the sensors. Subsequently, for electrical connections between the PCB pad and contact pad of the sensors techniques such as

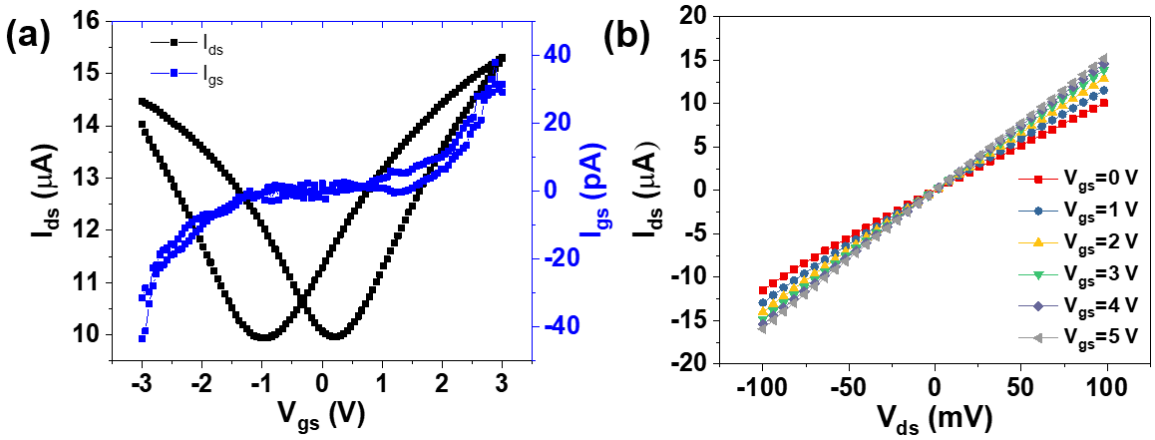

Figure 7.16: Electrical characteristics of the flexible GFET (a) Transfer characteristics of GFET at V_{ds}=100 mV. (b) Output characterisitcs of GFET under varying gate voltage.

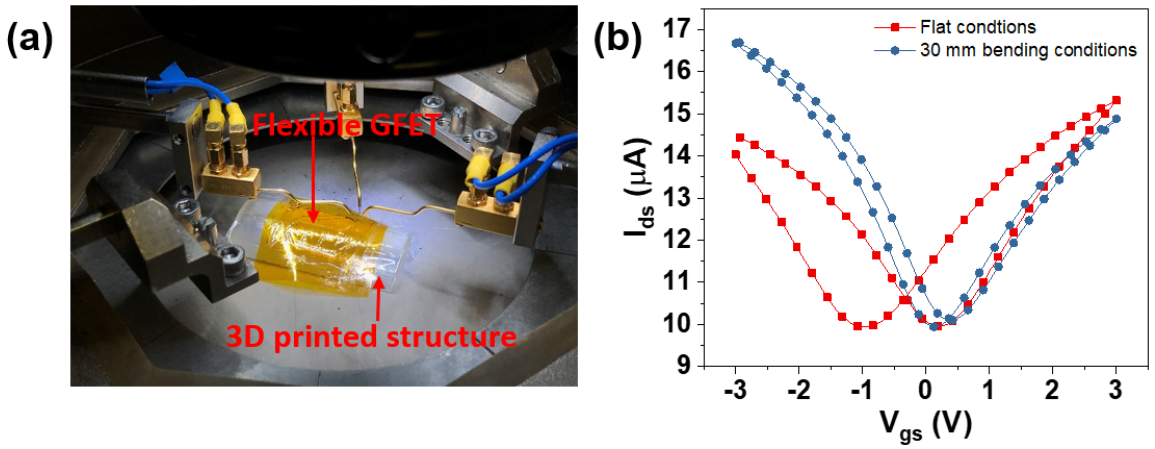

Figure 7.17: (a) Electrical measurement set-up to evaluate the electrical performance of the GFET under bending conditions. 3D printed structure with 30 mm bending radius was used to study GFET performance under a bending conditions. (b) Electrical characteristics of GFET under flat (square) and bending(circle) conditions.

wire bonding and ink-jet printing was investigated. The attempts to make electrical connection between the PCB pads and contact pads of the sensors via wire-bonding techniques failed due to contact pads of the sensor being removed by the ultrasonic agitation of the wire-bonder. Besides, wire-bonding attempts were made to make electrical connections between the contact pads of the sensor and PCBs pads via inkjet printing of silver ink. However, the thickness difference between the spin-on PI and PCB substrate affected the electrical continuity of ink-jet printed silver ink. In this regard, screen printing is an attractive choice for printing of interconnects. Therefore attempts to print the interconnects using the stretchable silver ink via screen-printing techniques will be investigated in the future.

7.4 Chapter Summary

In summary, low voltage piezoelectric GFET-based pressure sensors have been discussed. The pressure sensor comprises two main components: GFET and piezoelectric MIM structure, which acts as pressure sensitivity layer. Two different piezoelectric materials namely PZT and AlN have been investigated as a piezoelectric material for the development of the pressure sensors. The operation mechanism of the sensor can be summarised as follows: The application of pressure to the piezoelectric transducer layer results in the generation of piezopotential. The generated piezopotential is applied as a gate bias to the GFET, resulting in the modulation of the drain current. As the magnitude of the generated piezopotential is directly dependent on the applied pressure, a higher pressure results in a larger piezopotential thereby resulting in a larger modulation of the drain current.

PZT based pressure sensor exhibits sensitivity of 4.55×10^{-3} kPa^{-1} for pressure range 0-100 kPa with an excellent stability over 400 switching cycles. Athough, PZT is an excellent piezoelectric material, the high process temperature often associated with it, and CMOS incompatibiltiy limits its use in development of CMOS compatible flexible electronics. Frequently, high voltage poling is often employed to enhance its piezoelectric property, which could could have a detrimental effect on the device.

AlN is another attractive piezoelectric material. Despite its low piezoelectric coefficient in comparison to other piezoelectric material such as P(VDF-TrFE), PZT etc. its CMOS compatibility, ability to deposit high quality film at low temperature, have made it an attractive candidate for the development of large area flexible electronic applications. Further, issues associated with poling can be evaded by the use of AlN, owing to its non-centrosymmetric crystal structure. Remarkably, the reported sensors operate at very low voltage (100 mV), which is an attractive feature for e-skin and wearable health motoring applications where low voltage devices are preferred. Further, a simpler fabrication process in comparison to Si FET and intrinsic mechanical and electrical properties of graphene would pave way towards the development of low-cost flexible pressure sensors. In addition to extended gate configuration, integration of piezoelectric material within the dielectric stack of the GFET is an attractive option, as it would enable the development of a high-resolution sensor and also aid in the improvement of signal-noise ratio of the sensor. In this regard, a preliminary work towards the development of flexible GFET-based pressure sensor has been investigated. The GFET pressure sensor was developed on a flexible spin-on PI substrate. The piezoelectric AlN transducer layer was integrated within the dielectric stack of the GFET. The preliminary electrical characterisation of GFET and influence of mechanical bending on the electrical performance of the device were studied. The sensor exhibited a typical ambipolar characteristics of GFET and stable response under bending conditions (30 mm bending radius). Further investigation is required to evaluate the sensor performance under varying magnitude of pressure. This

requires the integration of the sensors with a flexible PCB for the electromechanical characterisation. However the initial attempts to achieve electrical connections between the PCB and contact pads of the sensor via wire-bonding and ink-jet printing failed due to aforementioned reasons. In this regards, in near future screen printing will be investigated to make an electrical contact between the sensors and PCB.

Chapter 8

Conclusion and Future works

8.1 Conclusion

Recent years have witnessed rapid progress in the development of e-skin. This is primarily attributed to developments in novel materials, device architectures and smart engineering approaches to incorporate existing high performance materials for the development of flexible and strecthable sensors for e-skin application. The interest in the development of sensors for e-skin applications is driven by its potential futuristic applications in the fields of interactive robotics, smart prostheses, healthcare monitoring devices and wearable and portable devices. In this regard, various sensors such as physical sensors(for detection of mechanical stimuli such as strain, pressure etc), chemical sensors, temperature sensors have been explored. Among them the development of physical sensors has become an area of immense interest resulting in the development of sensors (discussed in Chapter 2) that rivals or surpassed the performance of human skin. However various challenges still lay ahead in terms of power efficiency, compatible large area manufacturing processes and low cost etc.

The sense of touch is one of the major functionalities of human skin which aids us in various functions such as object manipulation, texture recognition, slip detection, gripping etc. In this regard, the development of sensors for mechanical stimuli has been a primary focus in the development of e-skin. To replicate the human skin's 'sense of touch' various transduction mechanisms and device architectures have been explored resulting in significant improvements in sensor performance that even rivals the human skin. To truly emulate the human skin requires development of the large array of sensors and addressing and readout mechanisms for individual sensors are required. In this regard, FET based pressure sensors are an attractive choice owing to their high sensitivity and fast response. In addition FET would enable the development of the active matrix with minimal cross talks. This thesis presents the development of low voltage GFET based pressure sensors for tactile sensing applications. Graphene is an attractive material for the development of flexible electronics owing to its fascinating electrical and mechanical properties enabling the development of high performance flexible electronics. Recent advances in large scale synthesis of CVD

graphene (30 in) and its CMOS compatibility have led to the exploration of graphene for high performance flexible electronics. The body of work presented in this thesis consists of development and optimisation of the transfer process of CVD grown graphene, development of top-gate GFET, and process development of the piezoelectric transducer layer for pressure sensing applications. The significant research outcomes of the thesis are summarised below:

- A CVD grown graphene on Cu was used as the channel material for the development of GFET. The development of GFET requires the transfer of graphene onto an insulating substrate. This was achieved using the widely adopted polymer assisted wet transfer of graphene. The quality of graphene is generally affected during the wet transfer process due to polymeric residues, tears, wrinkles etc. Therefore, it is critical to optimise the transfer process to achieve high quality graphene devices. In this regard, three polymers- PMMA, PC and CAB- were investigated as the supporting polymer during graphene transfer. A systematic study was performed on graphene transferred with different polymers to understand the impact of the polymer on transferred graphene. Raman spectroscopy, AFM and electrical characterisation of GFET were carried out to understand the impact of the polymers on graphene. The results of these studies are presented in Chapter 4. Among the different polymers investigated, CAB was preferred as it exhibited the lowest strain ($\epsilon \approx 0.045\%$) and doping on transferred graphene samples. Therefore,in the subsequent studies CAB assisted wet transfer was adopted for the graphene transfer.

- Top-gate GFET is one of the components of the pressure sensor. Development of top-gate GFET requires a uniform deposition of high quality top-gate dielectric. A low temperature thermal ALD process was adopted for deposition of high quality Al_2O_3 as top gate dielectric. The direct deposition of ALD on graphene is a challenging process due to its chemical inertness often resulting in a poor film. Prior to ALD deposition, a thin layer of Al (3 nm) was deposited via e-beam evaporation which served as the nucleation layer for the subsequent ALD process. The use of Al as the seed layer promoted a growth of high quality ALD film with surface roughness of 0.79 nm and dielectric constant (ε_r) of 7.46. The results of this study is presented in Chapter 5. Subsequently, the top-gate electrode was defined by photolithography, metallisation and lift-off. The results of electrical characterisation of top-gate GFET is discussed in Chapter 5. The fabricated top-gate GFET demonstrated an excellent gate control with average hole and electron mobility of 1222 cm^2/V.s and 1339 cm^2/V.s respectively. Notably, a low temperature CMOS compatible process was adopted for the fabrication of the device. Therefore this process could be directly adopted for the development of flexible electronics.

- A GFET based pressure sensor has been explored for tactile sensing

applications. The pressure sensor comprises of top-gate GFET in an extended gate configuration with a piezoelectric transducer layer. Namely two main piezoelectric materials PZT and AlN have been explored as a piezoelectric transducer layer for the pressure sensor. The PZT based pressure sensor exhibited a linear sensitivity of 4.55×10^{-3} kPa^{-1} for a pressure range of 0-100 kPa corresponding to the pressure range associated with touch events and object manipulation. Despite its high piezoelectric constant and high processing temperature, CMOS incompatibility, high voltage poling requirement are some of the drawback of PZTs. The aforementioned issues associated with PZT could be mitigated via the use of AlN. In this regard, low temperature RF magnetron sputtering has been explored for the deposition of piezoelectric AlN films. The piezoelectric property of AlN is strongly influenced by its c-axis crystal orientations. c-axis orientation of the film is strongly influenced by the sputtering conditions such as sputtering pressure, RF power, gas flow ratio etc. Therefore, a detailed study was performed to understand the impact of the sputtering conditions on AlN's c-axis orientations. The influence of sputtering conditions on the crystal orientation of the film was studied by evaluating the XRD scan of the AlN samples sputtered at different conditions. The results of the process optimisation for achieving highly c-axis oriented films is presented in Chapter 5. The pressure sensor with AlN as the piezoelectric transducer layer exhibited a linear response in pressure range upto 10 kPa with a sensitivity of 7.18×10^{-3} kPa^{-1}. This pressure range is ideal for applications associated with intra body pressure measurements and object manipulation. One of the stand out features of the developed pressure sensor is its low operation voltage (100 mV) which is an attractive feature for large area e-skin and wearable applications. It should be noted the biasing condition could also be further be reduced for extremely low voltage operation of the sensor.

- Development of flexible pressure sensors is an attractive choice for e-skin applications as it would enable conformable attachment to curvilinear surfaces. In this regard, top-gate GFET with a piezoelectric layer integrated within the dielectric stack of the device has been explored. Further, integration of the piezoelectric material within the top gate dielectric stack would enable the development of high resolution sensors with an improved signal to noise ratio in comparison to the extended gate approach. In this regard, top gate flexible GFET comprising of RF sputtered AlN deposited on top of ALD Al_2O_3 has been explored as a gate dielectric for FET based pressure sensors. The developed flexible GFET (with dielectric stack) showed a good gate control with an average hole and electron mobility of 1568 $cm^2/V.s$ and 1612 $cm^2/V.s$ respectively. Further, the device exhibited a good electrical stability under mechanical bending, showing its promise in e-skin application. However, the pressure response of the device is yet to be assessed. This requires the integration

of pressure sensors and flexible PCB. Initial attempts investigated the use of wire-bonding and inkjet printing for electrical connection between the PCB and contact pads of the sensor. However, these techniques failed due to contact pads being affected by the ultrasonic agitation of the wire-bonder or due to poor electrical continuity of inkjet printed Ag ink. Future work will explore the use of screen printer to address this issue.

8.2 Future work

The focus of the work has been on development of pressure sensors for e-skin applications. The piezoelectric GFET based pressure sensor presented in this work is an attractive choice owing to its high sensitivity, fast response and low operation voltage. The development of flexible pressure sensors are attractive as it would enable conformable attachment to non uniform surfaces and open up new avenues with respect to various applications. In this regard, a flexible GFET with a piezoelectric transducer layer integrated within the gate dielectric has been demonstrated. The results from the first batch of devices shows a stable transistor performance even under bending conditions. However, the integration of sensors for large area e-skin pressure sensing application requires addressing few shortcomings. These include:

- **Packaging**: Development of appropriate packaging is critical for the realisation of large area sensors. An appropriate packaging would :

  1. Enable easy access to individual pixels within an array
  2. Minimise wiring and ensure reliable electrical connection
  3. Enable facile integration with circuitry.

  This would be achieved in future using a flexible PCB. The interconnects between the GFET's contact pads and flexible PCB would be achieved using stretchable silver ink printed via screen printer.

- **Pressure sensor characterisation**- The current study has only focused on the electrical characterisation of GFET. The sensor response at varying magnitudes of pressure will be evaluated to determine its sensitivity, pressure regime and response time etc. In addition, the sensor response under varying bending radii, switching cycles and bending cycles would be studied to evaluate the sensor performance for large area e-skin applications.

- **Active pressure sensor matrix**- A 4 $\times$ 4 active matrix array would be developed with gate and drain electrode connected to the word and bit lines respectively and with all source electrodes of 16 transistors sharing a common ground. The active matrix response to a dynamic force would be assessed.

Bibliography

[1] A. Nathan, A. Ahnood, M. T. Cole, S. Lee, Y. Suzuki, P. Hiralal, F. Bonaccorso, T. Hasan, L. Garcia-Gancedo, A. Dyadyusha, S. Haque, P. Andrew, S. Hofmann, J. Moultrie, D. Chu, A. J. Flewitt, A. C. Ferrari, M. J. Kelly, J. Robertson, G. A. J. Amaratunga, and W. I. Milne, "Flexible electronics: The next ubiquitous platform," *P. IEEE*, vol. 100, pp. 1486–1517, 2012.

[2] J. A. Rogers, T. Someya, and Y. Huang, "Materials and mechanics for stretchable electronics," *Science*, vol. 327, no. 5973, pp. 1603–1607, 2010.

[3] T. Sekitani, U. Zschieschang, H. Klauk, and T. Someya, "Flexible organic transistors and circuits with extreme bending stability," *Nat. Mater.*, vol. 9, p. 1015, 2010.

[4] S. R. Forrest and M. E. Thompson, "Introduction: organic electronics and optoelectronics," *Chem. Rev.*, vol. 107, no. 4, pp. 923–925, 2007.

[5] C. Dimitrakopoulos and P. Malenfant, "Organic thin film transistors for large area electronics," *Adv. Mater.*, vol. 14, no. 2, pp. 99–117, 2002.

[6] S. Ju, A. Facchetti, Y. Xuan, J. Liu, F. Ishikawa, P. Ye, C. Zhou, T. J. Marks, and D. B. Janes, "Fabrication of fully transparent nanowire transistors for transparent and flexible electronics," *Nat. Nanotechnol.*, vol. 2, p. 378, 2007.

[7] M. C. McAlpine, R. S. Friedman, and C. M. Lieber, "High-performance nanowire electronics and photonics and nanoscale patterning on flexible plastic substrates," *P. IEEE*, vol. 93, no. 7, pp. 1357–1363, 2005.

[8] H. Zhou, J.-H. Seo, D. M. Paskiewicz, Y. Zhu, G. K. Celler, P. M. Voyles, W. Zhou, M. G. Lagally, and Z. Ma, "Fast flexible electronics with strained silicon nanomembranes," *Sci. Rep.*, vol. 3, p. 1291, 2013.

[9] L. Sun, G. Qin, J.-H. Seo, G. K. Celler, W. Zhou, and Z. Ma, "12-ghz thin-film transistors on transferrable silicon nanomembranes for high-performance flexible electronics," *Small*, vol. 6, no. 22, pp. 2553–2557, 2010.

[10] P. Avouris, Z. Chen, and V. Perebeinos, "Carbon-based electronics," *Nat. Nanotechnol.*, vol. 2, p. 605, 2007.

[11] G. Gruner, "Carbon nanotube films for transparent and plastic electronics," *J. Mater. Chem.*, vol. 16, no. 35, pp. 3533–3539, 2006.

[12] K. S. Novoselov, V. I. Falko, L. Colombo, P. R. Gellert, M. G. Schwab, and K. Kim, "A roadmap for graphene," *Nature*, vol. 490, p. 192, 2012.

[13] S. Bae, H. Kim, Y. Lee, X. Xu, J.-S. Park, Y. Zheng, J. Balakrishnan, T. Lei, H. Ri Kim, Y. I. Song, Y.-J. Kim, K. S. Kim, B. zyilmaz, J.-H. Ahn, B. H. Hong, and S. Iijima, "Roll-to-roll production of 30-inch graphene films for transparent electrodes," *Nat. Nanotechnol.*, vol. 5, p. 574, 2010.

[14] J. Ryu, Y. Kim, D. Won, N. Kim, J. S. Park, E.-K. Lee, D. Cho, S.-P. Cho, S. J. Kim, G. H. Ryu, H.-A. S. Shin, Z. Lee, B. H. Hong, and S. Cho, "Fast synthesis of high-performance graphene films by hydrogen-free rapid thermal chemical vapor deposition," *ACS Nano*, vol. 8, no. 1, pp. 950–956, 2014.

[15] Y. Hernandez, V. Nicolosi, M. Lotya, F. M. Blighe, Z. Sun, S. De, I. T. McGovern, B. Holland, M. Byrne, Y. K. Gun'Ko, J. J. Boland, P. Niraj, G. Duesberg, S. Krishnamurthy, R. Goodhue, J. Hutchison, V. Scardaci, A. C. Ferrari, and J. N. Coleman, "High-yield production of graphene by liquid-phase exfoliation of graphite," *Nat. Nanotechnol.*, vol. 3, p. 563, 2008.

[16] R. S. Dahiya, G. Metta, M. Valle, and G. Sandini, "Tactile sensingfrom humans to humanoids," *IEEE Trans. Robot.*., vol. 26, no. 1, pp. 1–20, 2010.

[17] R. S. Dahiya, P. Mittendorfer, M. Valle, G. Cheng, and V. J. Lumelsky, "Directions toward effective utilization of tactile skin: A review," *IEEE Sens. J.*, vol. 13, no. 11, pp. 4121–4138, 2013.

[18] B. T. M. Nghiem, I. C. Sando, R. B. Gillespie, B. L. McLaughlin, G. J. Gerling, N. B. Langhals, M. G. Urbanchek, and P. S. Cederna, "Providing a sense of touch to prosthetic hands," *Plast Reconstr Surg.*, vol. 135, no. 6, pp. 1652–1663, 2015.

[19] A. Chortos, J. Liu, and Z. Bao, "Pursuing prosthetic electronic skin," *Nat. Mater.*, vol. 15, p. 937, 2016.

[20] R. S. Johansson and A. B. Vallbo, "Tactile sensibility in the human hand: relative and absolute densities of four types of mechanoreceptive units in glabrous skin," *J. Physiol.*, vol. 286, pp. 283–300, 1979.

[21] G. Schwartz, B. C. K. Tee, J. Mei, A. L. Appleton, D. H. Kim, H. Wang, and Z. Bao, "Flexible polymer transistors with high pressure sensitivity for application in electronic skin and health monitoring," *Nat. Commun.*, vol. 4, p. 1859, 2013.

[22] C. G. Nunez, W. T. Navaraj, E. O. Polat, and R. Dahiya, "Energy-autonomous, flexible, and transparent tactile skin," *Adv. Funct. Mater.*, vol. 27, no. 18, p. 1606287, 2017.

[23] C. Pang, G.-Y. Lee, T.-i. Kim, S. M. Kim, H. N. Kim, S.-H. Ahn, and K.-Y. Suh, "A flexible and highly sensitive strain-gauge sensor using reversible interlocking of nanofibres," *Nat. Mater.*, vol. 11, p. 795, 2012.

[24] T. Someya, T. Sekitani, S. Iba, Y. Kato, H. Kawaguchi, and T. Sakurai, "A large-area, flexible pressure sensor matrix with organic field-effect transistors for artificial skin applications," *Proc. Natl. Acad. Sci. U.S.A*, vol. 101, no. 27, pp. 9966–9970, 2004.

[25] H. P. Saal and S. J. Bensmaia, "Biomimetic approaches to bionic touch through a peripheral nerve interface," *Neuropsychologia*, vol. 79, pp. 344–353, 2015.

[26] R. L. Klatzky and S. J. Lederman, *Touch*, vol. 4, pp. 152–178. New Jersey: Wiley, 2 ed., 2012.

[27] R. Dahiya and M. Valle, *Tactile Sensing: defintion and Classification*, pp. 13–17. Netherlands: Springer, 2013.

[28] S. Bauer, S. Bauer-Gogonea, I. Graz, M. Kaltenbrunner, C. Keplinger, and R. Schwdiauer, "25th anniversary article: A soft future: From robots and sensor skin to energy harvesters," *Adv. Mater.*, vol. 26, no. 1, pp. 149–162, 2014.

[29] J. Engel, J. Chen, Z. Fan, and C. Liu, "Polymer micromachined multimodal tactile sensors," *Sens. Actuator A-Phys.*, vol. 117, no. 1, pp. 50–61, 2005.

[30] M. L. Hammock, A. Chortos, B. C.-K. Tee, J. B.-H. Tok, and Z. Bao, "25th anniversary article: The evolution of electronic skin (e-skin): A brief history, design considerations, and recent progress," *Advanced Materials*, vol. 25, no. 42, pp. 5997–6038, 2013.

[31] B. C. K. Tee, C. Wang, R. Allen, and Z. Bao, "An electrically and mechanically self-healing composite with pressure- and flexion-sensitive properties for electronic skin applications," *Nat. Nanotechnol.*, vol. 7, pp. 825–832, 2012.

[32] F.-R. Fan, L. Lin, G. Zhu, W. Wu, R. Zhang, and Z. L. Wang, "Transparent triboelectric nanogenerators and self-powered pressure sensors based on micropatterned plastic films," *Nano Lett.*, vol. 12, no. 6, pp. 3109–3114, 2012.

[33] L. Lin, Y. Xie, S. Wang, W. Wu, S. Niu, X. Wen, and Z. L. Wang, "Triboelectric active sensor array for self-powered static and dynamic pressure detection and tactile imaging," *ACS Nano*, vol. 7, no. 9, pp. 8266–8274, 2013.

[34] S. C. B. Mannsfeld, B. C. K. Tee, R. M. Stoltenberg, C. V. H. H. Chen, S. Barman, B. V. O. Muir, A. N. Sokolov, C. Reese, and Z. Bao, "Highly sensitive flexible pressure sensors with microstructured rubber dielectric layers," *Nat. Mater.*, vol. 9, p. 859, 2010.

[35] Y. Zang, F. Zhang, C.-a. Di, and D. Zhu, "Advances of flexible pressure sensors toward artificial intelligence and health care applications," *Mater. Horizons*, vol. 2, no. 2, pp. 140–156, 2015.

[36] I. Graz, M. Kaltenbrunner, C. Keplinger, R. Schwdiauer, S. Bauer, S. P. Lacour, and S. Wagner, "Flexible ferroelectret field-effect transistor for large-area sensor skins and microphones," *Appl. Phys. Lett.*, vol. 89, no. 7, p. 073501, 2006.

[37] Y. Lee, J. Park, S. Cho, Y.-E. Shin, H. Lee, J. Kim, J. Myoung, S. Cho, S. Kang, C. Baig, and H. Ko, "Flexible ferroelectric sensors with ultrahigh pressure sensitivity and linear response over exceptionally broad pressure range," *ACS Nano*, vol. 12, no. 4, pp. 4045–4054, 2018.

[38] C. Dagdeviren, Y. Su, P. Joe, R. Yona, Y. Liu, Y.-S. Kim, Y. Huang, A. R. Damadoran, J. Xia, L. W. Martin, Y. Huang, and J. A. Rogers, "Conformable amplified lead zirconate titanate sensors with enhanced piezoelectric response for cutaneous pressure monitoring," *Nat. Commun.*, vol. 5, p. 4496, 2014.

[39] X. Wang, Y. Gu, Z. Xiong, Z. Cui, and T. Zhang, "Silk-molded flexible, ultrasensitive, and highly stable electronic skin for monitoring human physiological signals," *Adv. Mater.*, vol. 26, no. 9, pp. 1336–1342, 2014.

[40] L. Pan, A. Chortos, G. Yu, Y. Wang, S. Isaacson, R. Allen, Y. Shi, R. Dauskardt, and Z. Bao, "An ultra-sensitive resistive pressure sensor based on hollow-sphere microstructure induced elasticity in conducting polymer film," *Nat. Commun.*, vol. 5, p. 3002, 2014.

[41] S. Gong, W. Schwalb, Y. Wang, Y. Chen, Y. Tang, J. Si, B. Shirinzadeh, and W. Cheng, "A wearable and highly sensitive pressure sensor with ultrathin gold nanowires," *Nat. Commun.*, vol. 5, p. 3132, 2014.

[42] N. Yogeswaran, S. Tinku, S. Khan, L. Lorenzelli, V. Vinciguerra, and R. Dahiya, "Stretchable resistive pressure sensor based on cnt-pdms nanocomposites," in *2015 11th Conference on Ph.D. Research in Microelectronics and Electronics (PRIME)*, pp. 326–329.

[43] L. Wang and Y. Li, "A review for conductive polymer piezoresistive composites and a development of a compliant pressure transducer," *IEEE Trans. Instrum. Meas.*, vol. 62, no. 2, pp. 495–502, 2013.

[44] R. S. Timsit, "Electrical contact resistance: properties of stationary interfaces," *IEEE Trans. Compon. Packag. Technol.*, vol. 22, no. 1, pp. 85–98, 1999.

[45] Q. Sun, D. H. Kim, S. S. Park, N. Y. Lee, Y. Zhang, J. H. Lee, K. Cho, and J. H. Cho, "Transparent, low-power pressure sensor matrix based on coplanar-gate graphene transistors," *Adv. Mater.*, vol. 26, no. 27, pp. 4735–4740, 2014.

[46] L. Wang, T. Ding, and P. Wang, "Thin flexible pressure sensor array based on carbon black/silicone rubber nanocomposite," *IEEE Sensors J.*, vol. 9, no. 9, pp. 1130–1135, 2009.

[47] D. Niu, W. Jiang, G. Ye, K. Wang, L. Yin, Y. Shi, B. Chen, F. Luo, and H. Liu, "Graphene-elastomer nanocomposites based flexible piezoresistive sensors for strain and pressure detection," *Mater. Res. Bull*, vol. 102, pp. 92–99, 2018.

[48] Y. Pang, H. Tian, L. Tao, Y. Li, X. Wang, N. Deng, Y. Yang, and T.-L. Ren, "Flexible, highly sensitive, and wearable pressure and strain sensors with graphene porous network structure," *ACS Appl. Mater. Interfaces*, vol. 8, no. 40, pp. 26458–26462, 2016.

[49] R. Iglio, S. Mariani, V. Robbiano, L. Strambini, and G. Barillaro, "Flexible polydimethylsiloxane foams decorated with multiwalled carbon nanotubes enable unprecedented detection of ultralow strain and pressure coupled with a large working range," *ACS Appl. Mater. Interfaces*, vol. 10, no. 16, pp. 13877–13885, 2018.

[50] V. Maheshwari and R. F. Saraf, "High-resolution thin-film device to sense texture by touch," *Science*, vol. 312, no. 5779, pp. 1501–1504, 2006.

[51] S. Khan, S. Tinku, L. Lorenzelli, and R. S. Dahiya, "Flexible tactile sensors using screen-printed p(vdf-trfe) and mwcnt/pdms composites," *IEEE SENS J*, vol. 15, no. 6, pp. 3146–3155, 2015.

[52] D. J. Lipomi, M. Vosgueritchian, B. C. K. Tee, S. L. Hellstrom, J. A. Lee, C. H. Fox, and Z. Bao, "Skin-like pressure and strain sensors based on transparent elastic films of carbon nanotubes," *Nat. Nanotechnol*, vol. 6, p. 788, 2011.

[53] D. J. Lipomi, J. A. Lee, M. Vosgueritchian, B. C. K. Tee, J. A. Bolander, and Z. Bao, "Electronic properties of transparent conductive films of pedot:pss on stretchable substrates," *Chem. Mater*, vol. 24, no. 2, pp. 373–382, 2012.

[54] H.-K. Lee, J. Chung, S.-I. Chang, and E. Yoon, "Real-time measurement of the three-axis contact force distribution using a flexible capacitive polymer tactile sensor," *J. Micromec. Microeng*, vol. 21, no. 3, p. 035010, 2011.

[55] Z. Chen, Z. Wang, X. Li, Y. Lin, N. Luo, M. Long, N. Zhao, and J.-B. Xu, "Flexible piezoelectric-induced pressure sensors for static measurements based on nanowires/graphene heterostructures," *ACS Nano*, vol. 11, no. 5, pp. 4507–4513, 2017.

[56] N. Yogeswaran, W. T. Navaraj, S. Gupta, F. Liu, V. Vinciguerra, L. Lorenzelli, and R. Dahiya, "Piezoelectric graphene field effect transistor pressure sensors for tactile sensing," *Appl. Phys. Lett*, vol. 113, no. 1, p. 014102, 2018.

[57] W. Wu, X. Wen, and Z. L. Wang, "Taxel-addressable matrix of vertical-nanowire piezotronic transistors for active and adaptive tactile imaging," *Science*, vol. 340, no. 6135, pp. 952–957, 2013.

[58] R. S. Dahiya, G. Metta, M. Valle, A. Adami, and L. Lorenzelli, "Piezoelectric oxide semiconductor field effect transistor touch sensing devices," *Appl. Phys. Lett*, vol. 95, no. 3, p. 034105, 2009.

[59] S. Gao, X. Wu, H. Ma, J. Robertson, and A. Nathan, "Ultrathin multifunctional graphene-pvdf layers for multidimensional touch interactivity for flexible displays," *ACS Appl. Mater. Interfaces*, vol. 9, no. 22, pp. 18410–18416, 2017.

[60] L. Persano, C. Dagdeviren, Y. Su, Y. Zhang, S. Girardo, D. Pisignano, Y. Huang, and J. A. Rogers, "High performance piezoelectric devices based on aligned arrays of nanofibers of poly(vinylidenefluoride-co-trifluoroethylene)," *Nat. Commun.*, vol. 4, p. 1633, 2013.

[61] Q. Sun, W. Seung, B. J. Kim, S. Seo, S.-W. Kim, and J. H. Cho, "Active matrix electronic skin strain sensor based on piezopotential-powered graphene transistors," *Adv. Mater.*, vol. 27, no. 22, pp. 3411–3417, 2015.

[62] Z. L. Wang, "From nanogenerators to piezotronicsa decade-long study of zno nanostructures," *MRS Bull*, vol. 37, no. 9, pp. 814–827, 2012.

[63] Z. Wang, Y. Zhang, S. Yang, Y. Hu, S. Wang, H. Gu, Y. Wang, H. L. W. Chan, and J. Wang, "(k,na)nbo3 nanofiber-based self-powered sensors for accurate detection of dynamic strain," *ACS Appl. Mater. Interfaces*, vol. 7, no. 8, pp. 4921–4927, 2015.

[64] S. Yun, S. Park, B. Park, Y. Kim, S. K. Park, S. Nam, and K.-U. Kyung, "Polymer-waveguide-based flexible tactile sensor array for dynamic response," *Adv. Mater.*, vol. 26, no. 26, pp. 4474–4480, 2014.

[65] L. Lin, Y. Xie, S. Wang, W. Wu, S. Niu, X. Wen, and Z. L. Wang, "Triboelectric active sensor array for self-powered static and dynamic pressure detection and tactile imaging," *ACS Nano*, vol. 7, no. 9, pp. 8266–8274, 2013.

[66] W. T. Navaraj, S. Gupta, L. Lorenzelli, and R. Dahiya, "Wafer scale transfer of ultrathin silicon chips on flexible substrates for high performance bendable systems," *Adv. Electron. Mater*, vol. 4, no. 4, p. 1700277, 2018.

[67] S. Gupta, W. T. Navaraj, L. Lorenzelli, and R. Dahiya, "Ultra-thin chips for high-performance flexible electronics," *npj Flex. Elec.*, vol. 2, no. 1, p. 8, 2018.

[68] Y. Sun, W. M. Choi, H. Jiang, Y. Y. Huang, and J. A. Rogers, "Controlled buckling of semiconductor nanoribbons for stretchable electronics," *Nat. Nanotechnol*, vol. 1, p. 201, 2006.

[69] D.-Y. Khang, H. Jiang, Y. Huang, and J. A. Rogers, "A stretchable form of single-crystal silicon for high-performance electronics on rubber substrates," *Science*, vol. 311, no. 5758, pp. 208–212, 2006.

[70] D.-H. Kim, J. Song, W. M. Choi, H.-S. Kim, R.-H. Kim, Z. Liu, Y. Y. Huang, K.-C. Hwang, Y.-w. Zhang, and J. A. Rogers, "Materials and noncoplanar mesh designs for integrated circuits with linear elastic responses to extreme mechanical deformations," *Proc. Natl. Acad. Sci. U.S.A*, vol. 105, no. 48, pp. 18675–18680, 2008.

[71] S. P. Lacour, J. Jones, S. Wagner, L. Teng, and S. Zhigang, "Stretchable interconnects for elastic electronic surfaces," *Proc. IEEE*, vol. 93, no. 8, pp. 1459–1467, 2005.

[72] T. Sekitani, Y. Noguchi, K. Hata, T. Fukushima, T. Aida, and T. Someya, "A rubberlike stretchable active matrix using elastic conductors," *Science*, vol. 321, no. 5895, pp. 1468–1472, 2008.

[73] J. Kim, M. Lee, H. J. Shim, R. Ghaffari, H. R. Cho, D. Son, Y. H. Jung, M. Soh, C. Choi, S. Jung, K. Chu, D. Jeon, S.-T. Lee, J. H. Kim, S. H. Choi, T. Hyeon, and D.-H. Kim, "Stretchable silicon nanoribbon electronics for skin prosthesis," *Nat. Commun*, vol. 5, p. 5747, 2014.

[74] Y.-Y. Hsu, M. Gonzalez, F. Bossuyt, F. Axisa, J. Vanfleteren, and I. De Wolf, "The effects of encapsulation on deformation behavior and failure mechanisms of stretchable interconnects," *Thin Solid Films*, vol. 519, no. 7, pp. 2225–2234, 2011.

[75] N. Yogeswaran, W. Dang, W. T. Navaraj, D. Shakthivel, S. Khan, E. O. Polat, S. Gupta, H. Heidari, M. Kaboli, L. Lorenzelli, G. Cheng, and R. Dahiya, "New materials and advances in making electronic skin for interactive robots," *Adv. Robotics*, vol. 29, no. 21, pp. 1359–1373, 2015.

[76] H. Tian, Y. Shu, Y.-L. Cui, W.-T. Mi, Y. Yang, D. Xie, and T.-L. Ren, "Scalable fabrication of high-performance and flexible graphene strain sensors," *Nanoscale*, vol. 6, no. 2, pp. 699–705, 2014.

[77] J. Lee, T.-J. Ha, H. Li, K. N. Parrish, M. Holt, A. Dodabalapur, R. S. Ruoff, and D. Akinwande, "25 ghz embedded-gate graphene transistors with high-k dielectrics on extremely flexible plastic sheets," *ACS Nano*, vol. 7, no. 9, pp. 7744–7750, 2013.

[78] S.-H. Bae, Y. Lee, B. K. Sharma, H.-J. Lee, J.-H. Kim, and J.-H. Ahn, "Graphene-based transparent strain sensor," *Carbon*, vol. 51, pp. 236–242, 2013.

[79] S. Ryu, P. Lee, J. B. Chou, R. Xu, R. Zhao, A. J. Hart, and S.-G. Kim, "Extremely elastic wearable carbon nanotube fiber strain sensor for monitoring of human motion," *ACS Nano*, vol. 9, no. 6, pp. 5929–5936, 2015.

[80] B. Zhu, Z. Niu, H. Wang, W. R. Leow, H. Wang, Y. Li, L. Zheng, J. Wei, F. Huo, and X. Chen, "Microstructured graphene arrays for highly sensitive flexible tactile sensors," *Small*, vol. 10, no. 18, pp. 3625–3631, 2014.

[81] X. Wang, Y. Gu, Z. Xiong, Z. Cui, and T. Zhang, "Silk-molded flexible, ultrasensitive, and highly stable electronic skin for monitoring human physiological signals," *Adv. Mater.*, vol. 26, no. 9, pp. 1336–1342, 2014.

[82] L. Pan, A. Chortos, G. Yu, Y. Wang, S. Isaacson, R. Allen, Y. Shi, R. Dauskardt, and Z. Bao, "An ultra-sensitive resistive pressure sensor based on hollow-sphere microstructure induced elasticity in conducting polymer film," *Nat. Commun*, vol. 5, p. 3002, 2014.

[83] C.-L. Choong, M.-B. Shim, B.-S. Lee, S. Jeon, D.-S. Ko, T.-H. Kang, J. Bae, S. H. Lee, K.-E. Byun, J. Im, Y. J. Jeong, C. E. Park, J.-J. Park, and U.-I. Chung, "Highly stretchable resistive pressure sensors using a conductive elastomeric composite on a micropyramid array," *Adv. Mater.*, vol. 26, no. 21, pp. 3451–3458, 2014.

[84] J. Park, Y. Lee, J. Hong, Y. Lee, M. Ha, Y. Jung, H. Lim, S. Y. Kim, and H. Ko, "Tactile-direction-sensitive and stretchable electronic skins based on human-skin-inspired interlocked microstructures," *ACS Nano*, vol. 8, no. 12, pp. 12020–12029, 2014.

[85] N. Lu, C. Lu, S. Yang, and J. Rogers, "Highly sensitive skin-mountable strain gauges based entirely on elastomers," *Adv. Funct. Mater.*, vol. 22, no. 19, pp. 4044–4050, 2012.

[86] S. Jung, J. H. Kim, J. Kim, S. Choi, J. Lee, I. Park, T. Hyeon, and D.-H. Kim, "Reverse-micelle-induced porous pressure-sensitive rubber for wearable humanmachine interfaces," *Adv. Mater.*, vol. 26, no. 28, pp. 4825–4830, 2014.

[87] M. Amjadi, A. Pichitpajongkit, S. Lee, S. Ryu, and I. Park, "Highly stretchable and sensitive strain sensor based on silver nanowireelastomer nanocomposite," *ACS Nano*, vol. 8, no. 5, pp. 5154–5163, 2014.

[88] M. Kaltenbrunner, T. Sekitani, J. Reeder, T. Yokota, K. Kuribara, T. Tokuhara, M. Drack, R. Schwdiauer, I. Graz, S. Bauer-Gogonea, S. Bauer, and T. Someya, "An ultra-lightweight design for imperceptible plastic electronics," *Nature*, vol. 499, p. 458, 2013.

[89] T. Sekitani, T. Yokota, U. Zschieschang, H. Klauk, S. Bauer, K. Takeuchi, M. Takamiya, T. Sakurai, and T. Someya, "Organic nonvolatile memory transistors for flexible sensor arrays," *Science*, vol. 326, no. 5959, pp. 1516–1519, 2009.

[90] C. Wang, D. Hwang, Z. Yu, K. Takei, J. Park, T. Chen, B. Ma, and A. Javey, "User-interactive electronic skin for instantaneous pressure visualization," *Nat. Mater*, vol. 12, p. 899, 2013.

[91] K. Takei, T. Takahashi, J. C. Ho, H. Ko, A. G. Gillies, P. W. Leu, R. S. Fearing, and A. Javey, "Nanowire active-matrix circuitry for low-voltage macroscale artificial skin," *Nat. Mater.*, vol. 9, p. 821, 2010.

[92] L. Nela, J. Tang, Q. Cao, G. Tulevski, and S.-J. Han, "Large-area high-performance flexible pressure sensor with carbon nanotube active matrix for electronic skin," *Nano Lett.*, vol. 18, no. 3, pp. 2054–2059, 2018.

[93] C. Yeom, K. Chen, D. Kiriya, Z. Yu, G. Cho, and A. Javey, "Large-area compliant tactile sensors using printed carbon nanotube active-matrix backplanes," *Adv. Mater.*, vol. 27, no. 9, pp. 1561–1566, 2015.

[94] S.-H. Shin, S. Ji, S. Choi, K.-H. Pyo, B. Wan An, J. Park, J. Kim, J.-Y. Kim, K.-S. Lee, S.-Y. Kwon, J. Heo, B.-G. Park, and J.-U. Park, "Integrated arrays of air-dielectric graphene transistors as transparent active-matrix pressure sensors for wide pressure ranges," *Nat. Commun.*, vol. 8, p. 14950, 2017.

[95] Y. Zang, F. Zhang, D. Huang, X. Gao, C.-a. Di, and D. Zhu, "Flexible suspended gate organic thin-film transistors for ultra-sensitive pressure detection," *Nat. Commun.*, vol. 6, p. 6269, 2015.

[96] X. Wang, J. Zhou, J. Song, J. Liu, N. Xu, and Z. L. Wang, "Piezoelectric field effect transistor and nanoforce sensor based on a single zno nanowire," *Nano Lett.*, vol. 6, no. 12, pp. 2768–2772, 2006.

[97] K. S. Novoselov, A. K. Geim, S. V. Morozov, D. Jiang, Y. Zhang, S. V. Dubonos, I. V. Grigorieva, and A. A. Firsov, "Electric field effect in atomically thin carbon films," *Science*, vol. 306, no. 5696, pp. 666–669, 2004.

[98] Z. Yan, G. Liu, J. M. Khan, and A. A. Balandin, "Graphene quilts for thermal management of high-power gan transistors," *Nat. Commun.*, vol. 3, p. 827, 2012.

[99] I. W. Frank, D. M. Tanenbaum, A. M. v. d. Zande, and P. L. McEuen, "Mechanical properties of suspended graphene sheets," *J. Vac. Sci. Technol. B: Microelectronics and Nanometer Structures Processing, Measurement, and Phenomena*, vol. 25, no. 6, pp. 2558–2561, 2007.

[100] H. P. Boehm, A. Clauss, G. O. Fischer, and U. Hofmann, "Das adsorptionsverhalten sehr dnner kohlenstoff-folien," *Zeitschrift fr anorganische und allgemeine Chemie*, vol. 316, no. 34, pp. 119–127, 1962.

[101] W. Fu, M. E. Abbassi, T. Hasler, M. Jung, M. Steinacher, M. Calame, C. Schnenberger, G. Puebla-Hellmann, S. Hellmller, T. Ihn, and A. Wallraff, "Electrolyte gate dependent high-frequency measurement of graphene field-effect transistor for sensing applications," *Appl. Phys. Lett.*, vol. 104, no. 1, p. 013102, 2014.

[102] Y. Liang, X. Liang, Z. Zhang, W. Li, X. Huo, and L. Peng, "High mobility flexible graphene field-effect transistors and ambipolar radio-frequency circuits," *Nanoscale*, vol. 7, no. 25, pp. 10954–10962, 2015.

[103] Y. Xu and J. Liu, "Graphene as transparent electrodes: Fabrication and new emerging applications," *Small*, vol. 12, no. 11, pp. 1400–1419, 2016.

[104] F. Schedin, A. K. Geim, S. V. Morozov, E. W. Hill, P. Blake, M. I. Katsnelson, and K. S. Novoselov, "Detection of individual gas molecules adsorbed on graphene," *Nat. Mater.*, vol. 6, p. 652, 2007.

[105] Y. H. Kwak, D. S. Choi, Y. N. Kim, H. Kim, D. H. Yoon, S.-S. Ahn, J.-W. Yang, W. S. Yang, and S. Seo, "Flexible glucose sensor using cvd-grown graphene-based field effect transistor," *Biosens Bioelectron*, vol. 37, no. 1, pp. 82–87, 2012.

[106] J. H. An, S. J. Park, O. S. Kwon, J. Bae, and J. Jang, "High-performance flexible graphene aptasensor for mercury detection in mussels," *ACS Nano*, vol. 7, no. 12, pp. 10563–10571, 2013.

[107] Y. Ohno, K. Maehashi, Y. Yamashiro, and K. Matsumoto, "Electrolyte-gated graphene field-effect transistors for detecting ph and protein adsorption," *Nano Letters*, vol. 9, no. 9, pp. 3318–3322, 2009.

[108] A. A. Balandin, "Thermal properties of graphene and nanostructured carbon materials," *Nat. Mater.*, vol. 10, p. 569, 2011.

[109] A. K. Geim and K. S. Novoselov, "The rise of graphene," *Nat. Mater.*, vol. 6, p. 183, 2007.

[110] J.-C. Charlier, P. C. Eklund, J. Zhu, and A. C. Ferrari, *Electron and Phonon Properties of Graphene: Their Relationship with Carbon Nanotubes*, pp. 673–709. Berlin, Heidelberg: Springer Berlin Heidelberg, 2008.

[111] A. H. Castro Neto, F. Guinea, N. M. R. Peres, K. S. Novoselov, and A. K. Geim, "The electronic properties of graphene," *Rev. Mod. Phys.*, vol. 81, no. 1, pp. 109–162, 2009.

[112] J.-C. Charlier, X. Blase, and S. Roche, "Electronic and transport properties of nanotubes," *Rev. Mod. Phys.*, vol. 79, no. 2, pp. 677–732, 2007.

[113] K. S. Novoselov, S. V. Morozov, T. M. G. Mohinddin, L. A. Ponomarenko, D. C. Elias, R. Yang, I. I. Barbolina, P. Blake, T. J. Booth, D. Jiang, J. Giesbers, E. W. Hill, and A. K. Geim, "Electronic properties of graphene," *Phys. Stat. Sol. (b)*, vol. 244, no. 11, pp. 4106–4111, 2007.

[114] I. Meric, M. Y. Han, A. F. Young, B. Ozyilmaz, P. Kim, and K. L. Shepard, "Current saturation in zero-bandgap, top-gated graphene field-effect transistors," *Nat. Nanotechnol.*, vol. 3, p. 654, 2008.

[115] A. C. Ferrari, J. C. Meyer, V. Scardaci, C. Casiraghi, M. Lazzeri, F. Mauri, S. Piscanec, D. Jiang, K. S. Novoselov, S. Roth, and A. K. Geim, "Raman spectrum of graphene and graphene layers," *Phys. Rev. Lett.*, vol. 97, no. 18, p. 187401, 2006.

[116] K. F. Mak, J. Shan, and T. F. Heinz, "Electronic structure of few-layer graphene: Experimental demonstration of strong dependence on stacking sequence," *Phys. Rev. Lett.*, vol. 104, no. 17, p. 176404, 2010.

[117] F. Xia, D. B. Farmer, Y.-m. Lin, and P. Avouris, "Graphene field-effect transistors with high on/off current ratio and large transport band gap at room temperature," *Nano Lett.*, vol. 10, no. 2, pp. 715–718, 2010.

[118] E. V. Castro, K. S. Novoselov, S. V. Morozov, N. M. R. Peres, J. M. B. L. dos Santos, J. Nilsson, F. Guinea, A. K. Geim, and A. H. C. Neto, "Biased bilayer graphene: Semiconductor with a gap tunable by the electric field effect," *Phys. Rev. Lett.*, vol. 99, no. 21, p. 216802, 2007.

[119] Y. Zhang, T.-T. Tang, C. Girit, Z. Hao, M. C. Martin, A. Zettl, M. F. Crommie, Y. R. Shen, and F. Wang, "Direct observation of a widely tunable bandgap in bilayer graphene," *Nature*, vol. 459, p. 820, 2009.

[120] J.-H. Chen, C. Jang, S. Xiao, M. Ishigami, and M. S. Fuhrer, "Intrinsic and extrinsic performance limits of graphene devices on sio2," *Nat. Nanotechnol.*, vol. 3, p. 206, 2008.

[121] X. Du, I. Skachko, A. Barker, and E. Y. Andrei, "Approaching ballistic transport in suspended graphene," *Nat. Nanotechnol.*, vol. 3, p. 491, 2008.

[122] K. I. Bolotin, K. J. Sikes, J. Hone, H. L. Stormer, and P. Kim, "Temperature-dependent transport in suspended graphene," *Phys. Rev. Lett.*, vol. 101, no. 9, p. 096802, 2008.

[123] B. C. Brodie, "Xiii. on the atomic weight of graphite," *Philosophical Transactions of the Royal Society of London*, vol. 149, pp. 249–259, 1859.

[124] W. S. Hummers Jr and R. E. Offeman, "Preparation of graphitic oxide," *J. Am Chem. Soc.*, vol. 80, no. 6, pp. 1339–1339, 1958.

[125] L. Staudenmaier, "Verfahren zur darstellung der graphitsure," *Berichte der deutschen chemischen Gesellschaft*, vol. 31, no. 2, pp. 1481–1487, 1898.

[126] H. A. Becerril, J. Mao, Z. Liu, R. M. Stoltenberg, Z. Bao, and Y. Chen, "Evaluation of solution-processed reduced graphene oxide films as transparent conductors," *ACS Nano*, vol. 2, no. 3, pp. 463–470, 2008.

[127] S. Pei and H.-M. Cheng, "The reduction of graphene oxide," *Carbon*, vol. 50, no. 9, pp. 3210–3228, 2012.

[128] S. R. Kim, M. K. Parvez, and M. Chhowalla, "Uv-reduction of graphene oxide and its application as an interfacial layer to reduce the back-transport reactions in dye-sensitized solar cells," *Chem. Phys. Lett.*, vol. 483, no. 1, pp. 124–127, 2009.

[129] G. Williams, B. Seger, and P. V. Kamat, "Tio2-graphene nanocomposites. uv-assisted photocatalytic reduction of graphene oxide," *ACS Nano*, vol. 2, no. 7, pp. 1487–1491, 2008.

[130] S. Stankovich, D. A. Dikin, R. D. Piner, K. A. Kohlhaas, A. Kleinhammes, Y. Jia, Y. Wu, S. T. Nguyen, and R. S. Ruoff, "Synthesis of graphene-based nanosheets via chemical reduction of exfoliated graphite oxide," *Carbon*, vol. 45, no. 7, pp. 1558–1565, 2007.

[131] H.-J. Shin, K. K. Kim, A. Benayad, S.-M. Yoon, H. K. Park, I.-S. Jung, M. H. Jin, H.-K. Jeong, J. M. Kim, J.-Y. Choi, and Y. H. Lee, "Efficient reduction of graphite oxide by sodium borohydride and its effect on electrical conductance," *Adv. Funct. Mater.*, vol. 19, no. 12, pp. 1987–1992, 2009.

[132] P. Blake, P. D. Brimicombe, R. R. Nair, T. J. Booth, D. Jiang, F. Schedin, L. A. Ponomarenko, S. V. Morozov, H. F. Gleeson, E. W. Hill, A. K. Geim, and K. S. Novoselov, "Graphene-based liquid crystal device," *Nano Lett.*, vol. 8, no. 6, pp. 1704–1708, 2008.

[133] Y. Hernandez, M. Lotya, D. Rickard, S. D. Bergin, and J. N. Coleman, "Measurement of multicomponent solubility parameters for graphene facilitates solvent discovery," *Langmuir*, vol. 26, no. 5, pp. 3208–3213, 2010.

[134] U. Khan, A. O'Neill, M. Lotya, S. De, and J. N. Coleman, "High-concentration solvent exfoliation of graphene," *Small*, vol. 6, no. 7, pp. 864–871, 2010.

[135] U. Khan, H. Porwal, A. ONeill, K. Nawaz, P. May, and J. N. Coleman, "Solvent-exfoliated graphene at extremely high concentration," *Langmuir*, vol. 27, no. 15, pp. 9077–9082, 2011.

[136] C. Berger, Z. Song, T. Li, X. Li, A. Y. Ogbazghi, R. Feng, Z. Dai, A. N. Marchenkov, E. H. Conrad, P. N. First, and W. A. de Heer, "Ultrathin epitaxial graphite: 2d electron gas properties and a route toward graphene-based nanoelectronics," *J. Phys. Chem. B*, vol. 108, no. 52, pp. 19912–19916, 2004.

[137] J. Hass, W. A. d. Heer, and E. H. Conrad, "The growth and morphology of epitaxial multilayer graphene," *J. Phys. Condens. Matter*, vol. 20, no. 32, p. 323202, 2008.

[138] K. V. Emtsev, A. Bostwick, K. Horn, J. Jobst, G. L. Kellogg, L. Ley, J. L. McChesney, T. Ohta, S. A. Reshanov, J. Rhrl, E. Rotenberg, A. K. Schmid, D. Waldmann, H. B. Weber, and T. Seyller, "Towards wafer-size graphene layers by atmospheric pressure graphitization of silicon carbide," *Nat. Mater.*, vol. 8, p. 203, 2009.

[139] E. Rollings, G. H. Gweon, S. Y. Zhou, B. S. Mun, J. L. McChesney, B. S. Hussain, A. V. Fedorov, P. N. First, W. A. de Heer, and A. Lanzara, "Synthesis and characterization of atomically thin graphite films on a silicon carbide substrate," *J. Phys. and Chem. Solids*, vol. 67, no. 9, pp. 2172–2177, 2006.

[140] K. V. Emtsev, F. Speck, T. Seyller, L. Ley, and J. D. Riley, "Interaction, growth, and ordering of epitaxial graphene on sic0001 surfaces: A comparative photoelectron spectroscopy study," *Phys. Rev. B*, vol. 77, no. 15, p. 155303, 2008.

[141] C. Virojanadara, M. Syvjarvi, R. Yakimova, L. I. Johansson, A. A. Zakharov, and T. Balasubramanian, "Homogeneous large-area graphene layer growth on 6h-sic(0001)," *Phys. Rev. B*, vol. 78, no. 24, p. 245403, 2008.

[142] C. Berger, Z. Song, X. Li, X. Wu, N. Brown, C. Naud, D. Mayou, T. Li, J. Hass, A. N. Marchenkov, E. H. Conrad, P. N. First, and W. A. de Heer, "Electronic confinement and coherence in patterned epitaxial graphene," *Science*, vol. 312, no. 5777, pp. 1191–1196, 2006.

[143] J. Hass, F. Varchon, J. E. Milln-Otoya, M. Sprinkle, N. Sharma, W. A. de Heer, C. Berger, P. N. First, L. Magaud, and E. H. Conrad, "Why multilayer graphene on 4h-SiC(0001)behaves like a single sheet of graphene," *Phys. Rev. Lett.*, vol. 100, no. 12, p. 125504, 2008.

[144] P. N. First, W. A. de Heer, T. Seyller, C. Berger, J. A. Stroscio, and J.-S. Moon, "Epitaxial graphenes on silicon carbide," *MRS Bull.*, vol. 35, no. 4, pp. 296–305, 2011.

[145] F. Varchon, R. Feng, J. Hass, X. Li, B. N. Nguyen, C. Naud, P. Mallet, J. Y. Veuillen, C. Berger, E. H. Conrad, and L. Magaud, "Electronic structure of epitaxial graphene layers on sic: Effect of the substrate," *Phys. Rev. Lett.*, vol. 99, no. 12, p. 126805, 2007.

[146] Z.-Y. Juang, C.-Y. Wu, C.-W. Lo, W.-Y. Chen, C.-F. Huang, J.-C. Hwang, F.-R. Chen, K.-C. Leou, and C.-H. Tsai, "Synthesis of graphene on silicon carbide substrates at low temperature," *Carbon*, vol. 47, no. 8, pp. 2026–2031, 2009.

[147] X. Li, W. Cai, J. An, S. Kim, J. Nah, D. Yang, R. Piner, A. Velamakanni, I. Jung, E. Tutuc, S. K. Banerjee, L. Colombo, and R. S. Ruoff, "Large-area synthesis of high-quality and uniform graphene films on copper foils," *Science*, vol. 324, no. 5932, pp. 1312–1314, 2009.

[148] W. Liu, H. Li, C. Xu, Y. Khatami, and K. Banerjee, "Synthesis of high-quality monolayer and bilayer graphene on copper using chemical vapor deposition," *Carbon*, vol. 49, no. 13, pp. 4122–4130, 2011.

[149] A. Reina, X. Jia, J. Ho, D. Nezich, H. Son, V. Bulovic, M. S. Dresselhaus, and J. Kong, "Large area, few-layer graphene films on arbitrary substrates by chemical vapor deposition," *Nano Lett.*, vol. 9, no. 1, pp. 30–35, 2009.

[150] Z.-Y. Juang, C.-Y. Wu, A.-Y. Lu, C.-Y. Su, K.-C. Leou, F.-R. Chen, and C.-H. Tsai, "Graphene synthesis by chemical vapor deposition and transfer by a roll-to-roll process," *Carbon*, vol. 48, no. 11, pp. 3169–3174, 2010.

[151] K. Daiyu, S. Shintaro, Y. Katsunori, H. Naoki, S. Motonobu, N. Mizuhisa, and Y. Naoki, "Low-temperature synthesis of graphene and fabrication of top-gated field effect transistors without using transfer processes," *Appl. Phys. Express*, vol. 3, no. 2, p. 025102, 2010.

[152] C. M. Orofeo, H. Ago, B. Hu, and M. Tsuji, "Synthesis of large area, homogeneous, single layer graphene films by annealing amorphous carbon on co and ni," *Nano Res.*, vol. 4, no. 6, pp. 531–540, 2011.

[153] P. W. Sutter, J.-I. Flege, and E. A. Sutter, "Epitaxial graphene on ruthenium," *Nat. Mater.*, vol. 7, p. 406, 2008.

[154] J. Coraux, A. T. NDiaye, C. Busse, and T. Michely, "Structural coherency of graphene on ir(111)," *Nano Lett.*, vol. 8, no. 2, pp. 565–570, 2008.

[155] D. E. Starr, E. M. Pazhetnov, A. I. Stadnichenko, A. I. Boronin, and S. K. Shaikhutdinov, "Carbon films grown on pt(111) as supports for model gold catalysts," *Surf. Sci.*, vol. 600, no. 13, pp. 2688–2695, 2006.

[156] T. Oznuluer, E. Pince, E. O. Polat, O. Balci, O. Salihoglu, and C. Kocabas, "Synthesis of graphene on gold," *Appl. Phys. Lett.*, vol. 98, no. 18, p. 183101, 2011.

[157] Q. Yu, J. Lian, S. Siriponglert, H. Li, Y. P. Chen, and S.-S. Pei, "Graphene segregated on ni surfaces and transferred to insulators," *Appl. Phys. Lett.*, vol. 93, no. 11, p. 113103, 2008.

[158] C. Mattevi, H. Kim, and M. Chhowalla, "A review of chemical vapour deposition of graphene on copper," *J. Mater. Chem.*, vol. 21, no. 10, pp. 3324–3334, 2011.

[159] J. Kwak, J. H. Chu, J.-K. Choi, S.-D. Park, H. Go, S. Y. Kim, K. Park, S.-D. Kim, Y.-W. Kim, E. Yoon, S. Kodambaka, and S.-Y. Kwon, "Near room-temperature synthesis of transfer-free graphene films," *Nat. Commun.*, vol. 3, p. 645, 2012.

[160] K. S. Kim, Y. Zhao, H. Jang, S. Y. Lee, J. M. Kim, K. S. Kim, J.-H. Ahn, P. Kim, J.-Y. Choi, and B. H. Hong, "Large-scale pattern growth of graphene films for stretchable transparent electrodes," *Nature*, vol. 457, p. 706, 2009.

[161] X. Liang, B. A. Sperling, I. Calizo, G. Cheng, C. A. Hacker, Q. Zhang, Y. Obeng, K. Yan, H. Peng, Q. Li, X. Zhu, H. Yuan, A. R. Hight Walker, Z. Liu, L.-m. Peng, and C. A. Richter, "Toward clean and crackless transfer of graphene," *ACS Nano*, vol. 5, no. 11, pp. 9144–9153, 2011.

[162] M. C. Prado, D. Jariwala, T. J. Marks, and M. C. Hersam, "Optimization of graphene dry etching conditions via combined microscopic and spectroscopic analysis," *Appl. Phys. Lett.*, vol. 102, no. 19, p. 193111, 2013.

[163] S. Franssila, *Introduction to Microfabrication*. Chichester: John Wiley and Sons Ltd, 2004.

[164] R. W. Johnson, A. Hultqvist, and S. F. Bent, "A brief review of atomic layer deposition: from fundamentals to applications," *Mater. Today*, vol. 17, no. 5, pp. 236–246, 2014.

[165] A. Jorio, R. Saito, G. Dresselhaus, and M. S. Dresselhaus, *Raman Spectroscopy: From Graphite to sp2 Nanocarbons*.

[166] M. S. Dresselhaus, A. Jorio, M. Hofmann, G. Dresselhaus, and R. Saito, "Perspectives on carbon nanotubes and graphene raman spectroscopy," *Nano Lett.*, vol. 10, no. 3, pp. 751–758, 2010.

[167] L. M. Malard, M. A. Pimenta, G. Dresselhaus, and M. S. Dresselhaus, "Raman spectroscopy in graphene," *Phys. Rep.*, vol. 473, no. 5, pp. 51–87, 2009.

[168] A. C. Ferrari and D. M. Basko, "Raman spectroscopy as a versatile tool for studying the properties of graphene," *Nat. Nanotechnol.*, vol. 8, p. 235, 2013.

[169] A. Monshi, M. R. Foroughi, and M. R. Monshi, "Modified scherrer equation to estimate more accurately nano-crystallite size using xrd," *World Journal of Nano Science and Engineering*, vol. 2, pp. 154–160, 2012.

[170] S. Kim, J. Nah, I. Jo, D. Shahrjerdi, L. Colombo, Z. Yao, E. Tutuc, and S. K. Banerjee, "Realization of a high mobility dual-gated graphene field-effect transistor with al2o3 dielectric," *Appl. Phys. Lett.*, vol. 94, no. 6, p. 062107, 2009.

[171] A. Reina, X. Jia, J. Ho, D. Nezich, H. Son, V. Bulovic, M. S. Dresselhaus, and J. Kong, "Large area, few-layer graphene films on arbitrary substrates by chemical vapor deposition," *Nano Lett.*, vol. 9, no. 1, pp. 30–35, 2009.

[172] H. J. Park, J. Meyer, S. Roth, and V. Skkalov, "Growth and properties of few-layer graphene prepared by chemical vapor deposition," *Carbon*, vol. 48, no. 4, pp. 1088–1094, 2010.

[173] Y.-C. Lin, C. Jin, J.-C. Lee, S.-F. Jen, K. Suenaga, and P.-W. Chiu, "Clean transfer of graphene for isolation and suspension," *ACS Nano*, vol. 5, no. 3, pp. 2362–2368, 2011.

[174] D. W. Joshua, P. D. Gregory, A. C. Enrique, C. K. Justin, A. K. Joshua, D. Isha, B. Ashkan, H. Jayan, A. Basil, C. Yaofeng, D. Hefei, T. H. Richard, W. L. Joseph, and P. Eric, "Annealing free, clean graphene transfer using alternative polymer scaffolds," *Nanotechnology*, vol. 26, no. 5, p. 055302, 2015.

[175] Y. Lee, S. Bae, H. Jang, S. Jang, S.-E. Zhu, S. H. Sim, Y. I. Song, B. H. Hong, and J.-H. Ahn, "Wafer-scale synthesis and transfer of graphene films," *Nano Lett.*, vol. 10, no. 2, pp. 490–493, 2010.

[176] J. D. Caldwell, T. J. Anderson, J. C. Culbertson, G. G. Jernigan, K. D. Hobart, F. J. Kub, M. J. Tadjer, J. L. Tedesco, J. K. Hite, M. A. Mastro, R. L. Myers-Ward, C. R. Eddy, P. M. Campbell, and D. K. Gaskill, "Technique for the dry transfer of epitaxial graphene onto arbitrary substrates," *ACS Nano*, vol. 4, no. 2, pp. 1108–1114, 2010.

[177] C. T. Cherian, F. Giustiniano, I. Martin-Fernandez, H. Andersen, J. Balakrishnan, and B. zyilmaz, "bubble-free electrochemical delamination of cvd graphene films," *Small*, vol. 11, no. 2, pp. 189–194, 2015.

[178] A. Pirkle, J. Chan, A. Venugopal, D. Hinojos, C. W. Magnuson, S. McDonnell, L. Colombo, E. M. Vogel, R. S. Ruoff, and R. M. Wallace, "The effect of chemical residues on the physical and electrical properties of chemical vapor deposited graphene transferred to sio2," *Appl. Phys.Lett.*, vol. 99, no. 12, p. 122108, 2011.

[179] M. Ishigami, J. H. Chen, W. G. Cullen, M. S. Fuhrer, and E. D. Williams, "Atomic structure of graphene on sio2," *Nano Lett.*, vol. 7, no. 6, pp. 1643–1648, 2007.

[180] T. L. Chen, D. S. Ghosh, M. Marchena, J. Osmond, and V. Pruneri, "Nanopatterned graphene on a polymer substrate by a direct peel-off technique," *ACS Appl. Mater. Inter.*, vol. 7, no. 10, pp. 5938–5943, 2015.

[181] M. Miriam, W. Frederic, A. Therese, Z. Bin, J. Benedict, F. Manuel, C. Tong Lai, C. Theresa, L. Robert, P. Valerio, and M. Prantik, "Dry transfer of graphene to dielectrics and flexible substrates using polyimide as a transparent and stable intermediate layer," *2D Materials*, vol. 5, no. 3, p. 035022, 2018.

[182] L. G. P. Martins, Y. Song, T. Zeng, M. S. Dresselhaus, J. Kong, and P. T. Araujo, "Direct transfer of graphene onto flexible substrates," *P. Natl. Acad. Sci. USA*, vol. 110, no. 44, pp. 17762–17767, 2013.

[183] E. O. Polat, O. Balci, N. Kakenov, H. B. Uzlu, C. Kocabas, and R. Dahiya, "Synthesis of large area graphene for high performance in flexible optoelectronic devices," *Sci. Rep.*, vol. 5, p. 16744, 2015.

[184] M. A. Bissett, W. Izumida, R. Saito, and H. Ago, "Effect of domain boundaries on the raman spectra of mechanically strained graphene," *ACS Nano*, vol. 6, no. 11, pp. 10229–10238, 2012.

[185] J. E. Lee, G. Ahn, J. Shim, Y. S. Lee, and S. Ryu, "Optical separation of mechanical strain from charge doping in graphene," *Nat. Commun.*, vol. 3, p. 1024, 2012.

[186] A. Das, S. Pisana, B. Chakraborty, S. Piscanec, S. K. Saha, U. V. Waghmare, K. S. Novoselov, H. R. Krishnamurthy, A. K. Geim, A. C. Ferrari, and A. K. Sood, "Monitoring dopants by raman scattering in an electrochemically top-gated graphene transistor," *Nat Nanotechnol.*, vol. 3, p. 210, 2008.

[187] E. A. Carrion, J. D. Wood, A. Behman, M. Tung, J. W. Lyding, and E. Pop, "Variability of graphene mobility and contacts: Surface effects, doping and strain," in *72nd Device Research Conference*, pp. 199–200.

[188] R. H. J. Vervuurt, W. M. M. Kessels, and A. A. Bol, "Atomic layer deposition for graphene device integration," *Adv. Mater. Interfaces*, vol. 4, no. 18, p. 1700232, 2017.

[189] Z. Jin, Y. Su, J. Chen, X. Liu, and D. Wu, "Study of aln dielectric film on graphene by raman microscopy," *Appl. Phys. Lett.*, vol. 95, no. 23, p. 233110, 2009.

[190] Z. H. Ni, H. M. Wang, Y. Ma, J. Kasim, Y. H. Wu, and Z. X. Shen, "Tunable stress and controlled thickness modification in graphene by annealing," *ACS Nano*, vol. 2, no. 5, pp. 1033–1039, 2008.

[191] P. Zhou, S. Yang, Q. Sun, L. Chen, P. Wang, S. Ding, and D. W. Zhang, "Direct deposition of uniform high- dielectrics on graphene," *Sci. Rep-UK*, vol. 4, p. 6448, 2014.

[192] D. B. Farmer, H.-Y. Chiu, Y.-M. Lin, K. A. Jenkins, F. Xia, and P. Avouris, "Utilization of a buffered dielectric to achieve high field-effect carrier mobility in graphene transistors," *Nano Lett.*, vol. 9, no. 12, pp. 4474–4478, 2009.

[193] Y.-M. Lin, K. A. Jenkins, A. Valdes-Garcia, J. P. Small, D. B. Farmer, and P. Avouris, "Operation of graphene transistors at gigahertz frequencies," *Nano Lett.*, vol. 9, no. 1, pp. 422–426, 2009.

[194] H. Y. Liu, G. S. Tang, F. Zeng, and F. Pan, "Influence of sputtering parameters on structures and residual stress of aln films deposited by dc reactive magnetron sputtering at room temperature," *J. Cryst. Growth*, vol. 363, pp. 80–85, 2013.

[195] C. Mirpuri, S. Xu, J. D. Long, and K. Ostrikov, "Low-temperature plasma-assisted growth of optically transparent, highly oriented nanocrystalline aln," *J. Appl. Phys.*, vol. 101, no. 2, p. 024312, 2007.

[196] N. Sinha, G. E. Wabiszewski, R. Mahameed, V. V. Felmetsger, S. M. Tanner, R. W. Carpick, and G. Piazza, "Piezoelectric aluminum nitride nanoelectromechanical actuators," *Appl. Phys. Lett.*, vol. 95, no. 5, p. 053106, 2009.

[197] J. Nathan and M. Alan, "Enhancing the piezoelectric properties of flexible hybrid aln materials using semi-crystalline parylene," *Smart Mater. and Struct.*, vol. 26, no. 4, p. 045005, 2017.

[198] R. Dalmau, R. Schlesser, B. J. Rodriguez, R. J. Nemanich, and Z. Sitar, "Aln bulk crystals grown on sic seeds," *J. Cryst. Growth*, vol. 281, no. 1, pp. 68–74, 2005.

[199] H. Cheng, Y. Sun, J. X. Zhang, Y. B. Zhang, S. Yuan, and P. Hing, "Aln films deposited under various nitrogen concentrations by rf reactive sputtering," *J. Cryst. Growth*, vol. 254, no. 1, pp. 46–54, 2003.

[200] E. Smecca, F. Maita, G. Pellegrino, V. Vinciguerra, L. L. Magna, S. Mirabella, L. Maiolo, G. Fortunato, G. G. Condorelli, and A. Alberti, "Aln texturing and piezoelectricity on flexible substrates for sensor applications," *Appl. Phys. Lett.*, vol. 106, no. 23, p. 232903, 2015.

[201] L. Liao, Y.-C. Lin, M. Bao, R. Cheng, J. Bai, Y. Liu, Y. Qu, K. L. Wang, Y. Huang, and X. Duan, "High-speed graphene transistors with a self-aligned nanowire gate," *Nature*, vol. 467, p. 305, 2010.

[202] H. Wang, Y. Wu, C. Cong, J. Shang, and T. Yu, "Hysteresis of electronic transport in graphene transistors," *ACS Nano*, vol. 4, no. 12, pp. 7221–7228, 2010.

[203] A. Venugopal, L. Colombo, and E. M. Vogel, "Issues with characterizing transport properties of graphene field effect transistors," *Solid State Commun.*, vol. 152, no. 15, pp. 1311–1316, 2012.

[204] B.-C. Huang, M. Zhang, Y. Wang, and J. Woo, "Contact resistance in top-gated graphene field-effect transistors," *Appl. Phys. Lett.*, vol. 99, no. 3, p. 032107, 2011.

[205] F. Xia, V. Perebeinos, Y.-m. Lin, Y. Wu, and P. Avouris, "The origins and limits of metalgraphene junction resistance," *Nature Nanotechnol,*, vol. 6, p. 179, 2011.

[206] G. Giovannetti, P. A. Khomyakov, G. Brocks, V. M. Karpan, J. van den Brink, and P. J. Kelly, "Doping graphene with metal contacts," *Phys. Rev. Lett.*, vol. 101, no. 2, p. 026803, 2008.

[207] S. Russo, M. F. Craciun, M. Yamamoto, A. F. Morpurgo, and S. Tarucha, "Contact resistance in graphene-based devices," *Physica E: Low-dimensional Systems and Nanostructures*, vol. 42, no. 4, pp. 677–679, 2010.

[208] N. Kosuke and T. Akira, "Density-of-states limited contact resistance in graphene field-effect transistors," *Jpn. J. Appl. Phys.*, vol. 50, no. 7R, p. 070108, 2011.

[209] B. Huard, N. Stander, J. A. Sulpizio, and D. Goldhaber-Gordon, "Evidence of the role of contacts on the observed electron-hole asymmetry in graphene," *Phys. Rev. B*, vol. 78, no. 12, p. 121402, 2008.

[210] H. Zhong, Z. Zhang, H. Xu, C. Qiu, and L.-M. Peng, "Comparison of mobility extraction methods based on field-effect measurements for graphene," *AIP Adv.*, vol. 5, no. 5, p. 057136, 2015.

[211] J. A. Robinson, M. LaBella, K. A. Trumbull, X. Weng, R. Cavelero, T. Daniels, Z. Hughes, M. Hollander, M. Fanton, and D. Snyder, "Epitaxial graphene materials integration: Effects of dielectric overlayers on structural and electronic properties," *ACS Nano*, vol. 4, no. 5, pp. 2667–2672, 2010.

[212] L. Zheng, X. Cheng, D. Cao, G. Wang, Z. Wang, D. Xu, C. Xia, L. Shen, Y. Yu, and D. Shen, "Improvement of al2o3 films on graphene grown by atomic layer deposition with pre-h2o treatment," *ACS Appl. Mater. Interfaces*, vol. 6, no. 10, pp. 7014–7019, 2014.

[213] T. M. G. Mohiuddin, A. Lombardo, R. R. Nair, A. Bonetti, G. Savini, R. Jalil, N. Bonini, D. M. Basko, C. Galiotis, N. Marzari, K. S. Novoselov, A. K. Geim, and A. C. Ferrari, "Uniaxial strain in graphene by raman spectroscopy: G peak splitting, gruneisen parameters, and sample orientation," *Phys. Rev. B*, vol. 79, no. 20, p. 205433, 2009.

[214] S. Bochereau, S. Sinclair, and V. Hayward, "Perceptual constancy in the reproduction of virtual tactile textures with surface displays," *ACM Trans. Appl. Percept.*, vol. 15, no. 2, pp. 1–12, 2018.

[215] N. Yogeswaran, S. Gupta, and R. Dahiya, "Low voltage graphene fet based pressure sensor," in *2018 IEEE SENSORS*, pp. 1–4.

[216] P. K. Panda and B. Sahoo, "Pzt to lead free piezo ceramics: A review," *Ferroelectrics*, vol. 474, no. 1, pp. 128–143, 2015.

[217] N. Izyumskaya, Y. I. Alivov, S. J. Cho, H. Morko, H. Lee, and Y. S. Kang, "Processing, structure, properties, and applications of pzt thin films," *Crit. Rev. Solid State*, vol. 32, no. 3-4, pp. 111–202, 2007.